Phased array antenna with significant reduction of active controls

Francesco Scattone

To cite this version:

Francesco Scattone. Phased array antenna with significant reduction of active controls. Electronics. Université de Rennes, 2015. English. NNT : 2015REN1S168 . tel-01417803

ANNÉE 2015

THÈSE / UNIVERSITÉ DE RENNES 1
sous le sceau de l'Université Européenne de Bretagne

pour le grade de

DOCTEUR DE L'UNIVERSITÉ DE RENNES 1

Mention : Traitement du Signal et Télécommunications
Ecole doctorale MATISSE
présentée par

Francesco SCATTONE

préparée à l'unité de recherche UMR 6164 - I.E.T.R
Institut d'Électronique et de Télécommunications de Rennes
UFR Informatique - Électronique

Phased array antenna with significant reduction of active controls

Thèse soutenue à Rennes
le 15 décembre 2015
devant le jury composé de :

Thierry MONEDIERE
Professeur, XLIM, Limoges / rapporteur
Xavier BEGAUD
Professeur, LTCI, Paris / rapporteur
Hélène ROUSSEL
Professeur, LE2, Paris / examinateur
Shah Nawaz BUROKUR
Maître de conférences, IEF, Paris / examinateur
Giovanni TOSO
Docteur, ESA, Noordwijk, Pays-Bas / membre invité
Benjamin FUCHS
Chercheur CNRS, IETR, Rennes / membre invité
Mauro ETTORRE
Chercheur CNRS, IETR, Rennes / directeur de thèse
Ronan SAULEAU
Professeur, IETR, Rennes / co-directeur de thèse
Nelson FONSECA
Docteur, ESA, Noordwijk, Pays-Bas / co-directeur de thèse

L'auteur, les encadrants, le laboratoire et ses tutelles tiennent à remercier le Conseil Régional de Bretagne pour l'attribution d'une allocation de recherche doctorale (ARED, campagne 2012) ainsi que l'Agence Spatiale Européenne pour son soutien scientifique, technique et financier.

A mio nonno

Acknowledgments

My Ph.D. work would have never been possible without the contribution and the support of the people I met in IETR and ESA-ESTEC and I would like to express my gratitude to them.

First of all, I would like to thank my supervisor Mauro Ettorre for the time he spent teaching me most of the thing I needed and I will need during my future career. Grazie Mauro.

I would like to thank Prof. Ronan Sauleau, my co-supervisor in IETR, for his precious support during the years I spent in IETR.

I would express my gratitude to Nelson Fonseca, my co-supervisor in ESA-ESTEC, for working close with me during the three years of Ph.D. and for letting me enjoy my stay in The Netherlands.

I wish to acknoledge Prof. Thierry Monediere and Xavier Begaud for carefully reviewing this manuscript and Prof. Hélène Roussel, Prof. Shah Nawaz Burokur, Giovanni Toso and Benjamin Fuchs, for being members of the jury.

I would also thank my colleagues in IETR for the time we spent togheter, in particular Franck, Carole, Narcisse, François, Laurent.

I ricordi più belli di questi tre anni vengono dagli amici che ho incontrato e che sono diventati la mia famiglia durante questo periodo. In particolare vorrei ringraziare (nell'ordine in cui li ho conosciuti) Giovanni, Ana, Francesco (FFM), Giovannis, Fabrizio 'o sarracino e Ida. Tra questi non ho inserito Riccardo, poiché in lui non ho trovato un amico, ma un fratello.

Il mio pensiero va anche ai miei amici storici che mi hanno supportato da lontano: Federico, Claudio, Eleonora (che mi ha supportato e sopportato), Michelle, Piero, Luca e Andrea. Un grazie va alla mia famiglia e in particolare ai miei nonni che hanno vissuto questa mia esperienza con un'enfasi speciale. Infine un ringraziamento va a Rosa, entrata nella mia vita nella parte finale di questo percorso lasciando un segno indelebile.

Abstract

The objective of this thesis is to exploit the leaky-wave phenomena to enhance the performance of classical aperture antennas for space applications. Here, we consider planar configurations where the leaky modes are excited between a ground plane and a partially reflective superstrate, made of impedance sheets or dielectric slabs. Arrangements of small apertures opening on the ground plane are used to feed the antennas under study. The superstrate-like leaky-wave structures are developed in array or phased array configurations. These solutions are considered of interest in terms of flexibility of the system for next generation satellite links.

In order to efficiently study planar leaky-wave arrays, we have developed an analysis tool based on a Green's function spectral approach. The developed tool allows to precisely analyze the proposed structure by taking into account the impact of the mutual coupling among the elements on the radiation performance of the whole antenna. In addition, it can handle extremely large structures in terms of wavelengths with a small computational effort with respect to commercial tools. This tool has been used during the thesis to efficiently analyze the main features associated to the leaky-wave phenomenon, such as the gain enhancement and pattern shaping, for the improvement of the performance of the classical array solutions.

In particular, the gain enhancement of leaky-based structures can be an effective way to reduce the number of elements of the associated phased arrays. In a leaky-wave configuration each element of the array will radiate with a larger equivalent aperture allowing a larger spacing among elements without affecting the final gain of the whole structure. This aspect is particularly important in the case of phased arrays, where phase shifters and control cells are, typically, the most expensive components of the system. As extensively explained in the manuscript, antennas for user segment might find the highest benefit by using leaky-wave solutions. In fact, the constraints on bandwidth ($1 \sim 3\,\%$) and periodicity ($1 \sim 2$ wavelengths) make the leaky-wave technology suitable to reach the high aperture efficiencies required for such applications.

Besides the gain enhancement, the leaky-wave technology can be effectively exploited to conveniently shape the radiation pattern by properly engineering the design parameters of the antenna. For superstrate-like structures, as those considered in this work, such parameters are the reflectivity of the partial reflecting screens and their spacing. This capability can be used in phased arrays to generate a convenient element pattern to minimize the scan losses and filter the grating lobes appearing in the visible space when dealing with periodicities larger than a wavelength. Therefore, a synthesis procedure for thinned leaky-wave arrays is presented in the manuscript, showing the benefits of the superstrate configuration. In particular, it is shown that it is possible to design

thinned arrays with a number of elements reduced by a factor 4, if compared with bare configurations, working in a band of 7 %. Also, a novel array configuration, the irregular superstrate array, is presented. The irregular superstrate allows the reduction of the side lobes of the antenna below -20 dB in the considered 2.5 % band, using a uniform excitation. Such solution avoids the use of complicate feeding networks of classical solution. This last configuration clearly shows that the shaping capability of leaky-wave antennas is the most appealing feature to be used in phased array solutions.

Résumé

Les systèmes satellitaires multimédias actuels et de prochaine génération en bandes Ku et Ka peuvent bénéficier des caractéristiques flexibles des antennes multifaisceaux. Les spécifications typiques peuvent être 20 $\sim$ 100 faisceaux simultanés ou multiplexés avec une largeur de $0.5^\circ \sim 1^\circ$ et un gain dessus 40 dB, couvrant une zone angulaire régionale ou continentale de $3^\circ \sim 10^\circ$ depuis l'orbite terrestre géostationnaire. Compte tenu de l'évolution rapide des marchés des médias par rapport à une durée de vie typique des satellites de télécommunication, l'un des aspects les plus importants est la flexibilité du système, i.e. la possibilité de reconfigurer les faisceaux électroniquement pour pointer vers des zones géographiques présentant la plus forte demande. Les antennes réseau à commande de phase sont la technique la plus prometteuse pour satisfaire ces besoins de la mission. Ils permettent de changer la répartition de la puissance aux faisceaux, la taille du faisceau et la forme du faisceau alors que l'antenne est en orbite, ce qui représente une excellente solution en termes de flexibilité du système. Cependant, l'un des paramètres les plus critiques dans la conception de réseau à commande de phase est le nombre d'éléments car cela détermine le nombre de déphaseurs et des unités de commande qui sont souvent les composants les plus chers de l'ensemble.

Ces travaux de thèse sont centrés sur l'étude de nouveau réseaux à commande de phase. En particulier, les réseaux d'antennes planaires à ondes de fuite sont exploités pour améliorer les performances des réseaux d'antennes classiques. Il s'agit d'une solution

extrêmement intéressante pour augmenter le gain, diminuer le niveau des lobes secondaires et, plus généralement, modeler le diagramme de rayonnement des sources simples. Les antennes étudiées ici sont des structures à ondes de fuite planaires avec superstrat. Les modes à ondes de fuite sont excités par source située à l'intérieur d'une cavité résonante, aussi appelé cavité Fabry-Pérot, formée par un plan de masse métallique et une surface partiellement réfléchissante. Cette dernière est un superstrat placé au-dessus d'un plan de masse et peut être réalisé à l'aide de couches diélectriques ou de surfaces d'impédance. Nous présentons ci-dessous les principales parties de ce travail de thèse.

Outil d'Analyse

L'étude approfondie des structures réseaux avec superstrat et leurs possibles configurations innovantes nécessitent un outil d'analyse rapide. Ce dernier doit permettre d'évaluer efficacement les propriétés de rayonnement de ces structures de manière fiable et rapide. Les simulateurs commerciaux à usage général ne sont pas adaptés à ce besoin car ils nécessitent des ressources informatiques importantes, même pour la résolution des problèmes simples. Pour cette raison nous avons développé un outil d'analyse. Cet outil est basé sur une approche spectrale avec fonction de Green. Il permet d'évaluer les caractéristiques de rayonnement (diagramme de rayonnement, paramètres S, gain, niveau des lobes secondaires, largeur de faisceau) pour des réseaux génériques présentant un arrangement régulier ou irrégulier de sources génériques (ouvertures uniformes, guides d'ondes, antennes cornets, antennes cornet ondulé) sur un plan de masse, avec ou sans superstrat. L'algorithme développé a été validé avec les logiciels commerciaux (CST MWS, HFSS). Un excellent accord a été obtenu avec une réduction considérable du temps de calcul et d'utilisation de mémoire.

Outil de Synthèse pour le Diagramme de Rayonnement d'Antennes à Ondes de Fuite

Nous avons également développé un outil de synthèse conçu pour générer une structure à ondes de fuite apte à produire un diagramme de rayonnement demandé décrit analytiquement. La synthèse est réalisée en optimisant opportunément les paramètres de conception de l'antenne. Un prototype, produisant un diagramme de rayonnement sectoriel a été fabriqué et testé. Un bon accord est obtenu entre les résultats de simulation et les mesures.

Diagrammes de Rayonnement Cosécante-Carré

Cette partie concerne la génération d'un diagramme de rayonnement cosécante-carré, utile dans les applications où une illumination de puissance uniforme est nécessaire dans une certaine région angulaire. Dans la littérature, de tels diagrammes sont généralement obtenus en utilisant des réflecteurs courbes, des antennes réseau, des réseaux réflecteurs, des antennes lentilles. Ici, un diagramme en cosécante-carré est obtenu en tronquant opportunément le superstrat. La troncature supprime le mode à ondes de fuite magnétique transversal se propageant le long de la direction y positif sans affecter celui se propageantsur le côté opposé.

Performance des Réseaux d'Antennes Planaires à Ondes de Fuite

Ici, nous étudions la possibilité d'améliorer le gain de réseaux d'antennes utilisant des structures à ondes de fuite. L'objectif final est la réduction du nombre d'éléments du réseau. Cette opération peut être effectuée en utilisant la procédure de synthèse présentée ci-après. Une étude paramétrique a été effectué sur les réseaux d'antennes à ondes de fuite, en faisant varier les characteristiques du superstrat et les grillages du réseau. Ces résultats ont été utilisés pour concevoir des réseaux d'antennes planaires à ondes de fuite pour les segments bord et utilisateur, dont les specifications sont très différentes (maille de réseau, directivité d'élément et bande passante). Nos travaux ont montré que les configurations à superstrat sont particulièrement avantageuses pour le segment utilisateur.

Réseaux d'Antennes Bi-Bande avec Superstrat Échiquier

La nécessité d'élargir la bande passante des antennes à ondes de fuite nous a conduit à proposer une nouvelle antenne, appelée antenne superstrat-patch. Cette configuration permet d'améliorer le gain avec des antennes de Fabry-Pérot classiques, mais sur une bande plus large. Étant donné que chaque élément a son propre superstrat, nous avons décidé de mettre en œuvre l'antenne superstrat-patch dans un réseau bi-bande en Ku et Ka. Le réseau d'antenne proposé présente des propriétés très intéressantes en comparaison avec les solutions classiques.

Synthèse d'Antennes Réseaux Raréfiés à Ondes de Fuite

Ici, nous proposons une méthode de synthèse pour concevoir des antennes réseaux raréfiés à ondes de fuite. Une procédure d'optimisation convexe a été développée pour réduire le nombre d'éléments du réseau, tout en maintenant le diagramme de rayonnement à l'intérieur d'un gabarit prédéterminé. Le couplage mutuel entre les éléments est pris en compte lors de la procédure d'optimisation. Les résultats finaux conduisent à la synthèse de réseaux comportant un nombre réduit d'éléments et possédant une efficacité d'ouverture accrue par rapport à la configuration sans superstrat.

Réseau avec Superstrat Irrégulier

Le réseau avec superstrat irrégulier permet de contrôler le niveau des lobes secondaires du réseau en utilisant une excitation uniforme, ce qui simplifie la conception du formateur de faisceau. Un tel superstrat présente un gain différent pour chaque élément du réseau. Un réseau linéaire avec des lobe secondaires et des lobe de réseau réduits a ainsi été conçu en bande Ku, présentant d'excellentes performances.

Contents

List of Figures

List of Tables

Abbreviations

BFN	**B**eam-**F**orming **N**etwork
C/I	**C**arrier to **I**nterference ratio
DSA	**D**eep **S**pace **A**ntenna
EBG	**E**lectromagnetic **B**and-**G**ap
EoC	**E**dge **o**f **C**overage
EIRP	**E**ffective **I**sotropic **R**adiated **P**ower
FPC	**F**abry-**P**erot **C**avity
FSS	**F**requency **S**elective **S**urface
GEO	**G**eostationary **E**arth **O**rbit
HPBW	**H**alf-**P**ower **B**eam**W**idth
LRR	**L**aser **R**etro-**R**eflector
LWA	**L**eaky-**W**ave **A**ntenna
MEO	**M**edium **E**arth **O**rbit
MN	**M**atching **N**etwork
PCB	**P**rinted **C**ircuit **B**oard
Rx	**R**eceive
SLL	**S**ide **L**obe **L**evel
TE	**T**ransverse **E**lectric
TL	**T**ransmission **L**ine
TM	**T**ransverse **M**agnetic
Tx	**T**ransmit

Chapter 1

Introduction

Present and next-generation multimedia satellite systems in Ku- and Ka-bands can benefit from flexible multiple beam capabilities. Typical requirements can be $20 \sim 100$ simultaneous or multiplexed beams with a size of $0.5^\circ \sim 1^\circ$ and a gain over 40 dB, covering a continental or sub-continental angular region of $3^\circ \sim 10^\circ$ from geostationary Earth orbit (GEO). An example of a multiple beam coverage of the European continent and the Mediterranean basin is shown in Fig. 1.1.

Considering the fast evolution of multimedia market with respect to a typical telecommunication satellite life time, one of the most important aspects is the flexibility of the system, i.e. the possibility to reconfigure the beams electronically to address geographical areas with the highest demand.

Active phased arrays are the most promising technique to satisfy such mission needs. They enable changing the allocation of power to the beams, the beam size and the beam shape while the antenna is in orbit, representing the best antenna solution in terms of flexibility of the system. However, the most critical parameter of a phased array design is the number of elements as it determines the number of phase shifters and control units that are often the most expensive components of the array.

1.1 Antennas for Satellite Communications

The design of antennas for satellites communication systems is a challenging task. It involves several considerations that must be handled at different levels. From a system

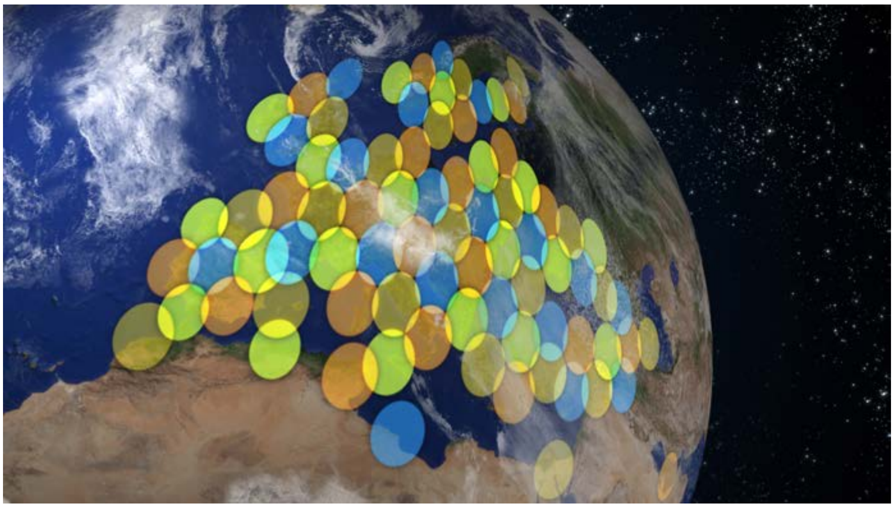

Figure 1.1: Coverage of Europe and the Mediterranean basin by Eutelsat KA-SAT 9A.

point of view, the most important parameters are the Effective Isotropic Radiated Power (EIRP) for transmitting antennas and the antenna gain to noise temperature G/T for receiving antennas [1].

Different specifications are needed for the space segment (on-board satellite antennas) and user segment (terminal antennas). During the last years, the technology dramatically changed the specifications for both parts. The main improvement is related to the frequency bands shifting upward, with broad bandwidth frequency allocations and more compact antennas. Frequency and polarization reuse schemes made possible a great increase in the communication capacity [2].

In the past, satellite antennas were covering the whole Earth visible disk. Nowadays, the area to be covered is divided in sub-regions (Fig. 1.1), using spot beam and multiple beam architectures [3]. The directivities that can be reached with these technologies are very high compared with the older satellite links, as they service smaller areas.

However, the electromagnetic performance is not the only parameter to be considered in a space link design. In fact, the designer typically faces other unconventional constraints, related to the size, the weigth, the power and, eventually, the costs.

The user segment takes advantage from the high performing on-board satellite antennas. Initially, the user segment needed huge dedicated ground terminals, serving as hubs and communicating with the user through side connections. Today, the general performance

FIGURE 1.2: Geostationary Earth orbit satellite phone Immarsat IsatPhone 2.

FIGURE 1.3: Estrack DSA in Cebreros, Spain.

enhancement on the space segment allows a reduction of the size of the antenna and/or a greater data rate. A user segment antenna, in general, has to be small, inexpensive and reliable to pointing errors from the user. A good example of compact satellite communication unit is the GEO satellite phone in Fig. 1.2. Huge reflector antennas, instead, are used just for particular applications, as high data rate links and Deep Space Antennas (DSA). Fig. 1.3 shows the 35 m-diameter DSA in Cebreros, Spain, part of the Estrack tracking station. A main design issue in the user segment is the reduction of the interference with other sources. In particular, a strong regulation in terms of side lobe envelope has to be respected for the congested C- and Ku-bands [4].

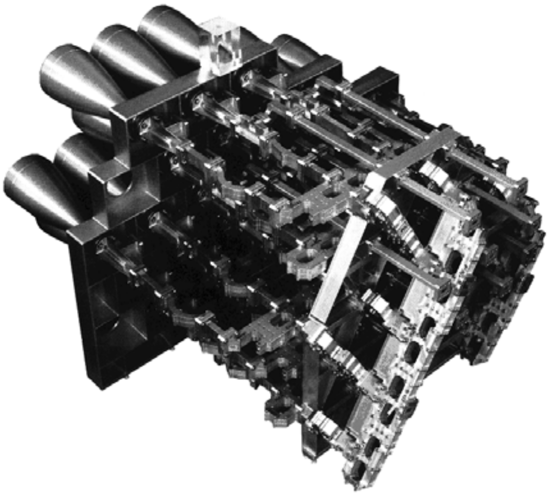

Figure 1.4: Feed system for a Ka-band multibeam antenna (Alenia Spazio).

The antenna types mainly employed for space applications are horn antennas, reflector antennas and direct radiating array antennas.

1.1.1 Horn Antennas

Horn antennas are the basic antenna solution and they managed to preserve their space in the modern satellite communication [5]. The reason why horn antennas are so popular is their simplicity along with the high performance in terms of gain and matching.

In early satellites, horn antennas were used for the global coverage of the Earth from geostationary satellites [6]. The beamwidth required for this application is about 17 degrees and the horn could easily fit due to its simplicity and electromagnetic characteristics.

Nowadays, Earth coverage applications are not widely used, leaving the scene to highly directive solutions for spot coverage and multiple beam applications. In these scenarios horn antennas are still employed as phased array elements or feed for reflector antennas [7]. A cluster of horn feed is shown in Fig. 1.4 as example.

Dual-Mode Conical Horns

The dual-mode conical horn has been proposed by Potter in 1963 [8]. A TM_{11} higher-order mode is excited to symmetrise the aperture distribution given by the fundamental TE_{11}. The radiation pattern is nearly symmetric and it presents low side lobe level

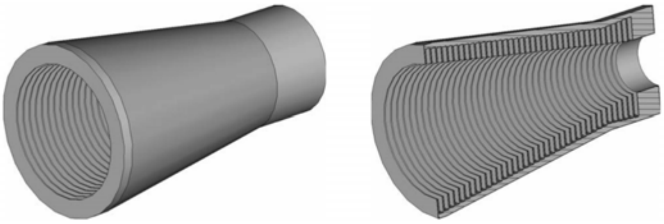

Figure 1.5: Corrugated conical horn [5].

(SLL). However, this solution reduces the operational bandwidth of the horn, because the two modes have to be excited with a precise phase difference.

Hybrid-Mode Corrugated Conical Horns

Corrugated conical horns (Fig. 1.5) provide circularly symmetric radiation pattern, low SLL and low levels cross-polarization. An HE_{11} mode is excited in the horn, that is an hybrid of the TE_{11} and TM_{11} modes that would be excited in a smooth waveguide. The corrugated horn has a larger bandwidth if compared to the dual-mode horn. Contrary to the latter, the two components of the HE_{11} have the same cut-off frequency and phase velocity, allowing the phase relation to remain the same along the frequency. However, the crosspolar bandwidth is still limited. The main reasons are the loss of the purely balanced hybrid condition and the excitation of high order modes inside the horn [7].

1.1.2 Reflector Antennas

Reflector antennas are the most common and cost effective high-gain antenna system for satellite applications. While the equipment for user segment reached extremely low prices with simple configurations (as for the case of direct-to-home television DTHTV), the space segment remains a challenging task. The constraints for the launch of the satellite impose the reflector system to be light and foldable, but once deployed it must be rigid and reliable despite the demanding in-orbit environment.

Different feed and reflector technologies are used for different scenarios. In the following we will focus our attention on the space segment, analyzing the spot coverage and multiple beam designs.

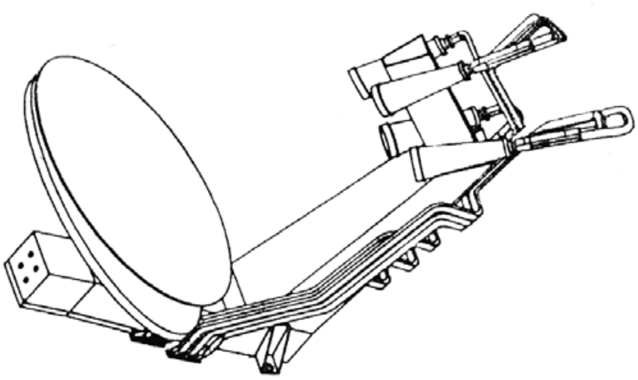

Figure 1.6: A Front-Fed Offset Reflector Antenna with Multiple-Feed Horns (Alenia Spazio).

1.1.2.1 Spot Coverage Design

Reflector antennas are the main choice for the spot coverage of the Earth, where the antenna must cover a limited field of view [3].

In a simple scenario, the reflector antenna can be used to illuminate a geographical region, mechanically tilting the beam to point at the centroid of the coverage area. This technique also allows the repositioning of the beam during the satellite lifetime.

The designers often face more complex situations. Electromagnetic requirements have to be respected at the geopolitical boundaries, leading to an irregular coverage regions. The single spot beam configuration might not be sufficient to satisfy the power density constraints. In this case, a cluster of feed can be exploited to illuminate a larger reflector (Fig. 1.6), increasing the flexibility of the system. The independent beams are used to produce the contours of the radiation pattern necessary to cover the region. The larger aperture produces narrower beams, allowing the fine shaping of the pattern. Furthermore, this approach reduces the SLL and the interference with the sources located outside the covering zone and enhances the overall gain of the antenna.

An efficient but not flexible alternative to the antenna solution described above consists in the use of shaped reflectors, designed to cover a predefined region [9].

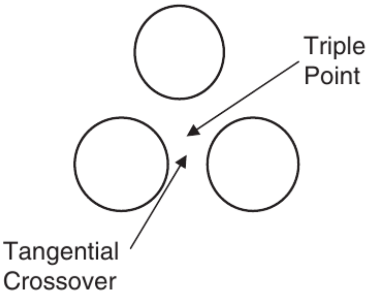

FIGURE 1.7: Tangential crossover and triple point location [3].

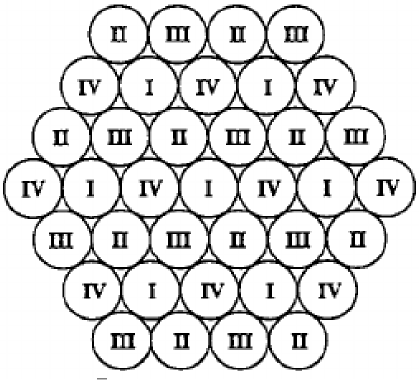

FIGURE 1.8: The hexagonal-grid layout of a four-color reuse scheme [10].

1.1.2.2 Multiple Beam Design

A multiple beam antenna covers the desired region using multiple beams with independent data streams. The gain of the antenna is higher, since it has to service a smaller area, resulting in a higher data rate and reduced user performance requirements [3].

In a multiple beam design, the beams are usually arranged on an equilateral triangular pattern, as shown in Fig. 1.7. The minimum gain occurs at the center of the triangle, called triple point. The tangential crossover is, instead, the point corresponding to the halfway between the centers of two adjacent beams.

A main design challenge in multiple beam designs is to obtain high gain at the crossover points, illuminating completely the region and, at the same time, minimizing the interference with the adjacent cells. For this scope, the two main design parameters for multiple beam coverage are the edge of coverage (EoC) directivity and the carrier to interference ratio (C/I) [10]. The EoC directivity is the directivity of the beam at the crossover between two cells. At the same time, co-polar component of the adjacent

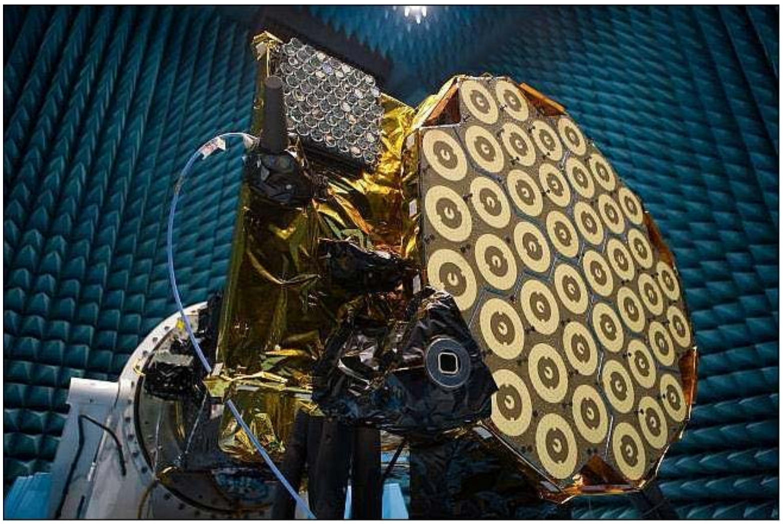

Figure 1.9: Earth-Facing Panel of GIOVE-B showing the navigation antenna and the LRR panel.

beams, or C/I, must be minimized. To have low interference, each beam needs low side lobes. The SLL is reduced using a tapered amplitude distribution on the aperture of the reflector which can be obtained through a more directive feed. This characteristic is obtained enlarging the feed aperture. However this implies a larger spacing between each feed and a larger angular separation between adjacent feeds, resulting in a gain loss at the crossover. Several ways have been studied to solve the issue, as a partial overlap of neighbor feeds or the generation of an additional beam by combining the beams around the triple point, but the most efficient solution still remains to use multiple reflector antennas to produce a given multiple beam coverage, typical 3 or 4.

The spatial discretization is not the only way exploited to isolate adjacent beams. In the multiple beam scenario, adjacent beams typically use different polarization and frequency sub-bands [2]. Frequency/polarization reuse schemes are employed to reduce the interference. The four-cell reuse scheme, or four-color topology, is the most exploited for GEO satellites (Fig. 1.8), dividing the available frequency band in two sub-portions and alternating left and right circular polarizations.

1.1.3 Phased Array Antennas

Phased array antennas are the most promising technique to satisfy the requirements of modern antenna systems in space environment. They are the best solution in terms of flexibility, allocation of power to the beams, beam size and beam shape [11, 12]. Several solutions have been studied in the past to make this promising technology suitable for both space and user segments. As an example, Fig. 1.9 shows the navigation phased array antenna and the LRR (laser retro-reflector) panel installed on the GIOVE-B satellite.

The main drawback of phased arrays is the complexity of their architecture and the consequent high costs. Indeed, the most critical parameter of a phased array design is the number of elements because it determines the number of phase shifters and control cells, that are the most expensive component of the array [13]. On the other hand, the number of elements is related to the gain, the side lobe level and the scan capabilities of the array. The general procedure to design a phased array consist in choosing an inter-element distance to avoid the appearance of the grating lobes in the real space while scanning the main beam. However, if the scanning sector is small ($5° \sim 25°$) it might be possible to increase the inter-element distance and, consequently, decrease the number of elements.

Several solutions have been provided in literature to efficiently increase the distance between elements and/or reduce the number of amplitude/phase controls. In the following we analyze the phased arrays with irregular lattices and the sub-array technique.

1.1.3.1 Irregular Arrays

The use of half-wavelength spaced fully-populated array might be unacceptable for large structures with a huge number of elements. The reasons are linked to the complexity of the resulting array antenna, not just involving the costs, but also electromagnetic parameters such as the mutual coupling that might degrade the scanning performances [12]. Furthermore, several applications require a narrow beamwidth and low side lobes, but not necessarily a high gain. This is the case for satellite receiving antennas operating against jamming, ground-based high-frequency radars and interferometers for radio astronomy [11].

For these and other applications it is possible to remove and/or displace some of the array elements ending up with an irregular array configuration. The beamwidth of the main lobe is not dramatically perturbed, as the size of the array remains the same. The antenna gain reduces proportionally to the elements reduction (neglecting the mutual

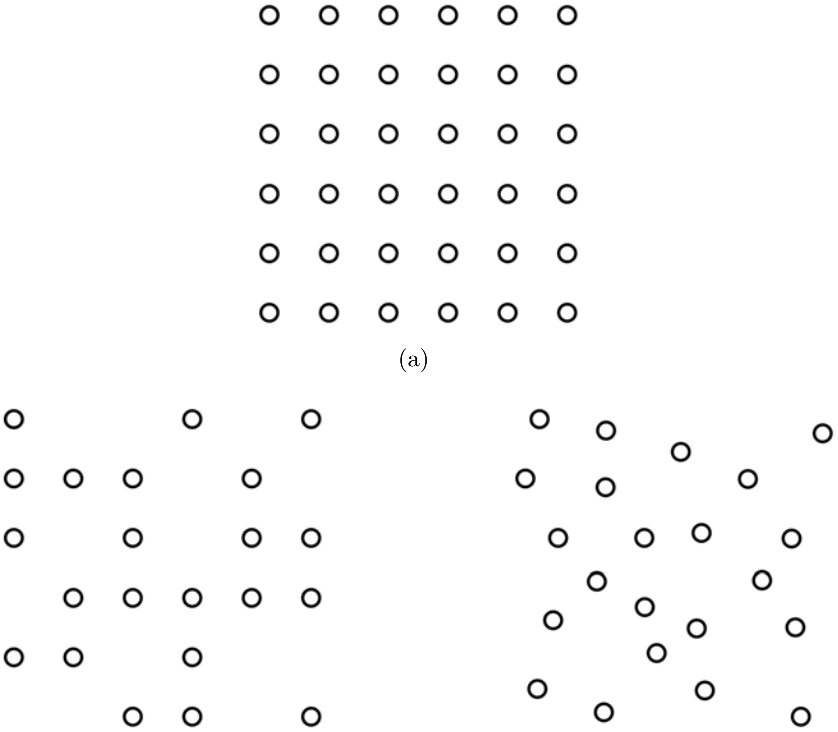

(a)

(b)

(c)

FIGURE 1.10: (a) Fully-populated array. (b) Thinned array. (c) Sparse array.

coupling in a first approximation), but a high directive array can be obtained with important advantages in terms of complexity and costs.

Phased array antennas with irregular element spacings are extensively studied in literature. In particular, we talk about thinned arrays when removing elements starting from a regular lattice. We refer to sparse array, instead, when the array elements are displaced and the optimization is performed on their positions. Fig. 1.10 shows a representation of the irregular array types starting from a 6×6 fully-populated array.

The synthesis of the array is performed to have the radiation pattern fitting a desired radiation mask. Depending on the specifications, different approaches can be used for the array synthesis [14–19]. The description of these methods is beyond the scope of this manuscript.

1.1.3.2 Overlapped Sub-Arrays

Another way to reduce the number of controls of a phased array is dividing it in sub-arrays. However, the criterion to group the elements must be carefully studied. The

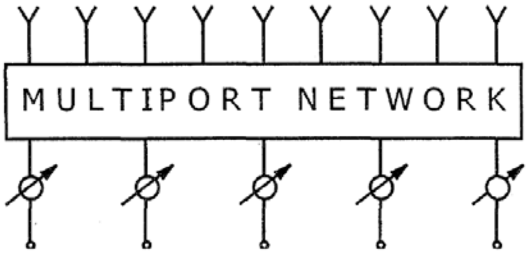

FIGURE 1.11: General case of multi-port network [13].

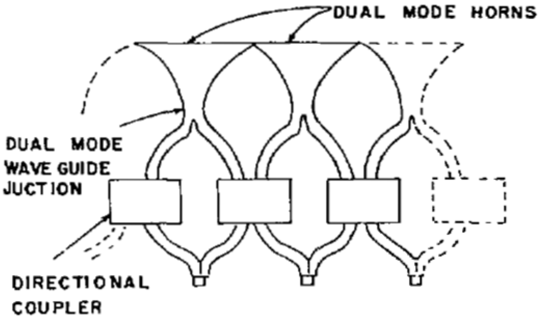

FIGURE 1.12: Multi-port network proposed in [21].

authors of [20] show the drawbacks of a simple sub-array. They divide a regular array of 592 elements in "tiles" of 4×4 elements, in order to simplify the beam forming network by a factor 16. This simplification leads to $\sim$ 3 dB scan losses at the edge of coverage and grating lobes pointing toward the Earth.

Several techniques have been addressed to design an effective sub-array-based system. Typically, a flat-topped radiation pattern is desired at sector level, filtering the grating lobes outside the field of view and minimizing the scan losses [21]. The goal is to produce a $\sin x/x$ aperture distribution using the sub-array. The overalapped sub-array is the most effective way to produce this distribution. A sub-array is called overlapped when its physical size exceed the distance between sub-arrays.

The price to pay for the enhanced performance of overlapped sub-arrays is a more complex beam forming network, with respect to the standard sub-arrays.

Multi-Port Networks

The most common method to produce the desired sector aperture field is to use a passive multi-port network to be inserted between the phase shifters and the radiated elements,

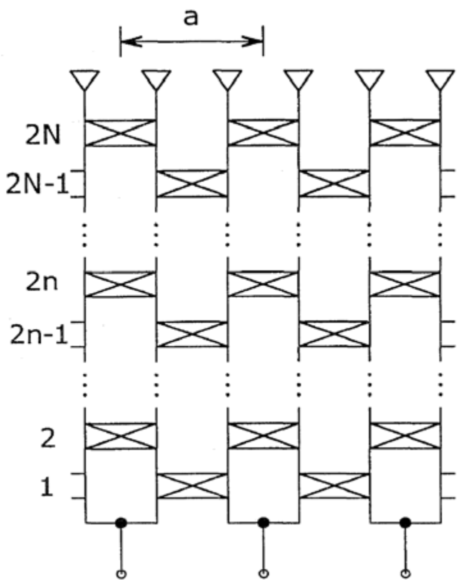

FIGURE 1.13: N-layers chess network [13].

as shown in Fig. 1.11. The spacing between control cells determines the grating lobe position. The multiport network generates the desired amplitude distribution of the sub-array.

The most successful solution implementing this method is presented by Mailloux in [21]. Each sub-array cell is is formed by three dual-mode horns, as in Fig. 1.12. The horns are connected to the feeding system through power dividers and directional couplers. The central horn results excited with an even mode, while the side ones with both even and odd modes. The ratio between the two modes is determined by the directional couplers, while the phase difference by the horn length. This network provides a good rejection of the grating lobes, but the sub-array dimension is limited to three elements and it works only with dual-mode horn antennas.

A similar, but more flexible feeding network allowing the use of any kind of antenna element was found by Skobelev in [22]. As shown in Fig. 1.13 the “chess network” consists of N cascades of directional coupler, each one comprehending a row of couplers between two adjacent cell and a row within the cell. Every sub-array is composed by $2(2N+1)$ radiating element, that can be of every kind.

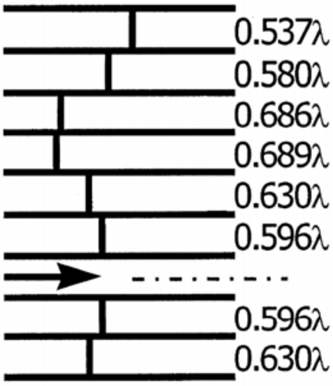

FIGURE 1.14: Array of PPW with corrugated structures [13].

Corrugated structures

Overlapped sub-arrays made of corrugated structures consist of a few active radiators, connected to the array controls, surrounded by an arrangement of passive elements, connected to a reactive load. The passive elements are excited by the mutual coupling with the active elements.

A possible implementation is shown in [13], using an array of parallel-plate waveguides (PPW). A sub-array is formed by one or two PPWs fed by a TEM mode and $10 \sim 20$ passive ones, everyone of these with a short circuit at different lengths providing the reactive load (Fig. 1.14).

1.2 Leaky-Wave Antennas in Space Applications

Leaky-wave antennas (LWAs) have been studied for decades mainly for their capability to enhance and/or modify the radiation properties of simple sources [14]. Here we focus our attention on planar 2-D LWAs, typically adopted to increase the directivity of low-directive sources, such as dipoles, patches and waveguide apertures. The structure is mainly formed by a ground plane underneath a partially reflective surface (PRS), forming a resonant cavity. For this reason, these structures are also called Fabry-Perot cavity (FPC) antennas. The source excites 2-D cylindrical leaky-waves in the cavity, propagating radially along the interface and leaking upward from the PRS. The effective area of the source results enlarged by this effect, with an enhancement of the gain [23–28] and a reduction of the SLL [29, 30].

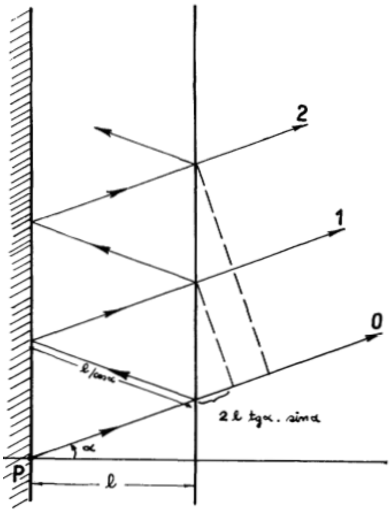

FIGURE 1.15: Electromagnetic propagation between a ground plane and a partially reflective sheet [23].

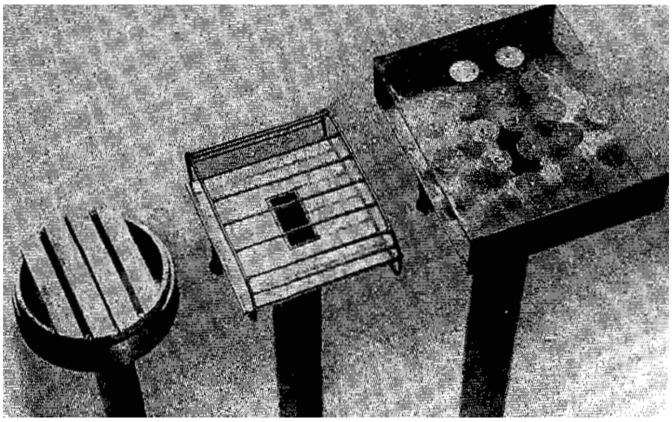

FIGURE 1.16: Prototype demonstrators of Fabry-Perot cavity antennas showed in [23].

The electromagnetic characteristics and the possibility to manufacture purely metallic structures, makes the planar LWAs suitable for space applications. This was the motivation that guided an important research branch into this topic.

1.2.1 Introduction to Planar Leaky-Wave Antennas

The first author to exploit the Fabry-Perot cavity configuration was Von Trentini in 1956 [23]. In particular, he used a structure made of a ground plane and a partially reflective sheet (Fig. 1.15) to increase the directivity of an aperture antenna. He developed a theory to explain the enhanced directivity, explaining it through the multiple reflections between the two layers. Eventually he validated the concept by measuring the three

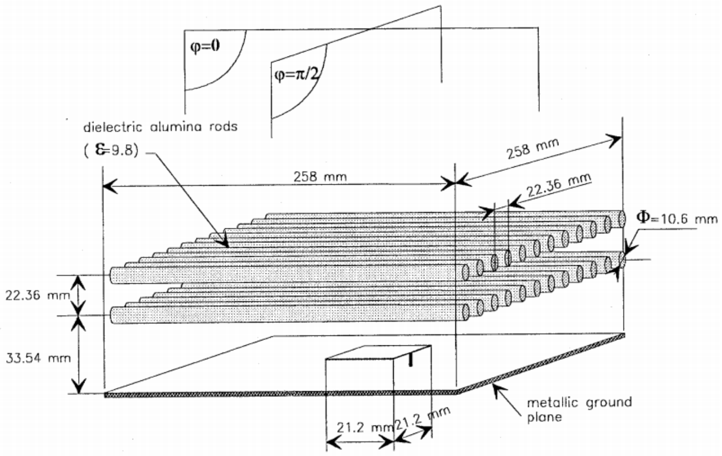

FIGURE 1.17: Prototype demonstrator of the EBG resonator antenna [32].

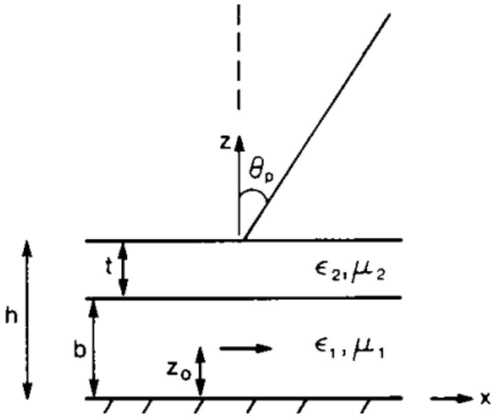

FIGURE 1.18: LWA made of two dielectric slabs above a ground plane. The structure is fed by a dipole embedded in the first dielectric.

prototypes in Fig. 1.16, made of capacitive and inductive FSS-type (frequency selective surface) impedance sheets. The measured gain of these antennas was between 14 and 17 dB at the design frequency.

The authors of [31] were the first to identify the excitation of a leaky-wave in this kind of structure, calculating the complex propagation constant and using the Kirchhoff-Huygens integration method to predict the radiation pattern. The model has been eventually validated experimentally.

In [32], the authors present the EBG (electomagnetic band-gap) resonator antenna. They use an EBG material as a superstrate to enhance the directivity of a simple patch antenna. In particular, they introduce some defects in the superstrate made of dielectric rods, creating an allowed band inside the band-gap. The gain of the antenna increases

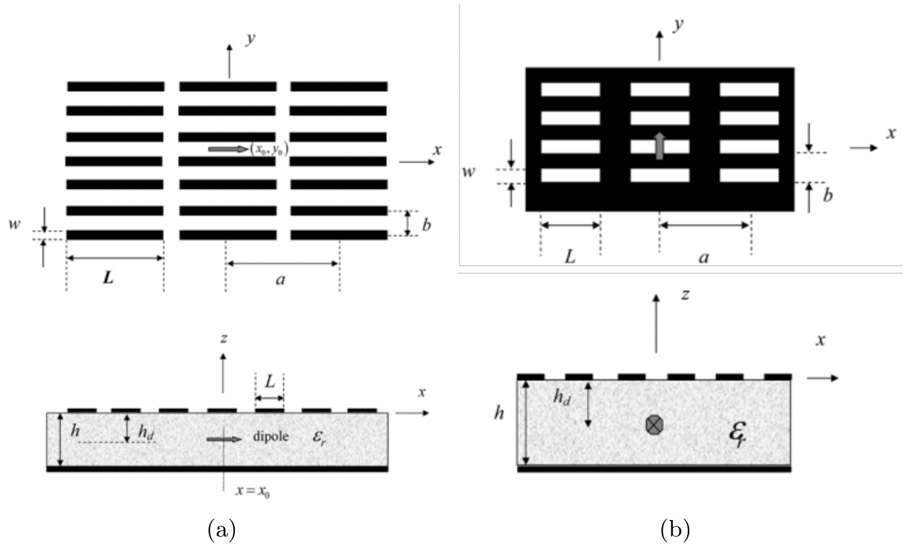

(a) (b)

Figure 1.19: LWA with capacitive and inductive PRS from [35] and [36], respectively.

by 13.5 dB by adding the superstrate. A prototype demonstrator in C-band, shown in Fig. 1.17, has been manufactured and tested, confirming the numerical prediction.

An important contribution for the analysis of 2-D LWAs has been given in [24, 33]. The authors studied a planar LWA made of a stack of dielectric slabs with different permittivities above a ground plane (Fig. 1.18). A moment method analysis procedure has been developed to predict the electromagnetic behavior of the structure with the aim to find the antenna parameters maximizing the gain. The authors gave, then, the mathematical expression to evaluate the radiation patterns of this kind of planar LWA, identifying the contribution of TE and TM modes in the radiation.

An extensive analytical study on 2-D leaky-wave antennas has been presented by the authors of [34–36]. The analytic study is performed on LWAs where the partially reflective surface (PRS) is formed by the capacitive and inductive impedance sheets (Fig. 1.19). The authors give closed expressions for the evaluation of the radiated field using a simple transmission line model.

To simplify the study of planar LWAs, an approximate analytical technique to find the dispersion equation of multi-layer stratified media is proposed in [37]. The structure under investigation is a dielectric stratification above a ground plane. The source is located at the level of the ground plane. This antenna is shown in a single slab configuration in Fig. 1.20. Its equivalent transmission line is reported in the same figure.

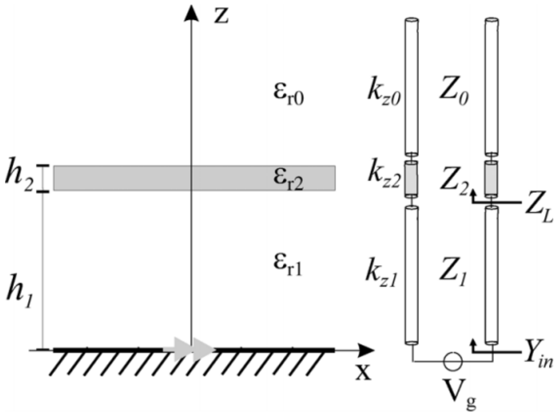

FIGURE 1.20: Planar LWA structure and its equivalent transmission line [37].

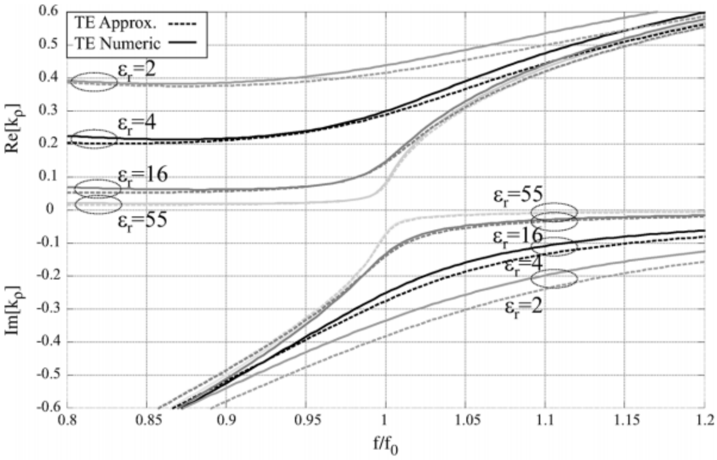

(a)

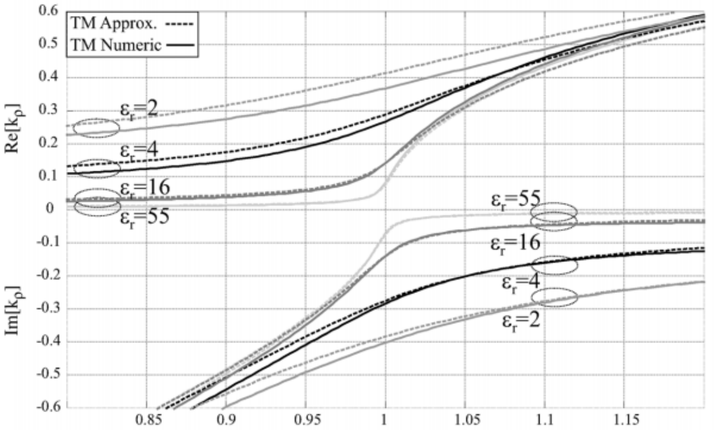

(b)

FIGURE 1.21: Dispersion diagram reported in [37] for the structure in Fig. 1.20. TE (a) and TM (b) modes.

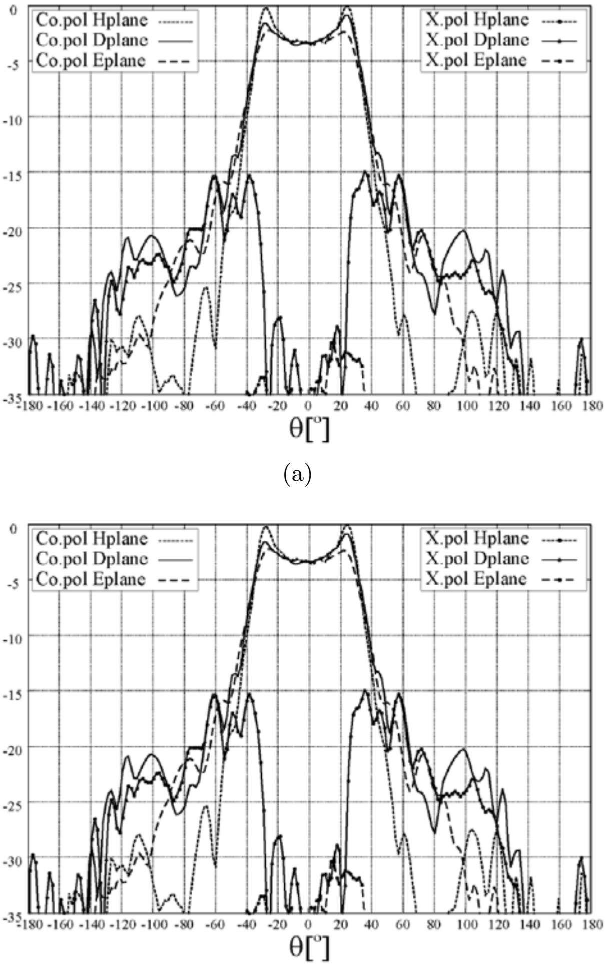

(a)

(b)

FIGURE 1.22: Measured radiation patterns at the edge of the frequency band: 9.4 GHz (a) and 10.2 GHz (b) [38].

The approximated approach has found to be very accurate. The comparison with the numerical results are shown in Fig. 1.21, where they solve the dispersion equation of the structure in Fig. 1.20. We can see in the figure the inherently dispersive behavior of leaky-wave. This behavior proves to be enhanced when using more dense dielectrics.

1.2.2 Applications on Reflector Antennas

The authors of [38] presented in 2007 a leaky-wave-based feed to improve the aperture efficiency of reflector antennas. The goal of their work was to get a radiation pattern as close as possible to a $\sec^4(\theta/2)$, the optimum distribution to illuminate the reflector. They do it by using two dielectric slabs above a small waveguide opening on a ground plane. The shaped pattern is obtained changing the leaky-wave modes of the structure,

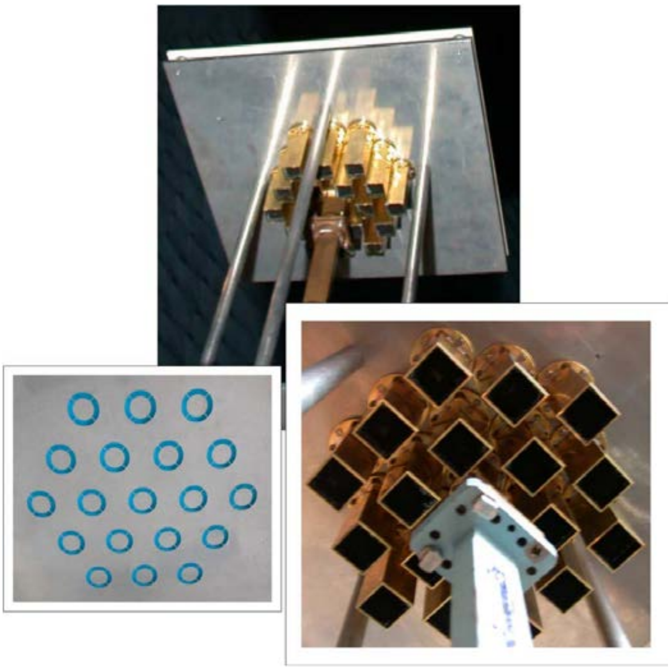

Figure 1.23: Leaky-wave feed array [39].

by opportunely tuning the parameters of the superstrate. A prototype in X-band has been tested. In Fig. 1.22 is shown the radiation pattern at 9.4 and 10.2 GHz, edges of the 8 % frequency band.

The extension to a cluster of feeds is straightforward. In fact, in [39] the authors proposed a leaky-wave feed array for reflector antennas, aiming to the improvement of the edge of coverage gain in a multiple beam scenario. The authors considered a single feed per beam design. In this configuration, the performance is typically attenuated by the reduced size of the feeds, whose maximum size is imposed by the period of the array. The superstrate, in this case, increases the effective area of each source. The edge of coverage gain results improved thanks to the reduced spillover losses due to the focalization of the main beam of each source at the center of the parabola. A prototype demonstrator has been realized in X-band and is shown in Fig. 1.23. The radiation pattern of the structure is shown in Fig. 1.24 in a 10 % band. In particular, the central element of the array is excited and all the other elements are connected to matched loads. The radiation pattern is stable in the band and the results are in line with the analytic prediction.

A similar approach is also adopted in [40] to reduce the spillover losses in a multiple beam reflector system.

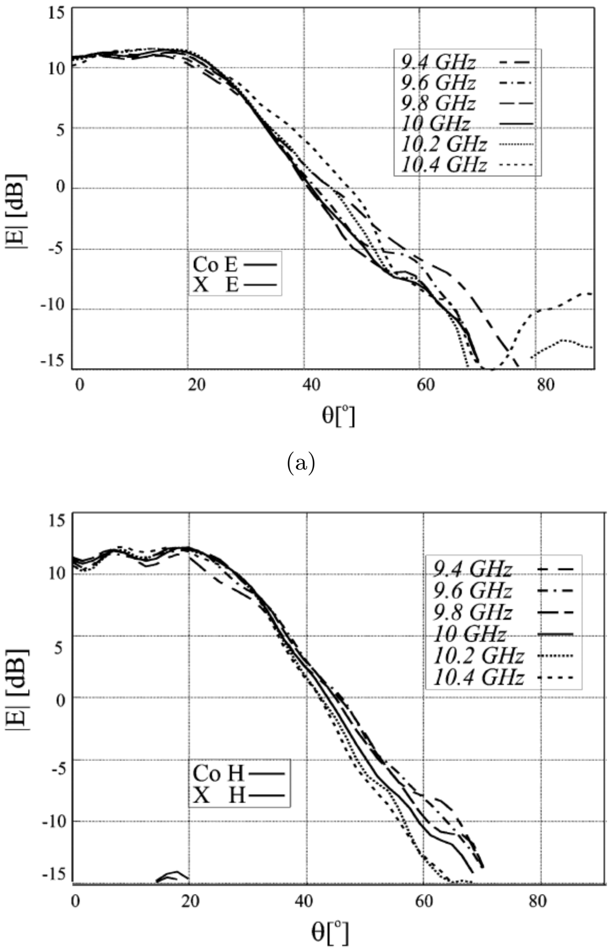

(a)

(b)

FIGURE 1.24: Measured radiation patterns in a 10 % band: E-plane (a), H-plane (b) [39].

FIGURE 1.25: EBG resonator feed for side-fed offset cassegrain antenna in Ka-band [41].

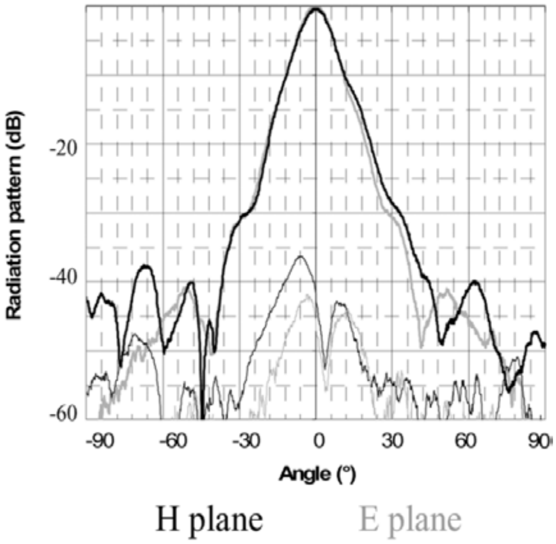

FIGURE 1.26: Measured radiation pattern at 30 GHz of the EBG resonator feed [41].

The authors of [41] proposed a feed for side-fed offset cassegrain antenna using an EBG resonator antenna (Fig. 1.25). They increased the bandwidth of the EBG resonator antenna opportunely designing the conical horn used as feed. A prototype in Ka-band has been manufactured and the radiation pattern is shown in Fig. 1.26, exhibiting very low SLL. The designed antenna has a gain of 24 dB between 29.5 and 30 GHz. The concept has been extended in [42] to a cluster of feeds for reflector antennas.

1.2.3 Applications on Phased Array Antennas

Planar LWAs have proved to be effective also in the design of array antennas. Here, multiple radiators share the same resonant cavity, allowing a partial overlap of the effective radiating surface. In this case, the main advantages of such configurations are the enhancement of the directivity and the reduction of the level of the grating lobes.

The authors of [29] presented in 2006 an extensive study on the capabilities of the Fabry-Perot cavities in the array framework. The structures considered are patch antennas on a ground plane, below a dielectric superstrate. In the first part of the paper, they show the frequency behavior using a single element, varying the permittivity and the amount of the dielectric layers. Increasing the reflectivity of the superstrate (i.e. increasing the number of dielectric slabs and/or their permittivities), the directivity and the effective

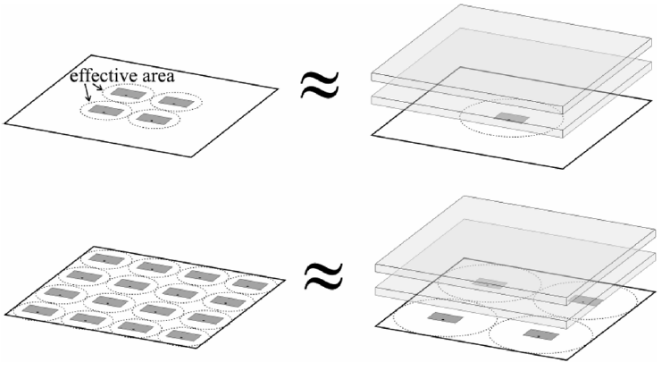

Figure 1.27: Sketch of the equivalence between a 2×2 array (with no FPC) and a single patch in an FPC (above), and between a 4×4 array and a 2×2 sparse array of patches in an FPC (below) [29].

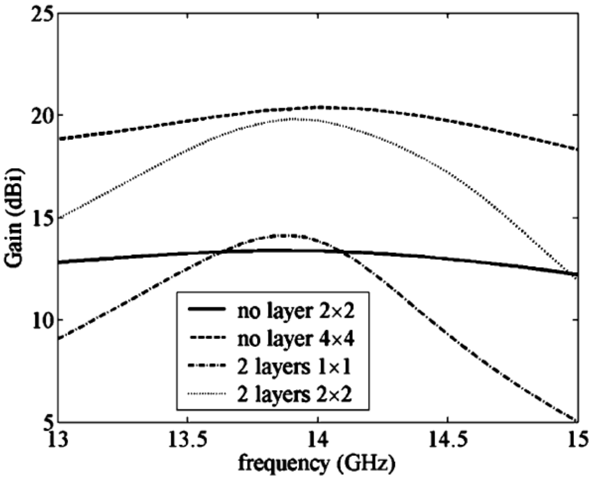

Figure 1.28: Broadside accepted Gain versus frequency. 2×2 array (continuous) and 4×4 array (dashed) of patches with no superstrate, single patch, i.e., 1×1, (dash dotted) and 2×2 array (dotted) of patches inside an FPC with $n = 2$ layers [29].

aperture increase. However, the bandwidth decreases as the reflectivity increases. Eventually, they apply this study to an array of patch antennas (Fig. 1.27). They conclude that, using the superstrate, the number of array elements can be reduced of a factor 4 maintaining the gain to comparable levels, as shown in Fig. 1.28. The results can be also extended to frequency bands other than the Ku and to different superstrate configurations.

In 2014, the authors of [30] showed the benefits of the superstrate structure applied to phased array antennas . In particular, their study is focused on the grating lobe level reduction. The structure considered is a superstrate array of waveguide apertures,

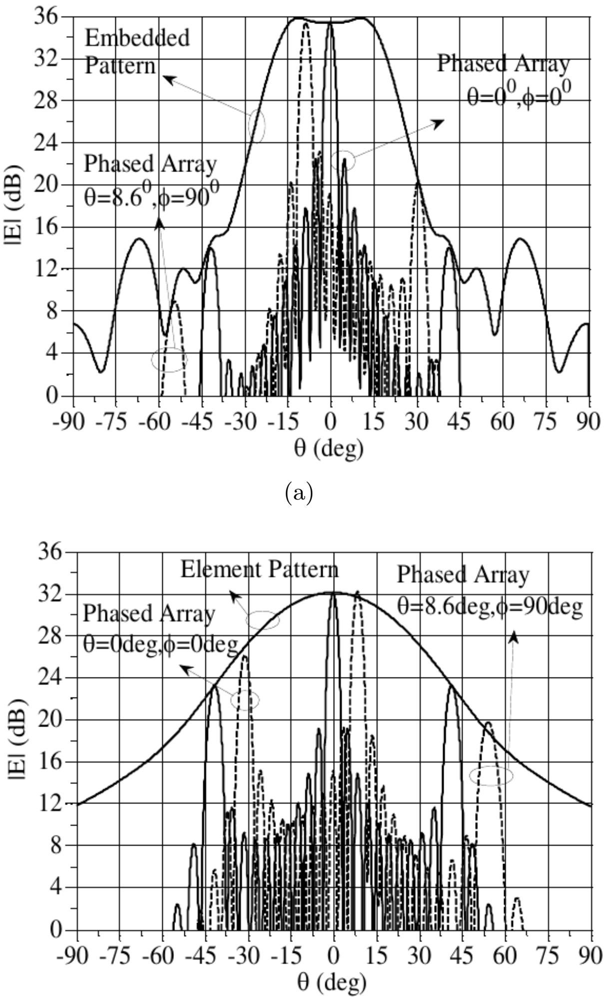

(a)

(b)

FIGURE 1.29: Radiation pattern on the E-plane of the phased array 11x11 elements: superstrate array (a) and horn array (b) at the design frequency [30].

compared with an array of horn antennas. The superstrate helps in the rejection of the grating lobe level, as shown in Fig. 1.29.

1.3 Thesis Goal

The thesis is focused upon the study of novel phased array solutions, considered one of the most promising research field for space applications. In particular, planar LWA arrays are exploited to improve the performance of classical aperture antenna arrays for space applications. As shown in the previous section, LWAs are an extremely interesting solution to increase the gain, to decrease the SLL and, more in general, to shape the radiation pattern of simple feeds.

Phased array for space applications are typically made of a huge number of sources. Analyze these structures through numerical simulations is nearly impossible and the computational time would make inefficient any kind of analysis and synthesis tool. On the other hand, a simple approach based on the array factor would not be sufficient, especially when studying structure with not negligible coupling. For these reasons, as a starting point we need a fast and reliable analytic tool able to efficiently analyze huge array structures with the minimum level of approximation. This tool also allows us to comprehend advantages and limitations of LWA arrays in terms of gain, side lobe rejection, bandwidth and mutual coupling.

Having an efficient analysis tool to study these structures, we can start to compare the LWA technology with the widely used aperture antennas. In particular, we want to understand whether it is possible to reduce the number of elements of classical aperture arrays, keeping similar performance in terms of aperture efficiency and scan capabilities.

Furthermore, we can exploit the natural characteristic of the superstrate to shape the radiation pattern, envisaging novel solutions useful for space or terrestrial applications. The shaping of the radiation pattern is possible both at element and array level.

The work has been developed in cooperation with the antenna and sub-millimetre wave section of the European Space Agency (ESA/ESTEC, 2200 AG Noordwijk, The Netherlands). The Ph.D. activity has been co-funded by ESA (co-sponsored PhD Ref. 267-2012) and Brittany Region (ARED project 2012).

The manuscript is organized as follows. In Chapter 2 we present the in-house analysis tool for planar leaky-wave antennas developed during the Ph.D. Activity. It is a fast analytic tool based on a Green's function spectral approach capable to evaluate the radiation characteristics for generic arrays of apertures over a ground plane, with or without covering superstrate. In Chapter 3 we use the electromagnetic properties of the leaky-waves to design antennas producing a desired shaped radiation pattern. In particular, the chapter is focused on the synthesis of the radiation pattern produced by a single radiator and novel synthesis methods are presented. We present in Chapter 4 a study aiming to understand if it is possible to improve the performance of classic aperture arrays for space applications using planar LWA arrays. In this chapter we focus the attention on the gain enhancement, that can lead to a reduction of the number of array elements, and bandwidth improvement. In Chapter 5 we present novel synthesis methods for planar LWA arrays. The goals are the reduction of the number of array elements and the lowering of the side lobe level envelope. Conclusions are finally drawn in Chapter 6. This chapter also discusses perspectives and possible future work.

Chapter 2

Analysis Tool for Planar Leaky-Wave Antennas

The antennas investigated during the Ph.D. activity are planar superstrate-based leaky-wave antennas. The leaky-wave modes are excited by a small radiator inside a cavity resonator, also called Fabry-Perot cavity (FPC), formed by a metallic ground plane and a partially reflective surface (Fig. 2.1). The latter is a superstrate placed above the ground plane and can be made of dielectric layers or impedance sheets, as shown in Fig. 2.2.

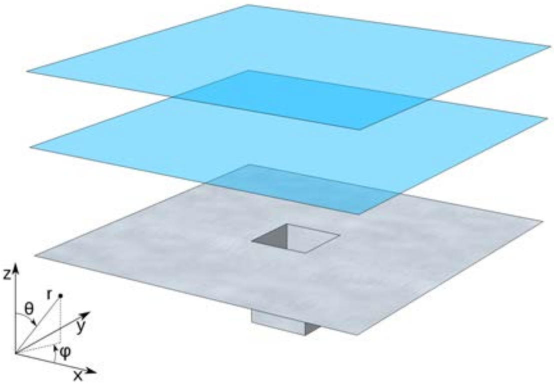

FIGURE 2.1: Planar leaky-wave antenna.

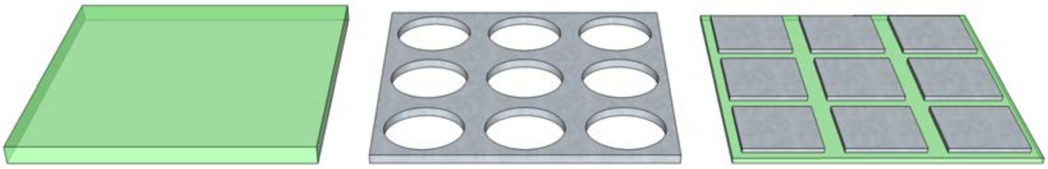

FIGURE 2.2: superstrate types: dielectric, inductive impedance sheet, capacitive impedance sheet.

2.1 Analytical Model

The deep study of the superstrate array structures and their possible innovative configurations require a fast analysis tool. It has to effectively evaluate the radiation properties of these structures in an accurate and fast way. General purpose commercial simulators are not suited for this application, as they require large amounts of resources even facing simple problems. Furthermore, in this research activity we want to analyze and synthesize electrically large arrays, possibly made of thousands of elements. For this reason we decided to develop an in-house analysis tool.

This analysis tool is based on a Green's function spectral approach. It can evaluate the radiation characteristics (radiation pattern, scattering parameters, gain, side lobe level, beamwidth) for generic arrays made of regular or irregular arrangements of generic sources (uniform apertures, waveguides, horn antennas, corrugated horn antennas) over a ground plane, with or without covering superstrate. The developed algorithm has been validated with general purpose commercial software (CST MWS, HFSS). An excellent agreement has been achieved with a drastic reduction of computation time and memory usage.

The antenna in Fig. 2.1 can be effectively analyzed using a Green's function spectral approach. To evaluate the Green's function of such a structure we can use its transmission line (TL) representation.

2.1.1 Transmission Line Model

The first step to develop an analytical model for planar leaky-wave antennas is a transmission line representation of the structure [43, 44]. The TL model allows the analytical characterization of the antenna in terms of a dyadic Green's function.

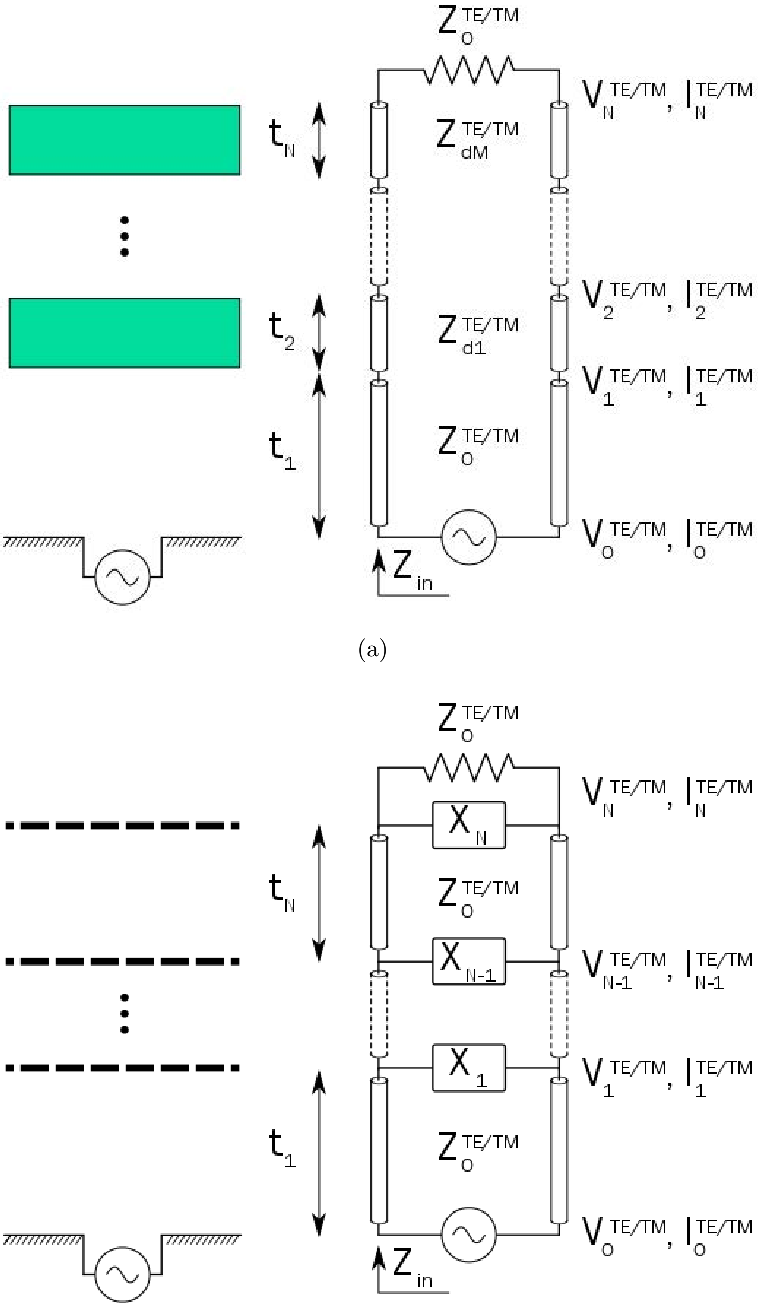

(a)

(b)

FIGURE 2.3: Transmission line model for the superstrate structure made of dielectric slabs (a) and impedance sheets (b).

The superstrate of the LWA can be made of dielectric slabs or impedance surfaces. Fig. 2.3 (a) shows the equivalent TL model for the dielectric case. A TL section is associated to each layer. The section is characterized by a length, that is the physical distance between two successive layers, and an impedance, evaluated for transverse electric (TE) and transverse magnetic (TM) modes as:

$$Z^{TE} = \eta \frac{k}{k_z} \qquad Z^{TM} = \eta \frac{k_z}{k}, \tag{2.1}$$

where $\eta = \sqrt{\mu_0/\epsilon}$ and $k_z = \sqrt{\epsilon_r k_0^2 - k_\rho^2}$ [37]. $k_\rho = \sqrt{k_x^2 + k_y^2}$ is the transverse component of the wave number k in the medium, k_0 is the free-space wave number and ϵ_r the relative permittivity of the medium considered.

The equivalent model for the impedance sheet case is reported in Fig. 2.3 (b). Each superstrate layer is associated to a shunt reactance.

The transmission line model allows an accurate description of the phenomena happening within the structure. Note that the model considers the structure infinite in the transverse direction.

2.1.1.1 Input Impedance

Refering to Fig. 2.3, the impedance at the n^{th} level of the transmission line looking upward from the generator is:

$$Z_n^{in} = Z_n \frac{Z_{n+1}^{in} + jZ_n tan(k_{z_{n+1}} t_{n+1})}{Z_n + jZ_{n+1}^{in} tan(k_{z_{n+1}} t_{n+1})}, \tag{2.2}$$

where Z_n is the characteristic impedance of the medium and Z_{n+1}^{in} is the input impedance at the $n^{th} + 1$ layer [45].

The input impedance of the antenna Z_{in} can be evaluated propagating the impedance from the upper-most layer of the transmission line to the generator. Note that the input impedance is different for TE and TM modes.

2.1.1.2 Equivalent Voltages and Currents

The equivalent voltages and currents are needed to find the parameters of the Green's function to evaluate the radiated field. Refering to Fig. 2.3, voltages and currents at the source point are related as:

$$I_0^{TE/TM} = \frac{V_0^{TE/TM}}{Z_{in}}. \tag{2.3}$$

Voltages and currents at the n^{th} layer of the transmission line can be evaluated using the formulation in [45]:

$$\begin{bmatrix} V_n^{TE/TM} \\ I_n^{TE/TM} \end{bmatrix} = \begin{bmatrix} cos(k_{z_n} t_n) & -jZ_n sin(k_{z_n} t_n) \\ -jZ_n^{-1} sin(k_{z_n} t_n) & cos(k_{z_n} t_n) \end{bmatrix} \begin{bmatrix} V_{n-1} \\ I_{n-1} \end{bmatrix}. \tag{2.4}$$

2.1.1.3 Dyadic Green's Function for Electric and Magnetic Field Radiated by a Magnetic Current

The Green's function is the tool to characterize the stratified media and is a fundamental building block in the analytic study of FPC antennas. In particular, since the feed is an aperture synthesizable with a magnetic current, we are interested in the spectral dyadic Green's function for electric and magnetic field radiated by a magnetic current.

The expression for the dyadic Green's function for the electric field $\underline{\underline{\mathbf{G}}}^{em}$ is:

$$\underline{\underline{\mathbf{G}}}^{em}(k_x, k_y, z) = \begin{bmatrix} \dfrac{k_x k_y (V_{TM}(k_\rho) - V_{TE}(k_\rho))}{k_\rho^2} & -\dfrac{(k_x^2 V_{TM}(k_\rho) + k_y^2 V_{TE}(k_\rho)}{k_\rho^2} \\ \dfrac{k_x^2 V_{TE}(k_\rho) + k_y^2 V_{TM}(k_\rho)}{k_\rho^2} & \dfrac{k_x k_y (V_{TE}(k_\rho) - V_{TM}(k_\rho))}{k_\rho^2} \\ -\dfrac{k_y V_{TM}(k_\rho)}{k_{z0}} & \dfrac{k_x V_{TM}(k_\rho)}{k_{z0}} \end{bmatrix}, \tag{2.5}$$

as reported in [46]. The couple of spectral variables k_x, k_y is related to its polar equivalent k_ρ, α as follows:

$$k_x = k_\rho \cos\alpha \qquad k_y = k_\rho \sin\alpha. \tag{2.6}$$

The $\underline{\underline{\mathbf{G}}}^{em}$ depends on the voltages of the equivalent transmission line for TE and TM modes in (2.4).

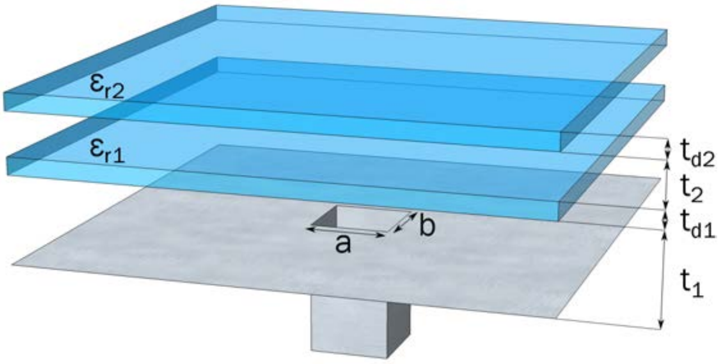

FIGURE 2.4: Example of leaky-wave antenna using a dielectric stratification. The parameters are: $a = b = 0.7\lambda_0$, $\epsilon_r = 4$, $t_1 = 0.5\lambda_0$, $t_2 = 0.25\lambda_0$ and $t_{d1} = t_{d2} = 0.25\lambda_d$.

The expression for the dyadic Green's function for the magnetic field $\underline{\underline{\mathbf{G}}}^{hm}$ is:

$$\underline{\underline{\mathbf{G}}}^{hm}(k_x, k_y, z) = \begin{bmatrix} -\dfrac{(k_x^2 I_{TE}(k_\rho) + k_y^2 I_{TM}(k_\rho)}{k_\rho^2} & \dfrac{k_x k_y (I_{TM}(k_\rho) - I_{TE}(k_\rho))}{k_\rho^2} \\ \dfrac{k_x k_y (I_{TM}(k_\rho) - I_{TE}(k_\rho))}{k_\rho^2} & -\dfrac{k_x^2 I_{TE}(k_\rho) + k_y^2 I_{TM}(k_\rho)}{k_\rho^2} \end{bmatrix}. \qquad (2.7)$$

The $\underline{\underline{\mathbf{G}}}^{hm}$ depends on the currents of the equivalent transmission line for TE and TM modes in (2.4).

2.1.2 Dispersion Equation

The dispersion equation is useful to get some physical insight on leaky-wave antennas, as it shows the frequency behavior of the transverse wave-number k_ρ. The solution of the equation shows the characteristics of the leaky-wave poles of the structure. The transverse resonance method can be used to solve the dispersion equation of the structure [44]: we choose a point on the transmission line and we impose the equality between the impedance seen looking upward and downward once the excitation is suppressed. Since this point is arbitrary, it is possible to choose it in the position of the ground plane. In this case, the problem consists in finding the zeros of the input impedance of the antenna. This task can be efficiently pursued using the Pade method described in [47]. The solutions of the dispersion equation represent the leaky wave poles $k_{lw} = k_0(\beta_{lw} + j\alpha_{lw})$ of the structure.

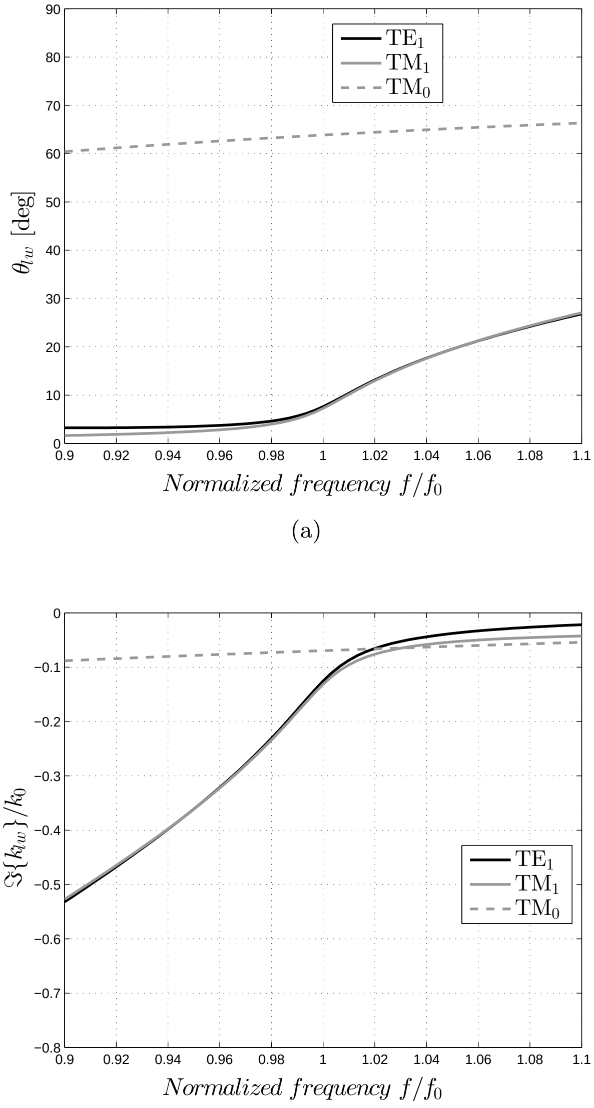

(a)

(b)

FIGURE 2.5: Dispersion diagram of the antenna in Fig. 2.4: pointing angle $\theta_{lw} \approx sin^{-1}(\beta_{lw}/k_0)$ (a) and attenuation constant α_{lw}/k_0 (b).

We introduce here the leaky-wave antenna configuration that will be used in this chapter as a benchmark. It is shown in Fig. 2.4. the antenna consists of a waveguide aperture open on a ground plane underneath two dielectric slabs. The ground plane and the superstrate form a half-wavelength resonant cavity. The two dielectric layers act like quarter wavelength transformers, decreasing the free-space impedance Z_0 of a factor ϵ_r^2 [29]. Such a structure respects the splitting condition $\alpha_{lw} = \beta_{lw}$ and radiates broadside at the design frequency [27]. The parameters of the antenna are: $a = b = 0.7\lambda_0$, $\epsilon_r = 4$, $t_1 = 0.5\lambda_0$, $t_2 = 0.25\lambda_0$ and $t_{d1} = t_{d2} = 0.25\lambda_d$, where λ_0 is the wavelength in the free-space and $\lambda_d = \lambda_0/\sqrt{\epsilon_r}$ is the wavelength in the dielectric.

The dispersion diagram for this structure is shown in Fig. 2.5 in terms of pointing angle $\theta_{lw} \approx \ sin^{-1}(\beta_{lw}/k_0)$ (a) and attenuation constant α_{lw}/k_0 (b). The main couple of leaky poles TE_1/TM_1 is responsible for the near-broadside radiation of the structure. An additional TM_0 mode is radiating close to 60°.

2.2 Single Element Configuration

2.2.1 Radiated Field

The electric and magnetic fields can be effectively expressed using the spectral dyadic Green's functions [38]. The electric field radiated in $\mathbf{r}(r,\theta,\phi)$ by a generic structure as in Fig. 2.1 can be expressed as follows:

$$\mathbf{E}(\mathbf{r}) = \frac{1}{|V|}\frac{1}{(2\pi)^2}\int_0^{2\pi}\int_0^{\infty} \underline{\underline{\mathbf{G}}}^{em}(V_{TE}, V_{TM}, k_\rho, \alpha)\cdot\mathbf{M}(k_\rho,\alpha)\, e^{-jk_{z0}z}e^{-jk_\rho\rho cos(\alpha-\phi)}k_\rho dk_\rho d\alpha. \tag{2.8}$$

V is the reference voltage and it depends on the physical dimension a and b of the feed. As reported in [48], the reference voltage is $V = \sqrt{a\,b/2}$ for a rectangular waveguide. $\mathbf{M}$ is the Fourier transform of the equivalent magnetic currents over the aperture, representing the feed. It depends just on the aperture field $\mathbf{M} = -\hat{\mathbf{n}}\times\mathbf{E}(z=0)$ [49]. $\underline{\underline{\mathbf{G}}}^{em}$ is the spectral dyadic Green's function for the electric field (2.5) evaluated at the upper most layer of the TL.

As we are typically interested in the far-field of the antenna, the asymptotic approximation of the stationary phase can be used to simplify the expression (2.8). In this case, the radiated field is:

$$\mathbf{E}(\mathbf{r}) \approx jk_0\cos\theta\frac{e^{-jk_0 r}}{|V|2\pi r}\underline{\underline{\mathbf{G}}}^{em}(V_{TE}, V_{TM}, k_\rho, \phi)\cdot\mathbf{M}(k_\rho,\phi). \tag{2.9}$$

In far-field we can assume $k_\rho = k_0\sin\theta$ and $\alpha = \phi$.

The radiation pattern obtained through (2.9) is in excellent agreement with the simulation results. We show in Fig. 2.6 the radiated electric field evaluated with the presented formulation and the results of an HFSS simulation. The structure under analysis is

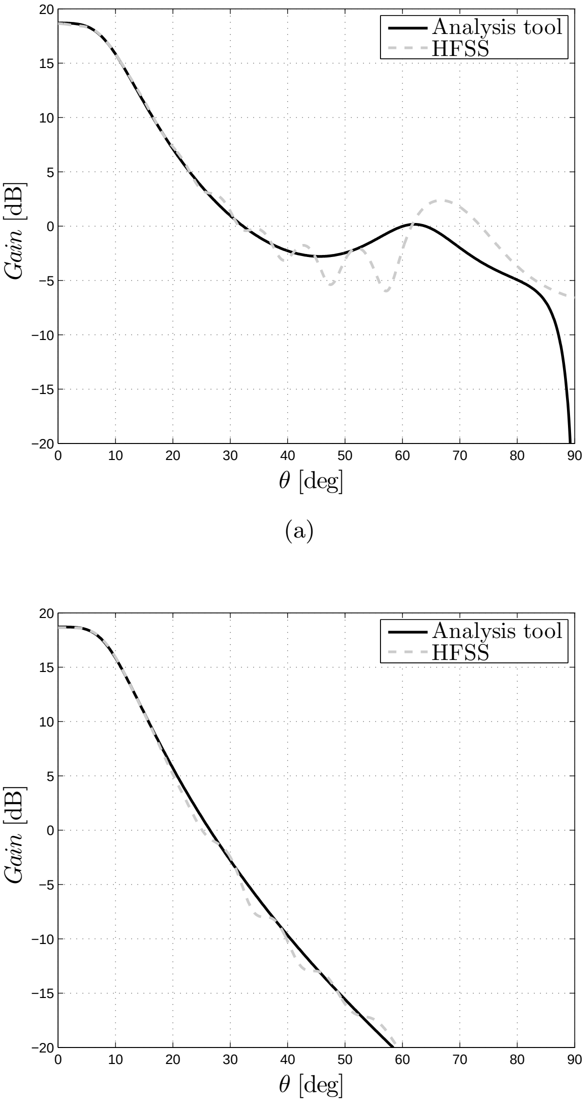

(a)

(b)

FIGURE 2.6: Radiation pattern of the antenna in Fig. 2.4 at the design frequency: E-plane ($\phi = 90°$) (a) and H-plane ($\phi = 0°$) (b)

shown in Fig. 2.4. The comparison shows an excellent agreement between the analytical procedure and the full-wave simulation. Minor discrepancies can be observed for angles far from broadside, mainly related to the finite size of the HFSS model.

The accuracy of the analytical tool allow us to generate a large number of radiation pattern in a short time, making possible the synthesis procedures that have been developed during the Ph.D. activity and that will be presented in the following chapters.

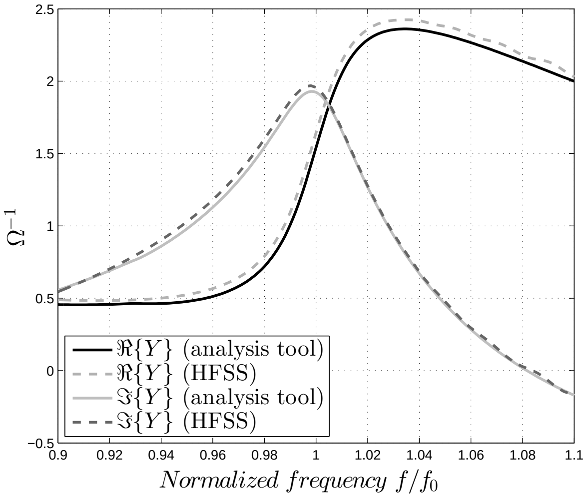

FIGURE 2.7: Input admittance of the antenna in Fig. 2.4.

2.2.2 Input Admittance

Some of the electromagnetic characteristic of the structure, such as the reflection coefficient and the gain, can be evaluated knowing the input admittance. As shown in [38], the input admittance of a planar LWA can be rigorously expressed in the spectral domain as:

$$Y_{in} = \frac{1}{|V|^2}\frac{1}{(2\pi)^2}\int_{-\infty}^{\infty}\int_{-\infty}^{\infty}|M(k_x,k_y)|^2\, G_{x,x}^{hm}(k_x,k_y,z=0)\, dk_x dk_y, \tag{2.10}$$

where $\underline{\underline{\mathbf{G}}}^{hm}$ is the spectral dyadic Green's function for the magnetic field (2.5) evaluated at the level of the source ($z = 0$). The computational time for the integral in (2.10) is $10 \sim 90$ ms on our workstation ($2 \times$ Intel Xeon E5-2650, 96 GB of RAM).

The input admittance of the structure in Fig. 2.4 is shown in Fig. 2.7. Also in this case, a very good agreement with the full wave simulation is observed.

2.2.3 Matching Network

The superstrate structure increases the reflection coefficient on the source. We addressed this problem inserting matching irises inside the feeding waveguide. Fig. 2.8 shows a matching network made of 2 capacitive irises. The parameters of the network can be evaluated using our synthesis tool. The network is modeled as a transmission line,

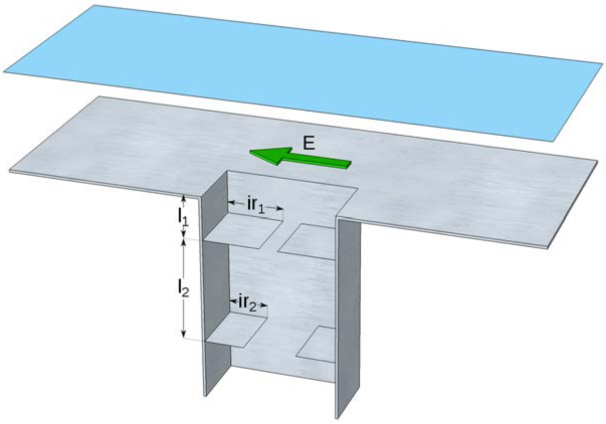

FIGURE 2.8: Section of the feeding waveguide where two irises have been embedded to match the impedance of the antenna.

where each iris is represented by shunt reactances. The transmission line is terminated on the input impedance of the antenna evaluated in Sec. 2.2.2. The parameters of the network are varied using the constrained nonlinear optimization function included in the *MATLAB optimization toolbox*, minimizing the reflection coefficient over the desired frequency band.

The maximum of the reflection coefficient for the test antenna in Fig. 2.4 is -3 dB in the considered band. Asking the synthesis tool to match the impedance in a 4 % band using two irises, it returns the following values: $l_1 = 0.14\,\lambda_0$, $l_2 = 0.87\,\lambda_0$, $ir_1 = 0.29\,\lambda_0$, $ir_2 = 0.22\,\lambda_0$. In Fig. 2.9 the effect of the matching network are presented. The reflection coefficient is lower than -10 dB in the requested band. Minor differences can be observed between the predicted and simulated curves.

2.3 Leaky-Wave Antenna Array

When embedding more than one aperture in an array configuration, the mutual coupling changes the radiation properties of the isolated element. This aspect is particularly important in the case of LWA, where the superstrate increases the mutual coupling between elements. Indeed, the mutual coupling modifies the shape of the radiation pattern and the radiation characteristics of the isolated element. The effects of the array must be taken into account to produce accurate results.

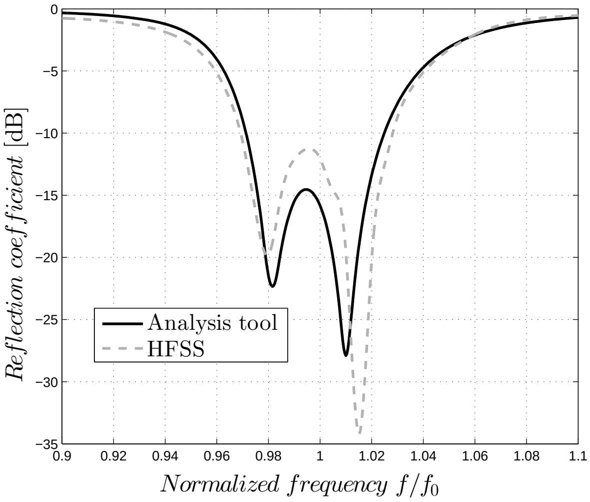

FIGURE 2.9: Reflection coefficient of the antenna after the insertion of the matching irises.

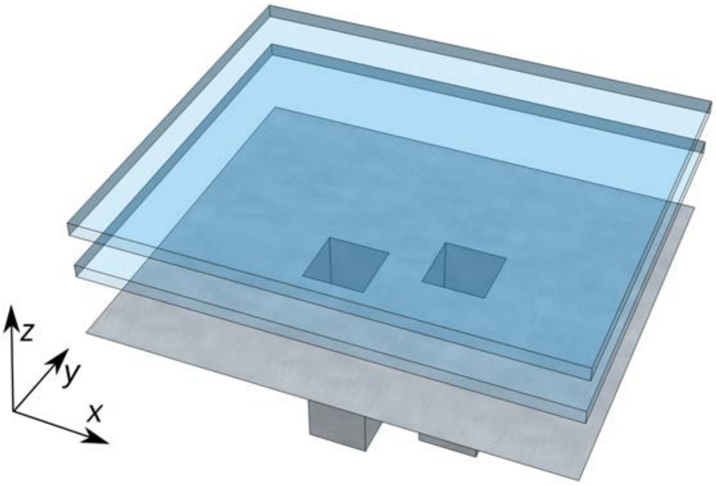

FIGURE 2.10: Example of leaky-wave antenna array using a dielectric stratification. The parameters are: $\epsilon_r = 4$, $t_1 = 0.5\lambda_0$, $t_2 = 0.25\lambda_0$ and $t_{d1} = t_{d2} = 0.25\lambda_d$. The feeds are two square waveguide apertures with side 0.7 λ_0 displaced of 1.2 λ_0 and 0.4 λ_0 in the x and y directions, respectively.

For this purpose a set of analytical functions has been developed. As shown in the following chapters of this thesis, these tools allowed us to reach results that would not be possible to achieve otherwise.

2.3.1 Radiation Pattern

The radiation pattern of the array is evaluated as the sum of the contribution of each element. The element pattern, however, is influenced by the presence of the neighbors and is different from the one of the isolated element.

Several methods can be used to calculate the array pattern with different degrees of approximation [11, 12]. The simplest way is to apply an array factor, without considering the effects of the mutual coupling. The accuracy of this approach is very poor when dealing with LWA arrays.

A second way, exploitable for regular array lattices, consists in the evaluation of the embedded element pattern in a periodic environment. The approximation considers all the elements to radiate the same pattern. An array factor is then applied. This approach works particularly well with large arrays. However it can not be applied to irregular lattices.

The most accurate way to evaluate the array pattern is calculating the actual embedded element pattern for each source. To do so, the scattering parameters of the structure are needed [50]. The sum of all the element patterns of the array gives as result the actual array pattern.

2.3.1.1 Embedded Element Pattern

The embedded element pattern of an array element is formally defined as the radiation pattern of the array when the element is excited and all the other elements are connected to matched loads [11, 12]. Considering a planar arrangement of N elements, the embedded element pattern of the n^{th} elements is:

$$\mathbf{E}_n^e(\theta,\phi) = \mathbf{E}_n^0(\theta,\phi) \cdot \left[e^{jk_0(x_n u + y_n v)} + \sum_{m=1}^{N} S_{mn} \cdot e^{jk_0(x_m u + y_m v)} \right], \tag{2.11}$$

with $u = \sin\theta\cos\phi$ and $v = \sin\theta\sin\phi$. $\mathbf{E}_n^0(\theta,\phi)$ is the field radiated by the isolated element and (x_n, y_n) its position on the array plane. S is the scattering matrix of the array. It can be analytically evaluated, as shown later in the text.

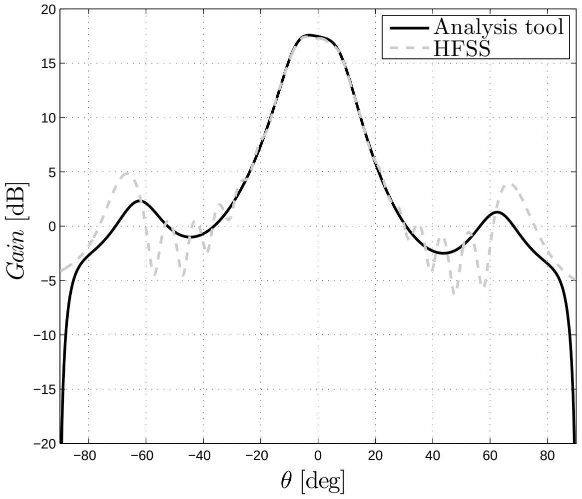

(a)

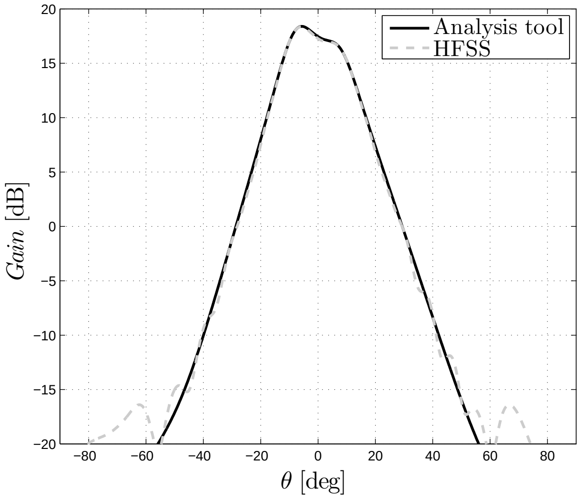

(b)

FIGURE 2.11: Embedded element pattern of the antenna in Fig. 2.10 at the design frequency: E-plane ($\phi = 90°$) (a) and H-plane ($\phi = 0°$) (b)

As an example, we evaluate the embedded element pattern of one of the elements of the array in Fig. 2.10. The distance between the two has been chosen as 1.2 λ_0 and 0.4 λ_0 in the x and y directions, respectively. The dielectric stratification and the dimension of the waveguide is the same as in Fig. 2.4. The embedded element pattern has been evaluated analytically and the results are presented in Fig. 2.11. Again, a very good agreement is observed with the full-wave simulation performed on HFSS, with some discrepancy appearing only at lower levels (20 dB below the peak directivity).

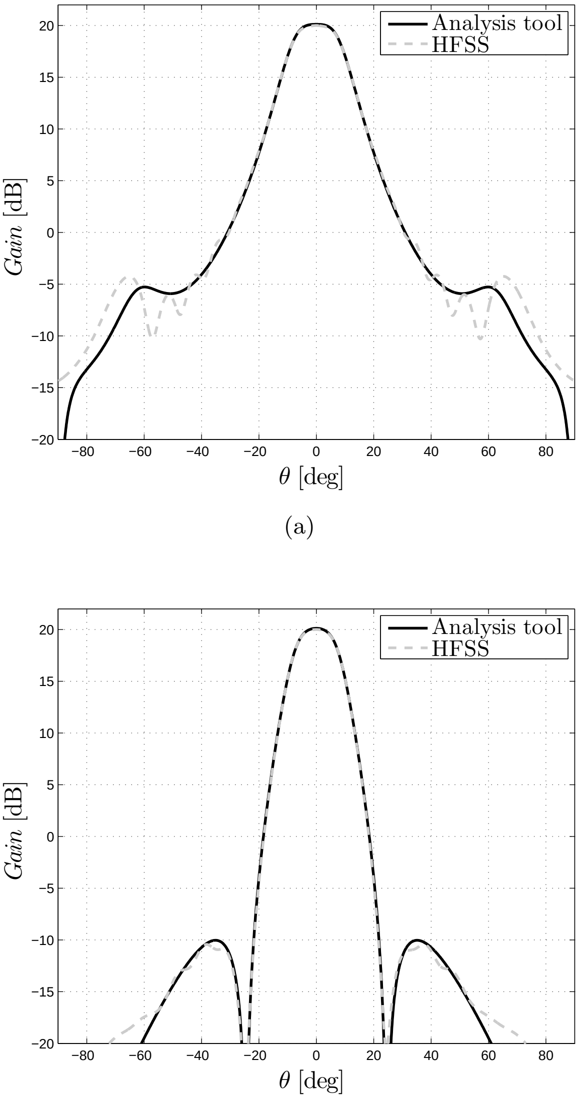

(a)

(b)

FIGURE 2.12: Array pattern of the antenna in Fig. 2.10 at the design frequency: E-plane ($\phi = 90°$) (a) and H-plane ($\phi = 0°$) (b).

2.3.1.2 Array Radiation Pattern

The array pattern can be evaluated as:

$$\mathbf{E}^a(\theta, \phi) = \sum_{n=1}^{N} \mathbf{E}^e_n(\theta, \phi) \cdot w_n, \tag{2.12}$$

where w_n is the excitation of the n^{th} array element.

The array pattern evaluated using the analysis tool and the comparison with HFSS is

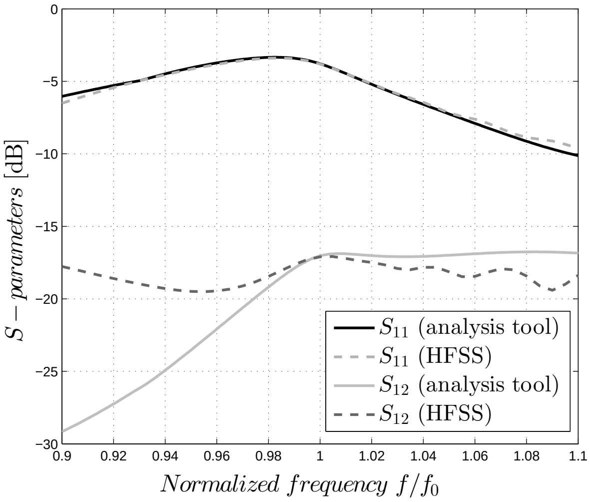

FIGURE 2.13: Scattering parameters of the antenna in Fig. 2.10.

shown in Fig. 2.12. As for the previous case, the structure under test is the one in Fig. 2.10.

2.3.2 Scattering Parameters

The evaluation of the radiation pattern in the array environment requires the calculation of the S-parameters. These can be evaluated analytically using the Green's function spectral approach.

As a first step, the admittance parameters are evaluated using the procedure outlined in [51]

$$Y_{m,n} = \frac{1}{|V|^2}\frac{1}{(2\pi)^2}\int\limits_{-\infty}^{\infty}\int\limits_{-\infty}^{\infty}|M(k_x,k_y)|^2 G_{xx}^{hm}(k_x,k_y,z=0)e^{-jk_\rho d_{m,n}}dk_x dk_y, \tag{2.13}$$

where $d_{m,n}$ is the distance between the m^{th} and the n^{th} element.

Once the Y-parameters are evaluated, the S-matrix can be computed using:

$$[S] = ([U]-[Y])([U]+[Y])^{-1}, \tag{2.14}$$

with $[U]$ the identity matrix.

Also in this case, the structure in Fig. 2.10 has been used to test the accuracy of the analytic approach. Fig. 2.13 shows the good agreement between the analysis tool and the full-wave simulation.

2.3.3 Gain

The gain of an antenna is defined as:

$$\mathbf{G}(\theta,\phi) = 4\pi \frac{|\mathbf{E}(\theta,\phi)|^2/2\eta_0}{P_{in}}, \tag{2.15}$$

where η_0 is the free-space impedance. P_{in} is the total accepted power. Considering an array of N elements, the accepted power assumes the following expression:

$$P_{in} = \frac{1}{2Z_0}\sum_{n=1}^{N} |w_n|^2 \left(1 - |S_n^{active}|^2\right). \tag{2.16}$$

Z_0 is the impedance of the feeding aperture. In the case of a waveguide excited with its TE_{10} mode, the impedance is:

$$Z_0^{TE_{10}} = \eta_0 \frac{k}{\beta}, \tag{2.17}$$

where $\beta = \sqrt{(k^2 - (\pi/a)^2)}$ is the propagation constant of the mode. Lastly we define the active scattering parameter for the n^{th} port of the array as:

$$S_n^{active} = \sum_{m=1}^{N} S_{nm}\frac{w_m}{w_n}. \tag{2.18}$$

The radiation patterns in Fig. 2.6, 2.11 and 2.12 have been evaluated using (2.15). In all the cases presented, the gain value is in excellent agreement with the simulation results.

2.4 Considerations and Limitations

Planar LWAs possess a great potential because of their unique electromagnetic properties. As presented later in this thesis, several novel applications have been found for this "classical" structure. However, some considerations have to be drawn to understand the limitations of these structures.

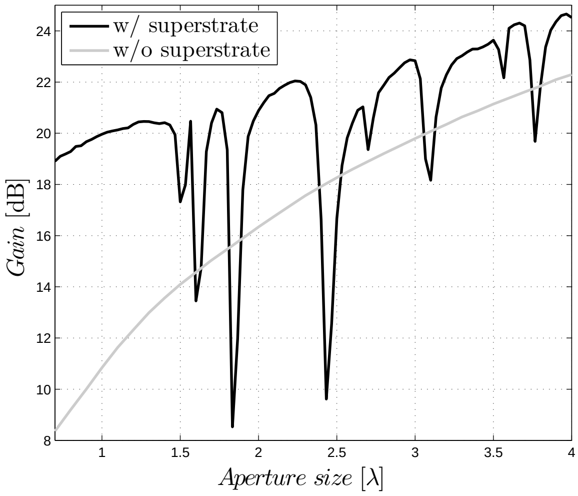

FIGURE 2.14: Gain variation with the size of the feed side (HFSS simulation). The comparison is between the leaky-wave antenna in Fig. 2.4 and an antenna without covering superstrate.

2.4.1 Bandwidth

The main, well-known drawback of the Fabry-Perot cavity antennas is the reduced bandwidth. Using a more reflective superstrate, the effective aperture and, consequently, the gain increase, but the antenna is more dispersive. Typical operational fractional bandwidths are in the order of $2 \sim 15\,\%$, depending on the requested performance [29].

2.4.2 Feed Size

The feeding aperture of the planar LWA has to be small. In literature, the side of the aperture is typically about $0.7 \sim 1\ \lambda_0$. A large aperture ($2 \sim 6\ \lambda_0$) does not allow the correct excitation of the leaky-wave modes in the cavity resonator, since the ground plane is heavily modified. A parametric study of the gain of the structure varying the dimension of the feed is shown in Fig. 2.14.

2.4.3 Mutual Coupling

The introduction of the covering superstrate increases the mutual coupling between the elements of a LWA array. The level of mutual coupling is mainly related to the reflectivity of the superstrate and the interelement distance. As shown later in the manuscript, sparse array configurations can be useful to reduce the level of mutual coupling keeping high directivity levels [29].

2.4.4 Superstrate Truncation

For proper operation the cavity requires certain dimensions in the transversal direction. These dimensions depend on the attenuation constant of the supported leaky-modes. The dimensions of the overall structure may result quite larger than the equivalent feed horn.

2.5 Summary

In this chapter we introduced the analytical in-house tool, based on a Green's function spectral approach, to study the planar LWA structures. The tool has been proven to be accurate and fast in the evaluation of the electromagnetic characteristics of the superstrate structures both for a single element and in array configuration.

All the results obtained though the analysis tool have been validated through full-wave simulations using HFSS (Finite Element Method in the frequency domain), showing an excellent agreement. The advantages in terms of computational time allow us to develop advanced synthesis tools that will be presented in the following chapters. The two main achievements are the accuracy in the evaluation of the radiation pattern, performed in a few milliseconds, and the ability to analyze array made of thousands of elements, without neglecting the mutual coupling.

Chapter 3

Element Pattern Synthesis

Leaky-wave antennas have been extensively studied in the past years for the enhancement of the gain [23, 33], the reduction of the side lobe level [29] and, more in general, for the shaping of the radiation pattern [38, 39, 52]. In this chapter, we exploit the electromagnetic properties of the superstrate to design antennas producing a desired shaped radiation pattern. In particular, we focus our attention on the synthesis of the radiation pattern produced by a single radiator, with the aim to enhance the performance of array antennas using such elements when applicable. Novel synthesis methods have been developed to reach this goal and are presented in the following.

In the fist part of the chapter, we show the synthesis tool designed to generate a leaky-wave structure producing a requested radiation pattern, given as an input through a mathematical function. The shaping is performed by opportunely tuning the design parameters of the antenna. A prototype radiating a flat-topped radiation pattern has been manufactured and tested and we show the results of the test campaign. In the second part we show the possibility to produce an asymmetric radiation pattern, such as a cosecant-squared pattern, using a truncated superstrate. Also in this case, an analytic procedure is presented.

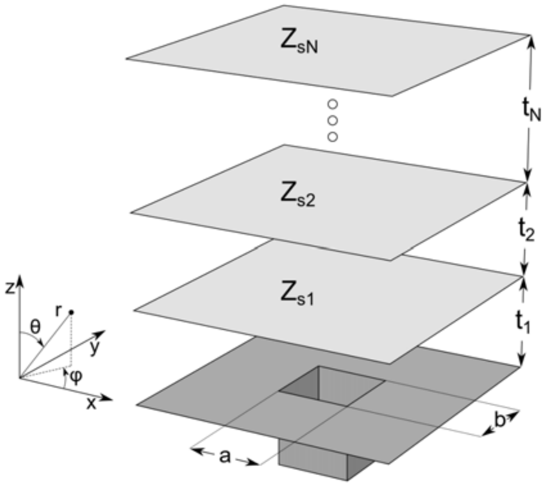

FIGURE 3.1: Superstrate configuration consisting of N impedance sheets above a ground plane. The source is a open ended waveguide with side dimensions a and b.

3.1 Radiation Pattern Synthesis Procedure for Planar Leaky-Wave Antennas

In this section we propose an optimization procedure based on the Green's function spectral approach presented in Chapter 2 to tailor the radiation pattern using planar multi-layer LWAs in a superstrate configuration. The aim is a fast analysis and design tool providing the geometrical parameters of the structure radiating the required far field radiation pattern. The spectral transmission line representation of the superstrate configuration is adopted for finely tuning the design parameters of the antenna in order to minimize the mean squared error between the target radiation pattern and the actual radiated far field. The proposed method does not require the complete knowledge of the dispersion properties of the structure under investigation [52] or any bending or shaping of its physical profile [53].

3.1.1 Optimization Procedure

The structure under investigation consists of an arrangement of impedance surfaces over a metallic ground plane, as shown in Fig. 3.1. The antenna is fed by an open-ended waveguide with its aperture on the ground plane. The impedance surfaces can be synthesized using metallic gratings [35, 54, 55], which are usually preferred to dielectric slabs for space applications. However, the proposed procedure can be used with any kind of partially reflecting screens.

The proposed procedure optimizes the design parameters of the antenna, namely: the surface impedances Z_{si}, their spacings t_i and the size of the feeding aperture a, b. The core of the optimization procedure is the minimization of the mean squared error (MSE) between the actual radiated electric field distribution and a target function:

$$MSE = \int_0^{\theta_c} \left(|\mathbf{F}_i(\theta, \phi_0)| - |\mathbf{F}_e(\theta, \phi_0)| \right)^2 d\theta, \tag{3.1}$$

where θ_c represents the angular region under consideration. $\mathbf{F}_e(\theta, \phi_0)$ is the radiation pattern of the antenna under investigation. It is analytically evaluated through the equation (2.9), speeding up the computational time of the optimization tool. The target function $\mathbf{F}_i(\theta, \phi_0)$ is a mathematical function in the angular domain representing the ideal radiation pattern.

During the optimization, the parameters of the structure are varied in order to find a minimum of the MSE. This operation is performed with the aid of the constrained nonlinear optimization function included in the *MATLAB optimization toolbox*. An initial guess is needed to start the nonlinear optimization. In the present work, the initial guess is found by treating the radiation pattern as the frequency response of a Chebyshev bandpass filter in the angular domain, as shown in the following. At each iteration, the radiation pattern of the resulting antenna is evaluated and compared with the target function. The process ends when a minimum of the MSE is found.

It is worth noting that the number of impedance sheets N could be introduced as a variable in the optimization process. However, since it affects both the bandwidth [29] and the complexity of the antenna, it is convenient to define it *a priori* based on the requirement of the particular application.

Initial Guess

The evaluation of the initial guess is a preliminary step that takes place before entering in the optimization loop. The initial solution must provide an acceptable starting point for the synthesis tool. A procedure similar to the one described in [56] has been implemented to find the initial guess.

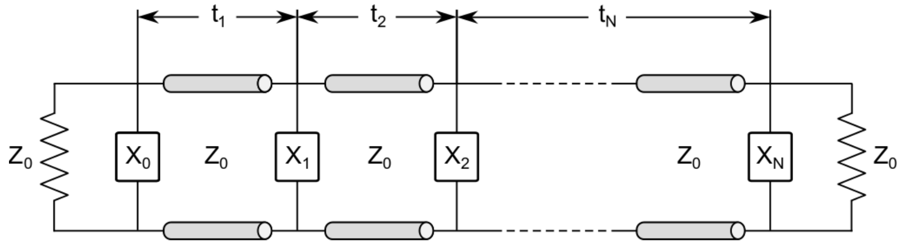

FIGURE 3.2: Transmission line model of the shunt-inductance-coupled waveguide filter.

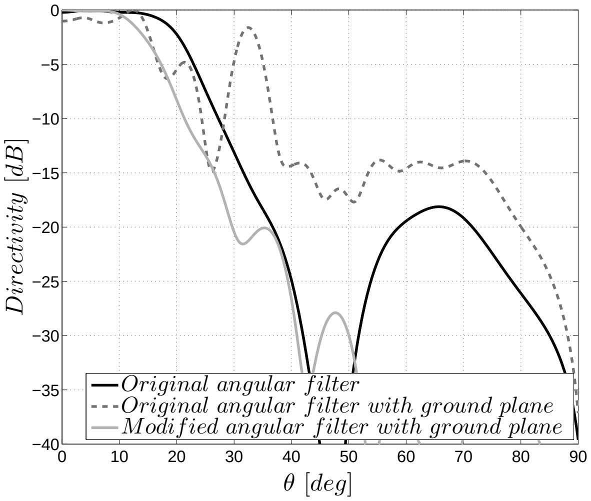

FIGURE 3.3: Simulated radiation patterns of the filter in E-plane ($\phi = 90°$) in its original and modified versions. In the first case, the filter is illuminated by an open ended waveguide placed at a distance of $\lambda_0/2$ from the first impedance surface. In the second case, the distance between the source and the stratification remains the same, but the waveguide aperture is open on a ground plane. In the third case, the first impedance is replaced with a ground plane, hosting the feeding open ended waveguide. In the three cases, the feeding waveguide has a square aperture ($a = 0.7\,\lambda_0$).

The superstrate is treated like a Chebyshev-like shunt-inductance-coupled bandpass filter (Fig. 3.2). The frequency response of the filter is defined as a function of the angular variable θ to move the problem from the frequency to the angular domain.

The transfer function of a filter of order N is related to the values of the impedance inverters K_0, $K_1, ...,$ K_N, as in [57]

$$\begin{aligned} \frac{K_0}{Z_0} &= \sqrt{\frac{\pi}{2}\frac{\omega_\lambda}{g_0 g_1}}, \\ \left.\frac{K_j}{Z_0}\right|_{j=1 \text{ to } N-1} &= \frac{\pi\omega_\lambda}{2}\frac{1}{\sqrt{g_j g_{j+1}}}, \\ \frac{K_N}{Z_0} &= \sqrt{\frac{\pi}{2}\frac{\omega_\lambda}{g_N g_{N+1}}}, \end{aligned} \tag{3.2}$$

where the coefficients $g_0,\ g_1, ...,\ g_{N+1}$ are given in [57]. $\omega_\lambda = 2(\lambda_2 - \lambda_1)/(\lambda_2 + \lambda_1)$ is the guided-wavelength fractional bandwidth. The terms λ_1 and λ_2 are the guided wavelengths at the boundary of the bandpass frequency region. We define these values as a function of θ, yielding:

$$\lambda_1 = \lambda_0, \qquad \lambda_2 = \frac{\lambda_0}{cos(\theta_r)}, \tag{3.3}$$

where λ_0 is the free space wavelength. The radiation pattern will have an angular range equal to $2\theta_r$. Z_0 is the waveguide characteristic impedance:

$$Z_0 = \frac{k_c}{\beta} \cdot \eta, \tag{3.4}$$

where η is the characteristic impedance of the medium, $\beta = \sqrt{k^2 - k_c^2}$ is the propagation constant and $k_c = \sqrt{(m\pi/a)^2 + (n\pi/b)^2}$ is the cut-off wave number.

Fig. 3.2 shows the equivalent transmission line of the shunt-inductance-coupled filter. The values of the reactances $X_0,\ X_1, ...,\ X_N$ and the distances $t_1,\ t_2, ...,\ t_N$ between them can be evaluated using the well known formulas in [57]:

$$\left.\frac{X_j}{Z_0}\right|_{j=0 \text{ to } N} = \frac{\frac{K_j}{Z_0}}{1 - \left(\frac{K_j}{Z_0}\right)^2}, \tag{3.5}$$

$$\left.t_i\right|_{i=1 \text{ to } N} = \frac{\lambda_0}{2} - \frac{\lambda_0}{4\pi}\left[tan^{-1}\left(\frac{2X_{i-1}}{Z_0}\right) + tan^{-1}\left(\frac{2X_i}{Z_0}\right)\right]. \tag{3.6}$$

The values of the superficial impedances used as initial guess for the leaky-wave structure correspond to the reactance values in (3.5). In the same way, the distances between the layers are those obtained from (3.6).

Angular filters designed with this method have radiation patterns in line with the specifications. Nevertheless, the synthesized structure is not the Fabry-Perot cavity in Fig. 3.1. Effects and position of the ground plane are not taken into account during the design process. The insertion of the ground plane dramatically alters the shape of the radiation pattern.

Let us consider a filter made of three layers with an angular range $\theta_r = 15°$. Equations (3.5) and (3.6) give us the values of reactance and distance between the layer in Table 3.1.

TABLE 3.1: Parameters of the filter with $N = 3$ and $\theta_r = 15°$ (Fig. 3.2) obtained through equations (3.5) and (3.6).

X_0	X_1	X_2	t_1	t_2
$115\,\Omega$	$47\,\Omega$	$115\,\Omega$	$0.44\,\lambda_0$	$0.44\,\lambda_0$

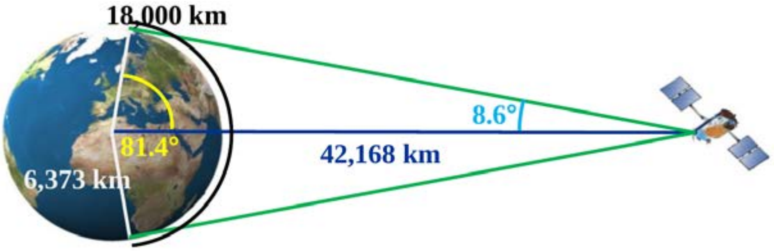

FIGURE 3.4: Simulat.

We illuminate this structure with an open ended waveguide at a distance $\lambda_0/2$ from the first impedance. The simulated radiation pattern of this structure is reported by the black curve in Fig. 3.3. The effects of the the insertion of a ground plane at the location of the waveguide leads to a degradation of the filtering characteristics. The radiation pattern is shown by the dashed curve in Fig. 3.3. Such degradation decreases as we move ground plane and source closer to the first impedance. In the limit case where the first impedance (X_0 in Fig. 3.2) is replaced by the ground plane and source, the radiation pattern will appear as the gray curve in Fig. 3.3. The beam is sharper than requested, but it is suitable as a starting point for the optimization procedure.

3.1.2 Flat-topped Radiating Structure

The optimization procedure proposed above is used here to design a flat-topped radiation pattern, suited as element pattern of a phased array steering its main beam in a given field of view. Flat-topped radiation patterns are generally adopted to provide uniform illumination over a defined angular region and low side lobe levels [58]. Phased array configurations of sources radiating flat-topped patterns are of interest for the reduction of the scan losses and side lobe levels, including grating lobes, over a defined field of view [30, 59]. These characteristics are suitable for on-board geosynchronous satellite applications, where a uniform illumination of the Earth and an efficient use of the available energy are required. The visible surface of the Earth from the GEO (geostationary Earth orbit) satellite corresponds to an angle $\theta_E = \pm 8.6°$, as shown in

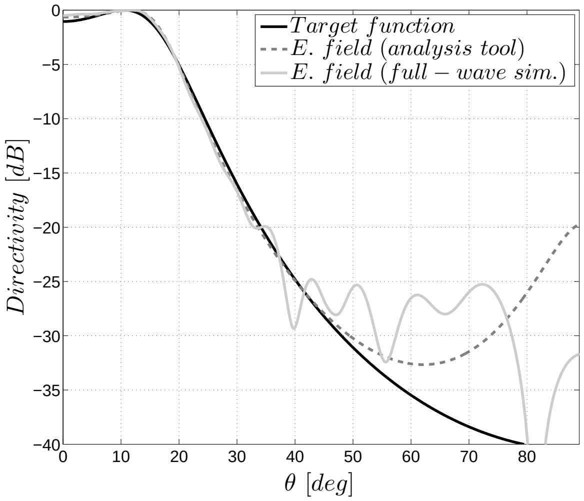

FIGURE 3.5: Flat-topped radiation pattern in E-plane ($\phi = 90°$). The black curve represents the analytical function to be approximated. The normalized far-field radiation pattern of the optimized structure evaluated using the in-house analysis tool and full-wave simulations are shown in dashed gray line and solid gray curve, respectively.

Fig. 3.4. The flat-topped characteristic is particularly useful in arrays with a periodicity larger than λ affected by the appearance of grating lobes in the visible range [59].

One of the first attempts to synthesize a flat-topped radiation pattern using a layered dielectric structure has been performed by Mailloux in [60]. In this work, a dielectric stratification was employed as a spatial filter in order to obtain a Chebyshev-like radiation pattern. Franchi and Mailloux followed a similar approach to obtain an angular filter using metallic grids [56] instead of dielectric slabs. In both cases, the design was performed using classical filter design techniques that did not take into account the actual nature of the sources used in the design. The idea was to apply the well-known formulas for Chebyshev band-pass filters, moving the problem from the frequency to the angular domain to derive the design parameters of the radiating structure. The solution proposed in [56], presented in Section 3.1.1, is the starting point of our optimization procedure for the flatted-topped case. However, as a difference with [56], the real spectral transmission line representation of the superstrate configuration is adopted for the evaluation of the radiated far field taking into account the position and nature of the feeding sources, leading to more accurate results and general procedure.

In the present case, the angular range to be uniformly covered is $\theta_E = \pm 8.6°$, which corresponds to the visible surface of the Earth on geostationary satellites. The operating

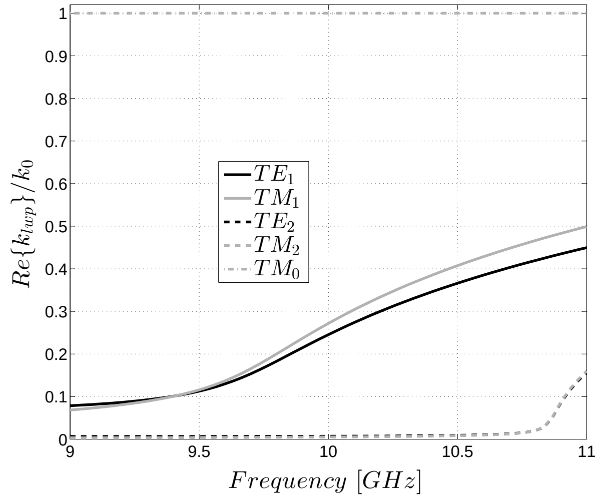

(a)

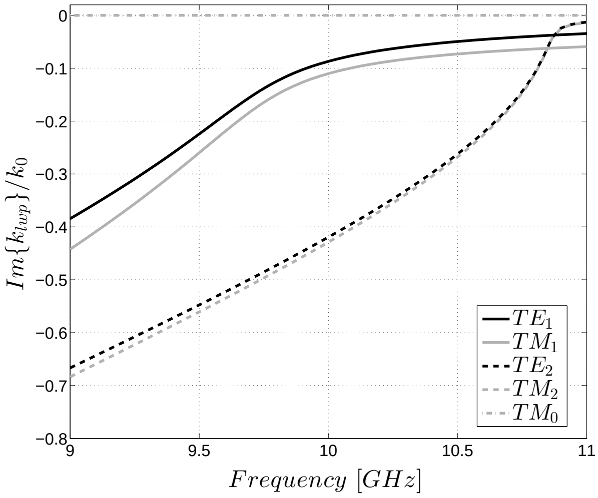

(b)

Figure 3.6: Dispersion diagrams for the LWA generating a flat-topped radiation pattern. (a) Real part of the propagation constant expressed in radiation angles. (b) Normalized attenuation constant.

frequency is chosen equal to $f_0 =$ 10 GHz. The number of layers N has been set equal to 2, allowing good performance over a fair bandwidth as well as a suitable roll-off. The latter determines the grating lobe rejection, once the feed is used in the array framework. Note that the following requirements has been chosen as an example and other specifications may be provided based on the considered application.

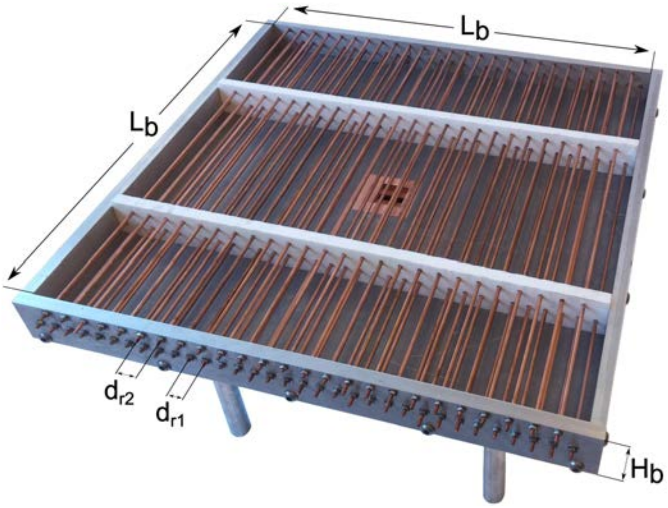

(a)

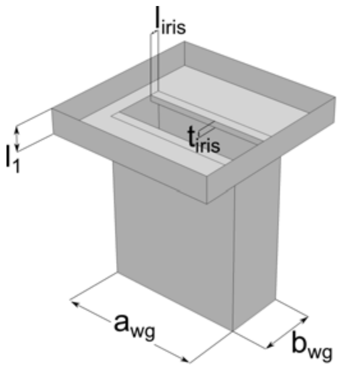

(b)

FIGURE 3.7: (a) Realized prototype. (b) Pictorial view of the radiating aperture and corresponding matching network.

The target function $\mathbf{F}_i(\theta, \phi_0)$ to be approximated in the angular range up to $\theta_c = 40°$ by the radiation pattern, has been chosen equal to

$$\mathbf{F}_i(\theta, \phi_0) = \frac{1}{1 + A\ T_{2N}\left(\dfrac{sin\theta}{sin\theta_r}\right)}, \tag{3.7}$$

with T_{2N} the Chebyshev polynomial of the first kind and order $2N$. In the following, N corresponds to the number of impedance sheets. The amplitude of the ripple of the target function is equal to $2A$, while θ_r corresponds to half of the equal-ripple band edge.

Here, we consider $N = 2$, with $\theta_r = 15°$ and $2A = 0.12$, corresponding to a ripple of $\sim 1\,\mathrm{dB}$. The target function $\mathbf{F}_i$ evaluated with these parameters is shown in Fig. 3.5. The value of θ_r, selected at the design frequency, has been chosen larger than the requested θ_E

in order to account for the dispersive behavior of the structure and resulting beamwidth variation with frequency over a typical operating band of about 7 %. This is further discussed at the end of this section, based on the dispersion analysis results. The values of the initial guess of the optimization are reported in Table 3.1. The corresponding radiation pattern is shown by the gray curve in Fig. 3.3. Note that the optimization has been performed in E-plane ($\phi_0 = 90°$) of the LWA. This plane is the most critical one for superstrate configurations due to the presence of a leaky-wave mode radiating close to endfire [25–27, 29, 30, 33, 35, 36, 38–40, 61]. On the other hand, the azimuthal symmetry of the configuration will assure good radiation performance in all field cuts once the E-plane fulfills the imposed requirements on the radiation pattern [38, 40].

The computational time necessary to perform the whole optimization is less than two seconds on our workstation ($2 \times$ Intel Xeon E5-2650, 96 GB of RAM). The structure generated by the optimization process consists of two impedance sheets with $Z_{s1} = j\,34.8\ \Omega$, $Z_{s2} = j\,115.2\ \Omega$ separated by distances $t_1 = t_2 = 13.52$ mm (Fig. 3.1). The feed is a square waveguide [30, 38–40] whose side has a length of $a = 27$ mm. Fig. 3.5 shows the normalized electric field evaluated by the optimization tool and by the full-wave simulator ANSYS HFSS in E-plane ($\phi = 90°$). A good agreement is observed between our tool and full-wave simulations. The simulation has been performed using two ideal impedance sheets. The lateral size of the antenna is equal to 30 λ_0 (with λ_0 free-space wavelength) with negligible edge effects.

To gain a better understanding of the physical operation of the antenna, the dispersion diagrams for the proposed structure are illustrated in Fig. 3.6. These curves have been obtained by deriving the solutions of the dispersion equation associated to equivalent transmission line representation of the structure. The procedure is extensively discussed in Section 2.1.2. In particular, the real and imaginary part of the transverse propagation constant $k_\rho = Re\{k_{lwp}\} - j\,Im\{k_{lwp}\}$ are plotted. Several TE/TM leaky-wave modes are found. In particular, the couple of leaky-wave modes TE_1/TM_1 radiates close to 15° at the design frequency ($\theta_{lwp} \approx\ sin^{-1}(\beta/k_0)$) and is mainly responsible for the shape of the pattern. In fact, the couple TE_2/TM_2 is in cut-off at the central frequency, whereas the TM_0 mode is radiating endfire in E-plane. Additionally, the variation of the radiating angle with frequency for the modes TE_1/TM_1, as reported in Fig. 3.6(a), clearly indicates that the lower operating frequencies are driving the minimum achievable beamwidth. Oversizing the field-of-view at the design frequency enables to remain compliant with a

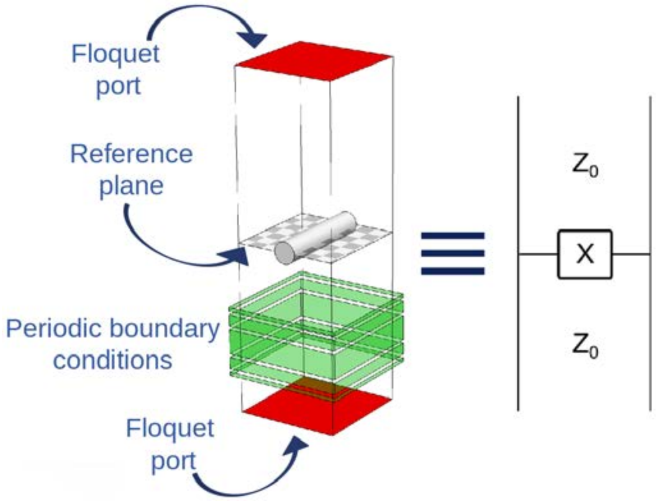

FIGURE 3.8: On the left, HFSS simulation setup used to synthesize the value of reactance for each impedance sheet using metallic rods. A single metallic rod is embedded in a cell with periodic boundary conditions, fed in the longitudinal direction by two Floquet-ports with the reference plane at the center of the rod. The equivalent transmission line is shown on the right.

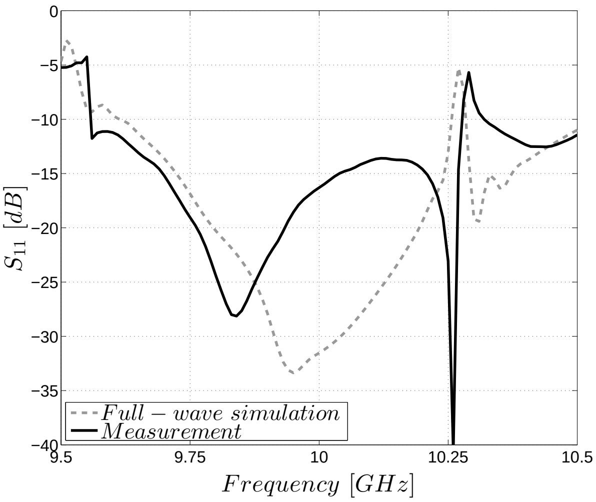

FIGURE 3.9: Simulated and measured reflection coefficient.

uniform coverage over the Earth at the lowest operating frequencies, around 9.6 GHz for the proposed design.

3.1.2.1 Prototype and Measurements

The flat-topped antenna designed in the previous section has been manufactured and tested at IETR. The prototype is shown in Fig. 3.7.

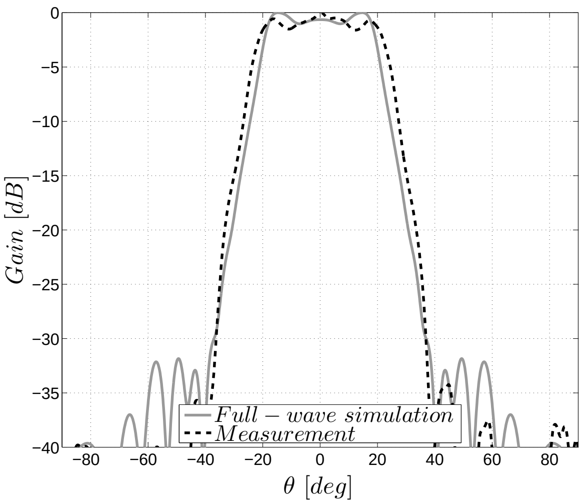

(a)

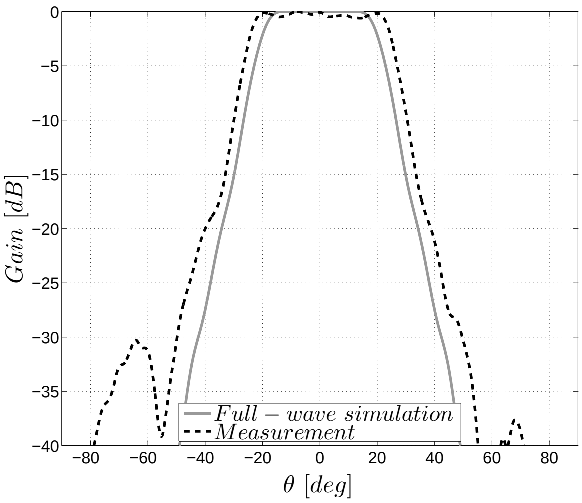

(b)

FIGURE 3.10: Simulated and measured radiation patterns at the design frequency (10 GHz). (a) E-plane ($\phi = 90°$). (b) H-plane ($\phi = 0°$).

The impedance sheets have been synthesized using a periodic arrangement of metallic rods. HFSS full-wave simulations have been used to synthesize the required value of reactance for each layer. The simulation setup is shown in Fig. 3.8 (left). A single metallic rod is embedded in a cell with periodic boundary conditions in the transverse direction. The cell is fed in the longitudinal direction by two Floquet-ports with the reference plane at the center of the rod. This setup is equivalent to transmission line in Fig. 3.8 (right). The Z-parameters of the simulation correspond to the impedance of the rod. The metallic rods used for the protoype are made of copper with a diameter equal

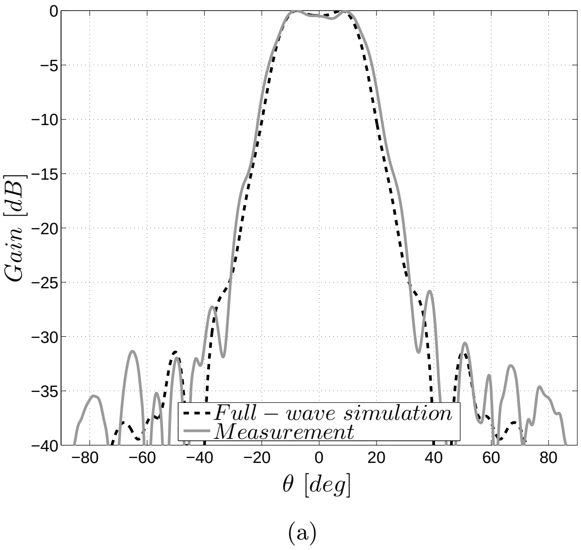

(a)

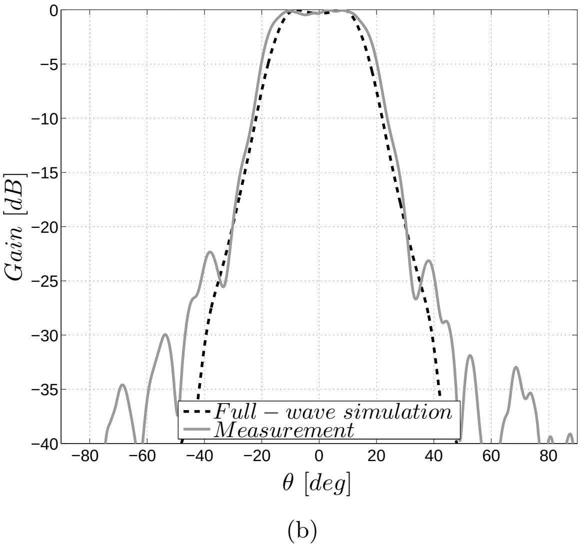

(b)

FIGURE 3.11: Simulated and measured radiation patterns at 9.6 GHz, the lower edge of the band of operation 10.2 GHz. (a) E-plane ($\phi = 90°$). (b) H-plane ($\phi = 0°$).

to 3 mm. The final periodicity for the required impedance sheets are $d_{r1} = 12.25$ mm and $d_{r2} = 15.48$ mm for the first and the second layer, respectively. The behavior of these impedance layers is therefore inherently dispersive. In particular, the reactance of the sheet impedance varies by less than 10 % (with respect to the nominal value at the operating frequency) within the considered band. Such a variation does not affect the overall performance of the antenna.

A metallic box has been placed around the antenna to support the rods. The height of the box is $H_b = 31$ mm and the lateral size is $L_b = 408$ mm. The latter has been

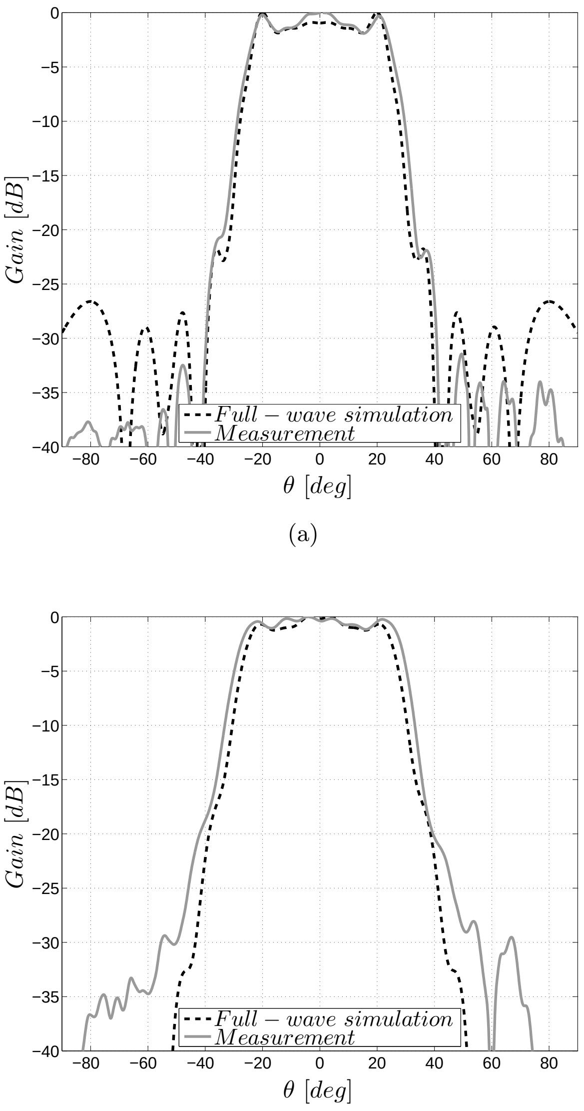

(a)

(b)

FIGURE 3.12: Simulated and measured radiation patterns at 10.2 GHz, the upper edge of the band of operation. (a) E-plane ($\phi = 90°$). (b) H-plane ($\phi = 0°$).

chosen through a parametric analysis in such a way to minimize the SLL in E-plane. A metallic box has been placed around the antenna to support the rods. Two bars of Rohacell (relative permittivity $\epsilon_r = 1.067$) have been placed within the metallic box of the final prototype to reduce the bending of the rods.

Fig. 3.7(b) shows a pictorial view of the feeding structure. The square waveguide used as source is connected to a standard WR-90 waveguide through a matching iris. The thickness and length of the iris are $t_{iris} = 1$ mm and $l_{iris} = 1.54$ mm, respectively. The height of the square waveguide section is $l_1 = 4.17$ mm. The simulated and measured

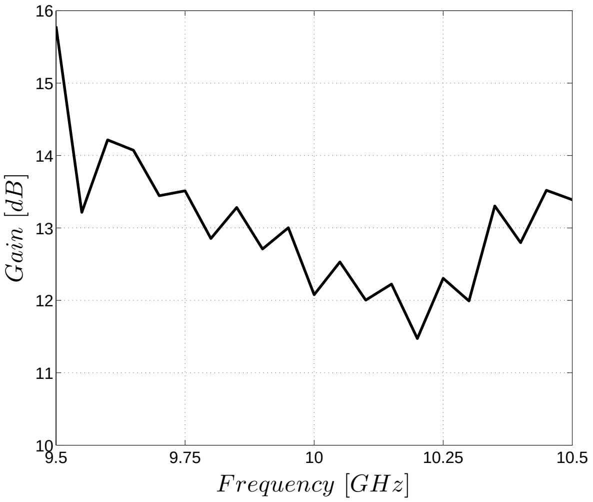

Figure 3.13: Frequency dependence of the measured broadside gain.

reflection coefficients are shown in Fig. 3.9. In both cases, the reflection coefficient is lower than -10 dB over the same 7.5 % band. However, we observe some discrepancies between the two curves that can be attributed to manufacturing imperfections and residual bending of the copper rods. Nevertheless, the results are considered acceptable.

In Fig. 3.10 we compare the simulation results with the measurements at the design frequency. A good agreement is obtained between the curves. A flat-topped radiation pattern has been achieved with a good roll-off figure. Small asymmetries can be observed in the measured radiation patterns attributed to the residual bending of the copper rods. The measured gain is equal to 12.1 dB at broadside, 1.8 dB lower than the simulated one. The discrepancy is mainly related to the beamwidth, larger in the measurements.

The comparison between simulated and measured radiation patterns at 9.6 GHz and 10.2 GHz, the edges of the considered band, are shown in Fig. 3.11 and Fig. 3.12, respectively. Also in this case, a good agreement is obtained between the predicted and measured results. The flat-topped shape is preserved within the considered band, with the beamwidth increasing with the frequency. Side lobe levels and roll-off values maintain excellent performance within the band.

The measured broadside gain is reported in Fig. 3.13 with value of 14.2 dB and 11.5 dB at the lower and upper edges of the band $9.6-10.2$ GHz, respectively. The gain remains quite stable in the band.

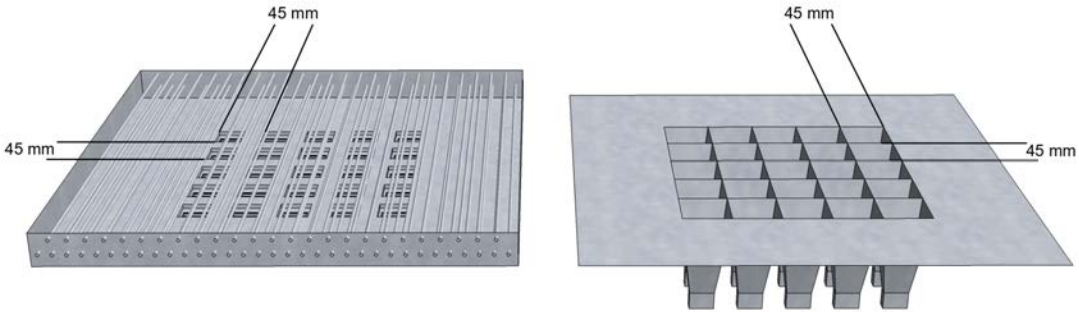

FIGURE 3.14: Structures of the 5 × 5 elements LWA array (left) and 5 × 5 elements benchmark horn array (right).

3.1.2.2 Array Performance

Finally, we simulated using HFSS the radiation pattern of an array of 5 × 5 square waveguides ($a = 27$ mm) arranged in a square lattice with periodicity $d = 1.5\lambda_0 = 45$ mm in the superstrate configuration analyzed in the previous sections. The outer dimensions of the antenna are the same as the one in Fig. 3.7(a). The structure is shown in Fig. 3.14 (left). The array patterns for a beam pointing at broadside and at the edge of coverage ($\theta_E = 8.6°$) are shown in Fig. 3.15. Limited scan losses are observed in the considered region. When scanning toward the edge of coverage, a grating lobe appears at $\theta_{GL} = sin^{-1}(sin\theta_0 - \lambda_0/d) = -31.1°$, but its amplitude is below the side lobe level, by virtue of the synthesized pattern. In particular, the grating lobe levels are -15.8 dB and -12.7 dB for the E- and the H-planes, respectively.

As a benchmark solution, we took an array of 5×5 horn antennas without the superstrate and with the same periodicity $d = 45$ mm of the previous example. We refer to this configuration in the following as *bare case*. The side of the square apertures of each horn is $a = d = 45$ mm, in order to maximize the aperture efficiency. The tapering length of the horns has been chosen equal to 108 mm, maximizing the broadside gain for the given aperture [49]. The benchmark array is shown in Fig. 3.14 (right). Fig. 3.16 shows the array pattern in E- and H-planes. The antenna performance is degraded with respect to the superstrate configuration. In addition to the presence of scan losses on both planes, the grating lobe level is very high. Comparing the two solutions, the superstrate array provides a reduction of the grating lobes of 4.5 dB and 7.5 dB in E- and H-planes, with respect to the bare case. Even if not reported for brevity, similar performances have been obtained over the considered band of operation.

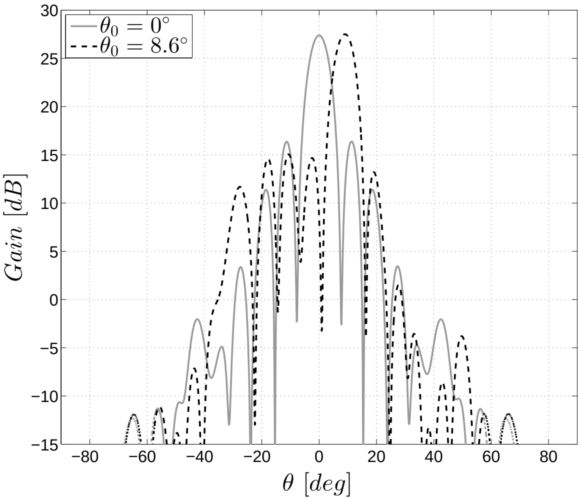

(a)

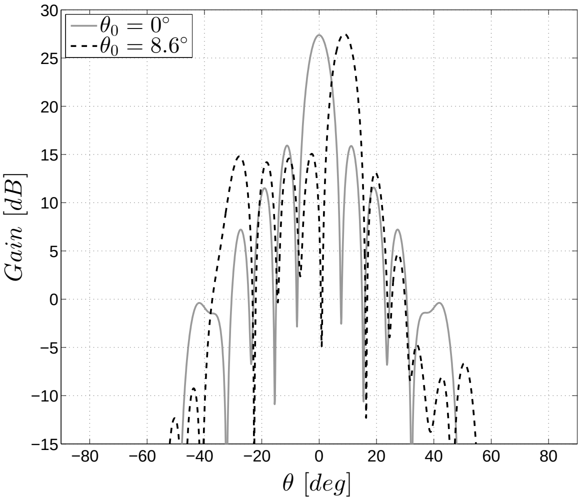

(b)

FIGURE 3.15: Simulated radiation patterns of the 5×5 LWAs array pointing at broadside ($\theta_0 = 0°$) or at $\theta_0 = 8.6°$. (a) E-plane. (b) H-plane.

3.1.3 Isoflux Radiation Pattern

We synthesize here an isoflux radiation pattern for medium Earth orbit (MEO) satellites using the procedure in Sec. 3.1.1. The isoflux pattern is exploited to compensate the path loss due to the curved surface of the ground, providing an homogeneous power density over the visible surface of the Earth. The isoflux pattern is a function of the geometrical parameters of the system. Approximating the shape of the Earth by a sphere with radius $R_e = 6,371$ km, the gain distribution of an antenna generating an isoflux

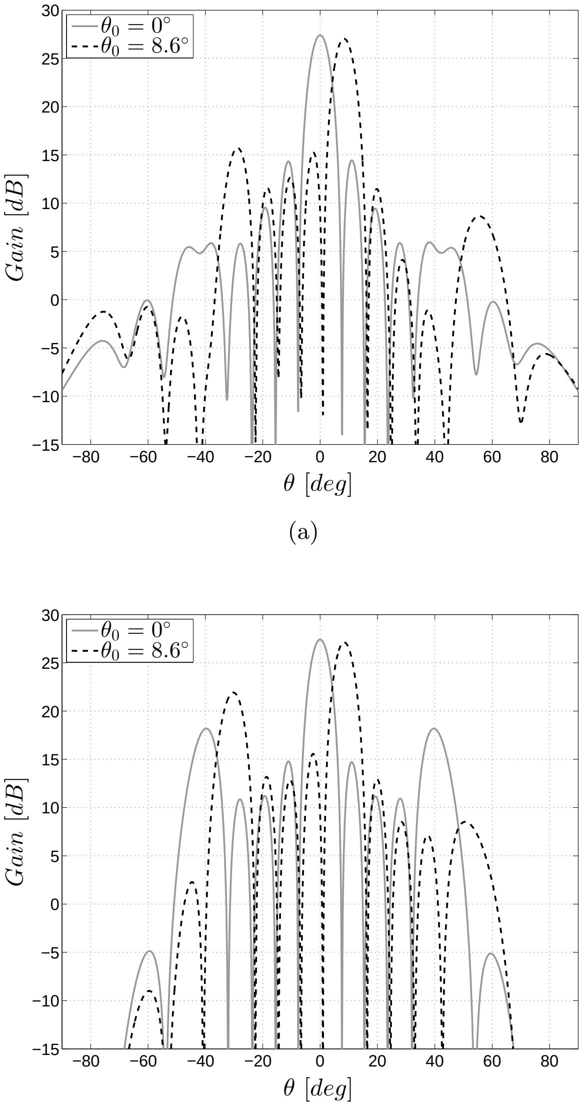

(a)

(b)

FIGURE 3.16: Simulated radiation patterns of the 5×5 array bare configuration pointing at broadside ($\theta_0 = 0°$) or at $\theta_0 = 8.6°$. (a) E-plane. (b) H-plane.

radiation pattern must be proportional to:

$$G(\theta, h) \propto \begin{cases} |cos\theta|\left(1+\frac{h}{R_e}\right) - \sqrt{1-\left(1+\frac{h}{R_e}\right)^2 sin^2\theta} & \text{, for } |\theta| \leq \theta_e \\ 0 & \text{, for } |\theta| > \theta_e \end{cases}, \tag{3.8}$$

with h the distance of the satellite from the ground and $\theta_e = sin^{-1}[R_e/(R_e + h)]$ the visibility angle, [62].

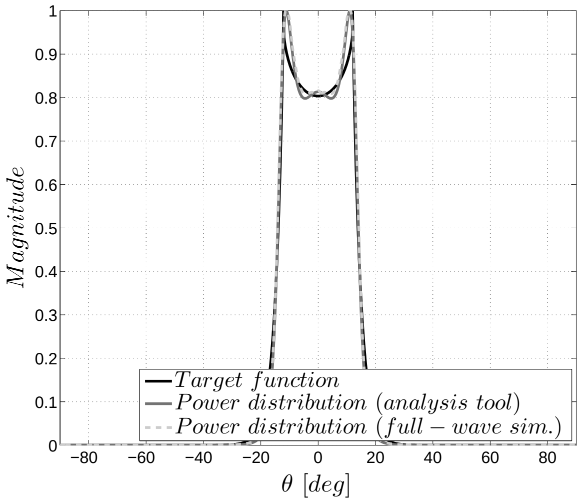

FIGURE 3.17: Isoflux radiation pattern in E-plane ($\phi = 90°$). The black curve represents the analytical function to be approximated. The normalized far-field radiation pattern of the optimized structure evaluated using the in-house analysis tool and full-wave simulations are shown in dashed gray line and solid gray curve, respectively.

As an example, we design an antenna for MEO applications circling at a height $h = 23,222$ km, like the GIOVE-A satellite of the Galileo satellite system. In this case, the visibility angle is equal to $\theta_e = 12.4°$. The following target function has been chosen to perform the optimization:

$$\mathbf{F}_i(\theta,\phi_0) = \begin{cases} |cos\theta|\left(1+\dfrac{h}{R_e}\right) - \sqrt{1-\left(1+\dfrac{h}{R_e}\right)^2 sin^2\theta} & \text{, for } \theta \le \theta_e \\ \dfrac{e^{-\theta\cdot c}}{e^{-\theta_e\cdot c}} & \text{, for } \theta > \theta_e \end{cases}, \tag{3.9}$$

where c is a constant. An exponentially decaying function has been introduced for $\theta > \theta_e$ to make the target function continue and manageable by the optimization tool.

Using a number of impedance sheets $N = 2$ and a design frequency equal to $f_0 = 10$ GHz, the optimization process generates a structure where the impedance values are $Z_{s1} = j\,22.5\ \Omega$, $Z_{s2} = j\,86.8\ \Omega$. Referring to Fig. 3.1, the spacings between each layer are $t_1 = 14.42$ mm and $t_2 = 13.92$ mm. The source is a square waveguide with side $a = 27$ mm.

In Fig. 3.17 the analytical and simulated radiation patterns are shown together with the target power distribution. The full-wave simulation has been performed using HFSS,

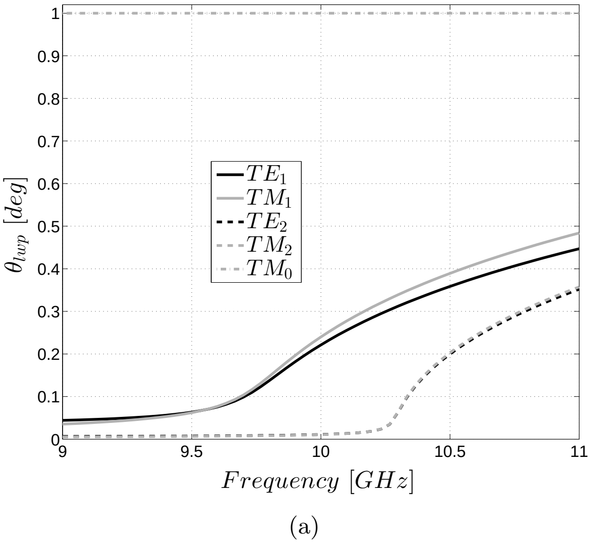

(a)

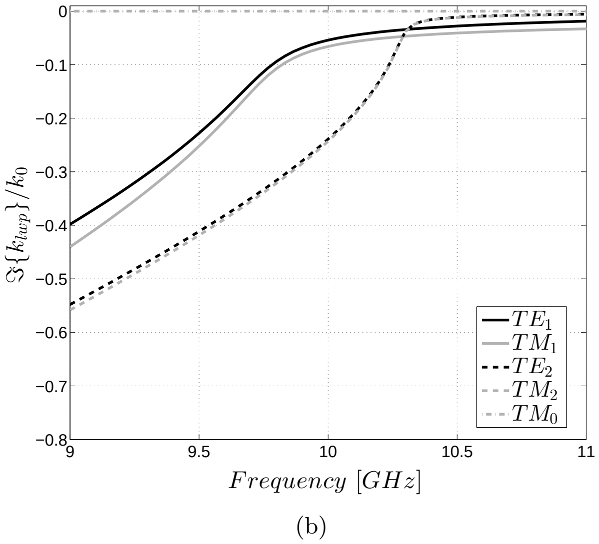

(b)

FIGURE 3.18: Dispersion diagrams for the LWA generating a flat-topped radiation pattern. (a) Real part of the propagation constant expressed in radiation angles. (b) Normalized attenuation constant.

considering the same simulation setup as for the flat-topped case. We remark a good agreement between the three curves.

In Fig. 3.18 the solution of the dispersion equation is displayed for the structure under analysis. The direction of the couple of the leaky wave poles TE_1/TM_1 is close to 13°. The second couple TE_2/TM_2 is in cut-off at 10 GHz, but it weakly contributes to the radiation. We still have a single TM_0 mode pointing endfire.

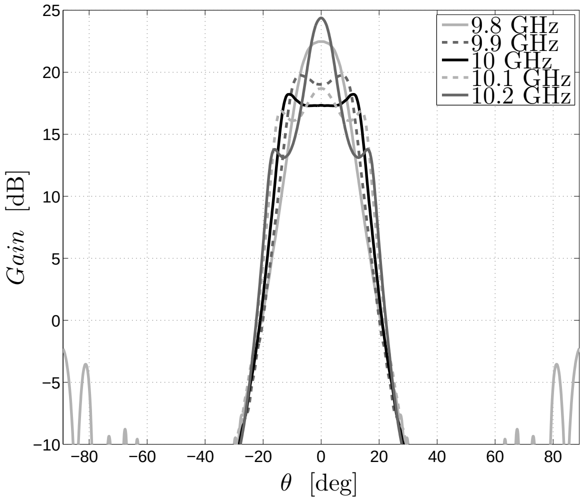

(a)

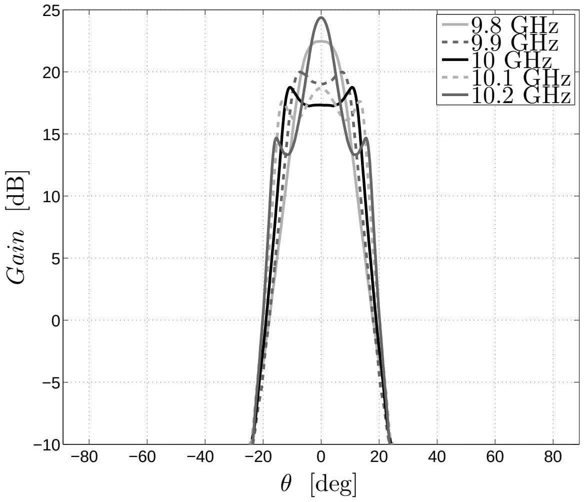

(b)

FIGURE 3.19: Simulated radiation pattern of the LWA generating the isoflux shape in a 4 % bandw.

Fig. 3.19 shows the frequency behavior of the designed structure. The antenna is dramatically frequency dependent. The radiation pattern exhibits important variations even in a narrow band.

3.2 Cosecant-Squared Radiation Pattern

In this section we focus our attention on the generation of cosecant-squared patterns, useful in applications where a uniform power illumination is required within a certain

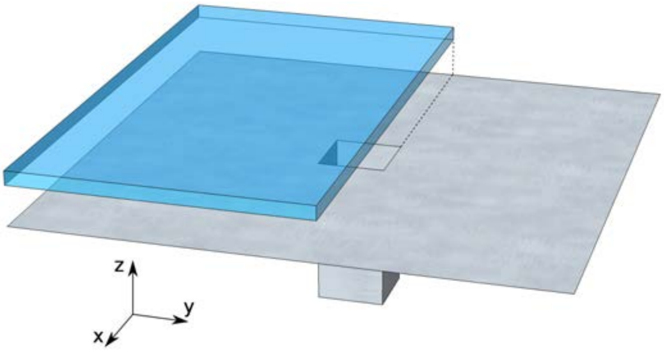

Figure 3.20: Leaky-wave antenna with truncated dielectric superstrate.

angular range [5]. In literature, cosecant-squared radiation patterns are typically obtained using curved shaped reflectors [63], phased array antennas [64], reflectarrays [65], shaped lenses [66] and also leaky-wave antennas [67]. Here, we present a simple design methodology to shape asymmetrically the radiation pattern of a low-cost superstrate-like configuration.

The basic idea consists in properly truncating the superstrate in such a way to shape asymmetrically the radiation pattern to achieve a cosecant-squared pattern or other functions required by the particular application.

3.2.1 Antenna Design

The proposed antenna architecture is represented in Fig. 3.20. The design frequency has been chosen equal to $f_0 = 10$ GHz. The source is an open waveguide on the ground plane with a lateral side $a = 21$ mm and with the electric field polarized along the y axis. The superstrate is made by a dielectric slab with relative permittivity $\epsilon_r = 10$. However other solutions can be envisaged as FSSs, metasurfaces, etc. The superstrate is placed at a height 0.55 λ_0 (free-space wavelength $\lambda_0 = 30$ mm at the operating frequency) over the ground plane and its thickness is $\lambda_d/4$, where λ_d is the wavelength in the dielectric. This superstrate configuration has been chosen in such a way to generate a couple of leaky-wave modes pointing at 23° as shown in the dispersion diagram in Fig. 3.21. The dielectric slab is then truncated in the E-plane (yz-plane), in order to generate an asymmetric radiation pattern. The truncation is performed in such a way to suppress the Transverse Magnetic (TM) leaky-wave mode traveling along the positive y direction

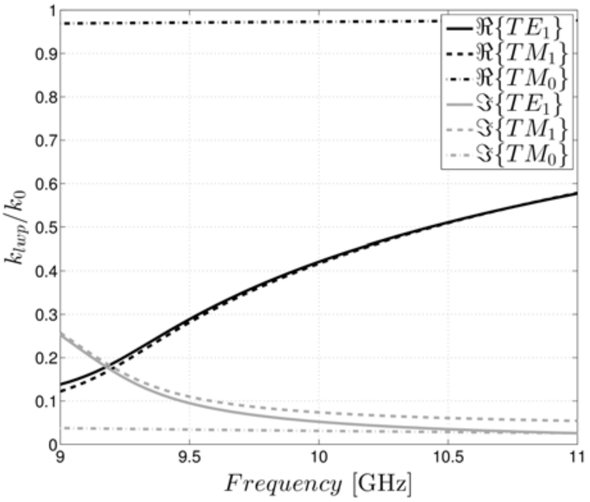

FIGURE 3.21: Dispersion diagram of the structure without truncation.

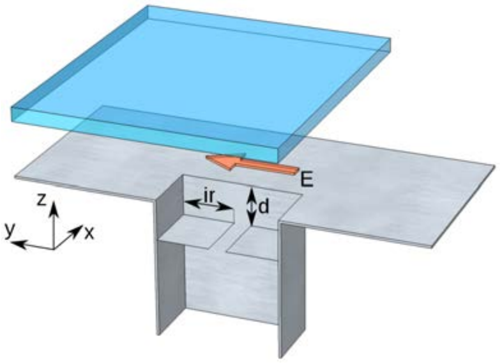

FIGURE 3.22: Section of the structure in Fig. 5.1 exposing the matching iris. The green arrow represents the direction of the electric field.

without affecting the one traveling on the opposite side. At the same time the pattern is shaped to fulfill the required radiation pattern.

A metallic capacitive iris has been introduced inside the waveguide for matching purposes. The structure is shown in Fig. 3.22. The distance of the iris from the aperture plane is $d = 5.54$ mm, while the dimension of the flap is $ir = 5.4$ mm. The reflection coefficient is reported in Fig. 3.23 as a function of the frequency. As we can see, the S_{11} is lower than -10 dB in a 12 % band centered at 10 GHz. This bandwidth is acceptable for many applications. If needed, it could be extended or achieved return loss improved by implementing a more complex matching network (e.g. multiple irises).

The radiation pattern of the antenna has been simulated using ANSYS HFSS and the

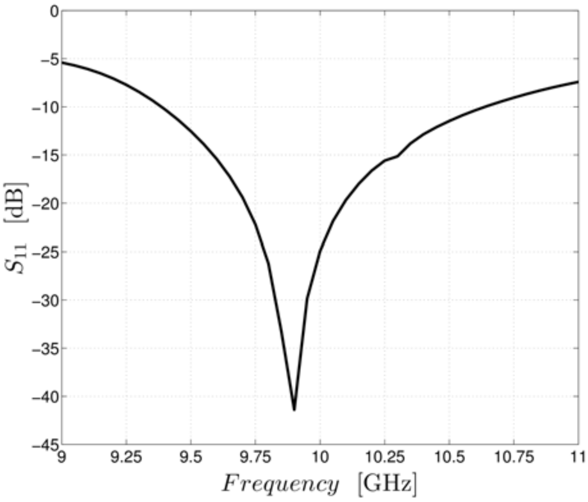

Figure 3.23: Reflection coefficient of the designed structure.

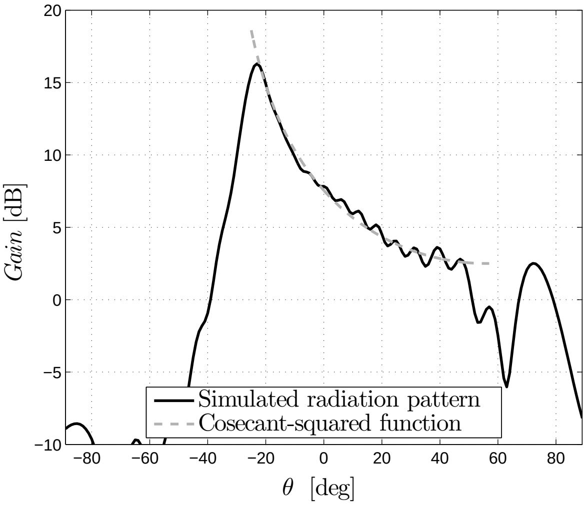

Figure 3.24: Simulated radiation pattern in E-plane (y,z plane). A the cosecant-squared function is shown for comparison.

resulting radiation pattern on the E-plane is shown in Fig. 3.24. The ideal cosecant-squared function is shown for comparison. A good agreement is achieved between the ideal function and the actual radiation pattern in an angular range of approximately 71° (for θ within $-23°$ and $48°$).

The 3-D radiation pattern in Fig. 3.25 gives us a clearer understanding of the capabilities of the antenna. The beam is broad along the x-axis. This characteristic is typically appreciated in this kind of antennas. It is worth noting that a linear array of sources could be placed on the x-axis in order to scan the beam, increase the gain and/or shape

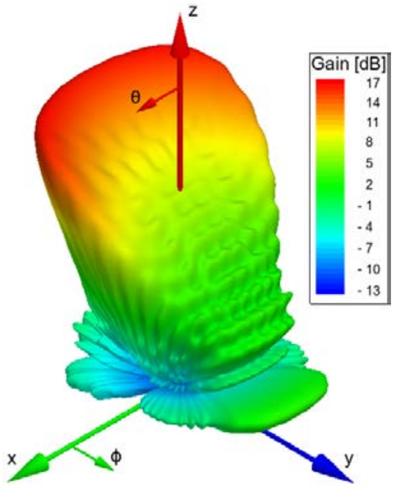

FIGURE 3.25: 3-D radiation pattern.

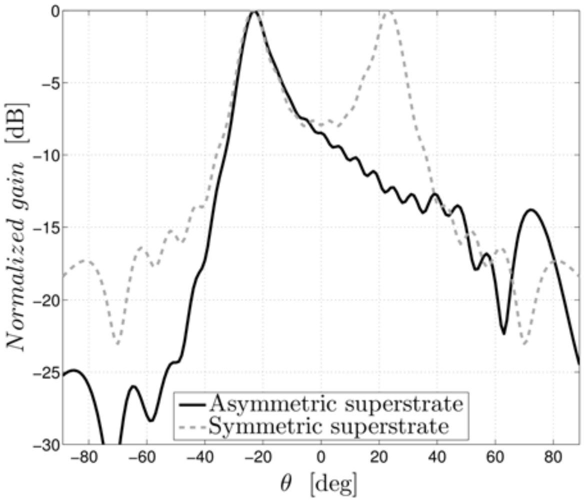

FIGURE 3.26: Radiation pattern of truncated and non-truncated superstrate antennas.

the pattern in the H-plane without perturbing the cosecant-squared shape in the other plane.

A comparison between truncated and non-truncated superstrate structures is reported in Fig. 3.26. The radiation patterns of the two antennas are similar for angles close to the pointing direction of the leaky-wave modes. This comparison confirms how such a truncation allows the correct excitation of the leaky-mode in a single direction.

The frequency behavior of the antenna can be described using the dispersion diagram in Fig. 3.21. In particular, the position of the maximum directivity in the radiation

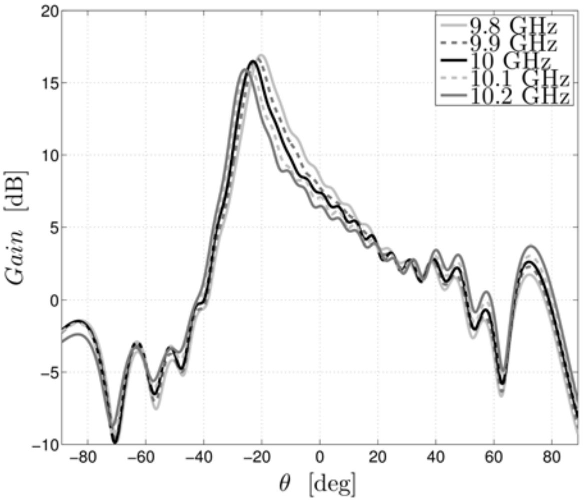

FIGURE 3.27: Simulated radiation pattern in a 4 % bandwidth.

pattern corresponds to the the pointing angle of the leaky-wave mode.

The antenna bandwidth is here defined as the frequency band for which a variation of 1 dB is observed in the radiation pattern. In this particular case, the gain varies of 1 dB over a 4 % bandwidth. The pointing direction varies of about 5.5° within this band. The cosecant-squared shape and the roll-off are preserved in the whole band.

To have a better understanding of the frequency behavior of the antenna, we report in Fig. 3.28 the maximum gain and its position in a 20 % band. Again, the leaky-wave changes its pointing angle θ_{Max} varying the frequency. Nevertheless, it is remarkable for such a directive structure how the 3 dB gain variation bandwidth is larger than 17 %.

3.2.2 Analysis and Recommendations

An analytic procedure has been developed to study the radiating characteristics of such a truncated structure. It is based on the spectral approach described in Chapter 2. The aim is to predict the radiation pattern of the structure without the use of numerical simulators.

The first step of the procedure consists in the evaluation of the near-field in the spectral domain of the antenna with the full-covering superstrate:

$$\mathbf{E}_s^{sup}(k_x, k_y) \propto \underline{\underline{\mathbf{G}}}^{em}(k_x, k_y) \cdot \mathbf{M}(k_x, k_y). \tag{3.10}$$

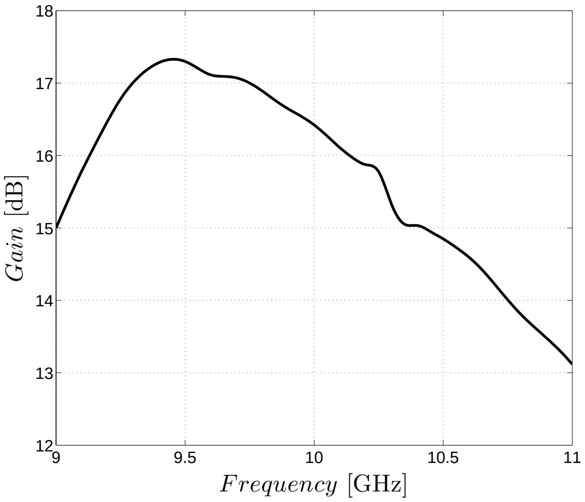

(a)

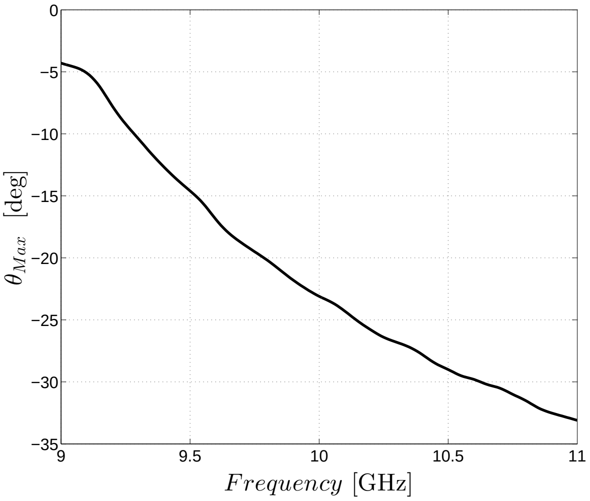

(b)

FIGURE 3.28: Maximum gain (a) and its position θ_{Max} (b) as a function of the frequency.

$\underline{\underline{\mathbf{G}}}^{em}(k_x, k_y)$ the spectral dyadic Green's function of the structure evaluated at the height of the superstrate. $\mathbf{M}(k_x, k_y)$ is the Fourier transform of the equivalent magnetic current representing the feeding aperture (Sec. 2.1.1.3). The near-field for the antenna in Sec. 3.2.1 with a full-covering superstrate is shown in the spectral domain in Fig. 3.29 (a).

With an inverse Fourier transform we move from the frequency to the space domain:

$$\mathbf{E}_s^{sup}(x, y) = IFT\,[\mathbf{E}_s(k_x, k_y)]. \tag{3.11}$$

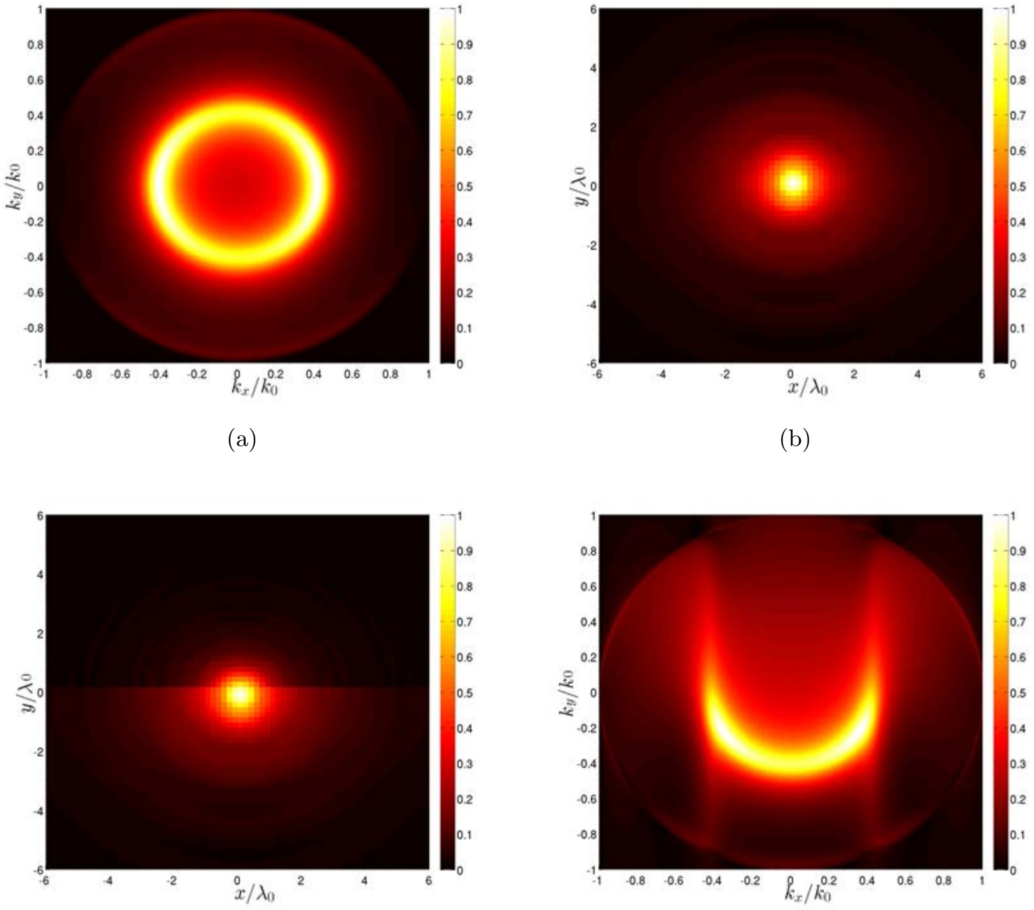

(a) (b)

(c) (d)

Figure 3.29: Analytic procedure to predict the radiating properties of the truncated superstrate structure: near field in the spectral domain with a fully-covering superstrate (a), near field in the space domain (b), substitution of the field on the truncated region with the field of the bare configuration (c), near field in the spectral domain after the substitution (d).

We obtain the field distribution in Fig. 3.29 (b).

In the space domain, we substitute the field on the truncated region with the field of the bare configuration:

$$\mathbf{E}_s(x,y) = \begin{cases} \mathbf{E}_s^{sup}(x,y) & \text{for} \quad -\infty < y \leq y_{trunc} \\ \mathbf{E}_s^{bare}(x,y) & \text{for} \quad y_{trunc} < y < +\infty \end{cases} \tag{3.12}$$

The result is shown in Fig. 3.29 (c).

Eventually, we move back to the frequency domain though a Fourier transform. The

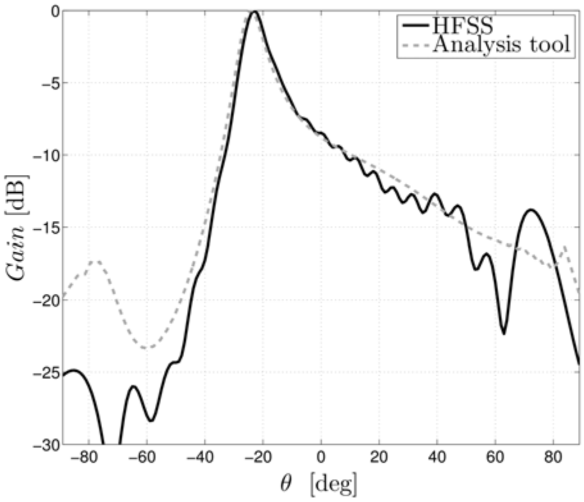

FIGURE 3.30: Analytic procedure for truncated superstrate structures: comparison between HFSS simulation and analytic approach.

new field distribution is reported in Fig. 3.29 (d). An asymptotic approximation can be now used to evaluate the radiated field. The result is shown in Fig. 3.30. We remark a good agreement between the proposed method and HFSS simulations.

Note that this approach does not take into account the edge effects of the truncation.

3.3 Summary

In this chapter we presented novel ways and methodologies to efficiently shape the radiation pattern of planar leaky-wave antennas.

In the first part we presented a universal analytic synthesis tool to obtain a desired radiation pattern giving as input a mathematical function. Different kind of shapes can be obtained using this tools. In particular, we analyzed two structures radiating a flat-topped radiation pattern and an isoflux radiation pattern, respectively. The structure radiating a flat-topped shape has been manufactured and tested. A good agreement is shown between the simulation results and the measurements.

In the second section of the chapter we analyzed the possibility to produce a cosecant-squared radiation pattern conveniently truncating the superstrate and generating an asymmetric radiation pattern. The truncation suppresses the transverse magnetic leaky-wave mode traveling along the positive y direction without affecting the one traveling on the opposite side. An analysis method has been also proposed, showing a good agreement with the simulation results.

Chapter 4

Leaky-Wave Antenna Arrays

One of the most interesting aspects of leaky-wave antennas is the possibility to increase the effective aperture of small sources through a superstrate and consequently enhance the gain [23, 25–27, 33]. In doing so, an electrically large antenna can be substituted with a smaller one, with advantages in terms of weight and size.

These advantages are particularly evident when using the superstrate in array configurations [29, 30, 39, 40]. Here, the enhanced gain at element level can be exploited to reduce the number of array elements, keeping the same overall maximum gain. In the complex scenario of space applications, even minor reductions of elements translate into significant improvements in terms of simplification and cost-effectiveness of the system.

In this chapter we want to investigate the possibility to improve the performance of classic aperture arrays for space applications using planar LWA arrays. In particular, the studies presented in the following are centered on the gain enhancement, that can, then, lead to a reduction of the number of array elements. In the first section we study the effects of the leaky-wave structures in the array environment, performing parametric studies on superstrates and array lattices. The results are used to design LWA arrays for space and user segment, analyzing their performance. The two segments have different specifications in terms of array lattice, element directivity and bandwidth. The trade-off between gain and bandwidth is considered. In the second section we introduce a novel configuration, the patch-superstrate antenna, where we make use of a truncated superstrate for the band enlargement. This antenna is, then, used to design a dual-band array in K- and Ka-bands for on-board satellite applications. The performance of the proposed array is compared with the ones of dual-band aperture arrays.

4.1 Planar Leaky-Wave Antenna Arrays Performance

The superstrate configuration is used here to increase the effective area of small aperture antennas and, consequently, aperture efficiency and gain. The goal is to find array configurations more directive than the existing classical solutions, so that the number of array elements can be reduced, guaranteeing the same link budget. However, in this chapter we will not quantify the reduction of number of elements. In fact, simple thinning procedures would lead to incomparable results: an array with reduced size has a different beamwidth, while a rearrangement of the elements shifts the position of the grating lobes. A synthesis procedure is needed to achieve a significant reduction of array elements and will be presented in Chapter 5.

In order to understand the effects of the superstrate on the broadside directivity, we present in this section a parametric study in the array configuration, varying the reflectivity of the PRS (partially reflective surface) and the distance between the elements of the array, monitoring the effects on mutual coupling and frequency behavior of the antenna. Following the conclusions of the parametric study, we analyze the leaky-wave technology applied to space and user segments.

All the radiation patterns shown in this section are evaluated using the in-house analysis tool presented in Chapter 2. The structures (superstrates and ground planes) are considered infinite in the transverse direction.

4.1.1 Parametric Study in Array Configuration

We present here the results of a parametric study addressed to understand the electromagnetic behavior of the LWA array varying the characteristics of superstrate and array lattice. In particular, we study arrays of apertures on a square lattice underneath a superstrate made of a single quarter-wave long dielectric slab. The conclusions hold using different kind of superstrates, such as impedance sheets [43], and number of slabs [29]. The parametric study is performed on the permittivity of the dielectric and the

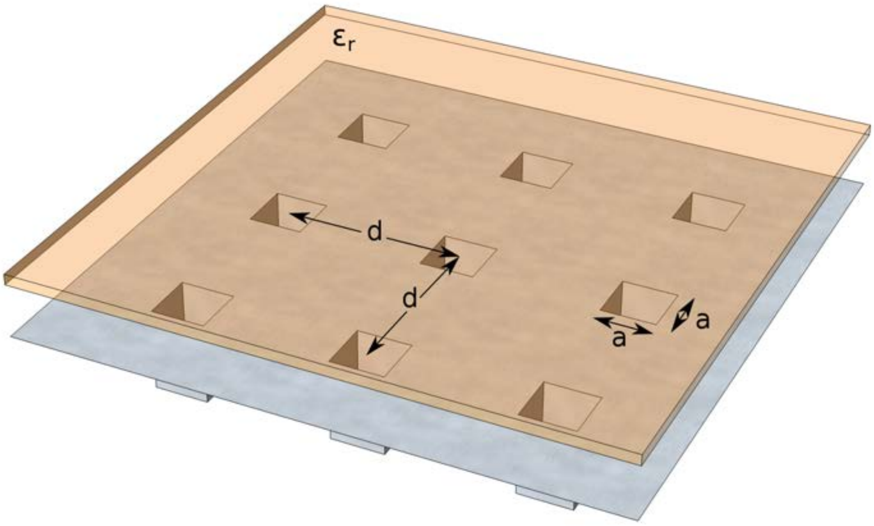

FIGURE 4.1: Setup of the parametric study: array of 3×3 square apertures in a square lattice with periodicity d, underneath a dielectric slab with relative permittivity ϵ_r.

distance between the elements. The array elements are square waveguide apertures on the ground plane. The side of the waveguide is not a parameter of the study because, as discussed in Section 2.4.2, it is generally useful to use small/low directive radiators. The following results have been evaluated using the analysis tool presented in Chapter 2.

The structure under analysis is shown in Fig. 4.1. It consists of an array of 3×3 square apertures with side $a = 0.7\,\lambda_0$ in a square lattice. The interelement distance d and the relative permittivity of the dielectric ϵ_r are parameters of the study. The dielectric slab is placed at height of $\lambda_0/2$ above the ground plane. Its thickness is $\lambda_d/4$ at the design frequency, where $\lambda_d = \lambda_0/\sqrt{\epsilon_r}$ is the wavelength in the dielectric.

The results of the parametric study are reported in Fig. 4.2. Here we show the gain (a) and the mutual coupling (b) with varying interelement distance and permittivity of the dielectric slab. Note, that we reported in Fig. 4.2 (b) the strongest level of mutual coupling, between neighbor elements of the array.

For small interelement distances, the broadside gain is reduced by the high level of mutual coupling. Separating the elements, the gain increases up to a point where it gets steady. In this point, the mutual coupling is below -30 dB. A denser dielectric increases both the gain and the coupling between the sources. Therefore, the interelement distance needed to maximize the gain increases. Using a dielectric with relative permittivity $\epsilon_r = 4$ allows the maximization of the gain for distances of about $1.5\,\lambda$. For a dielectric

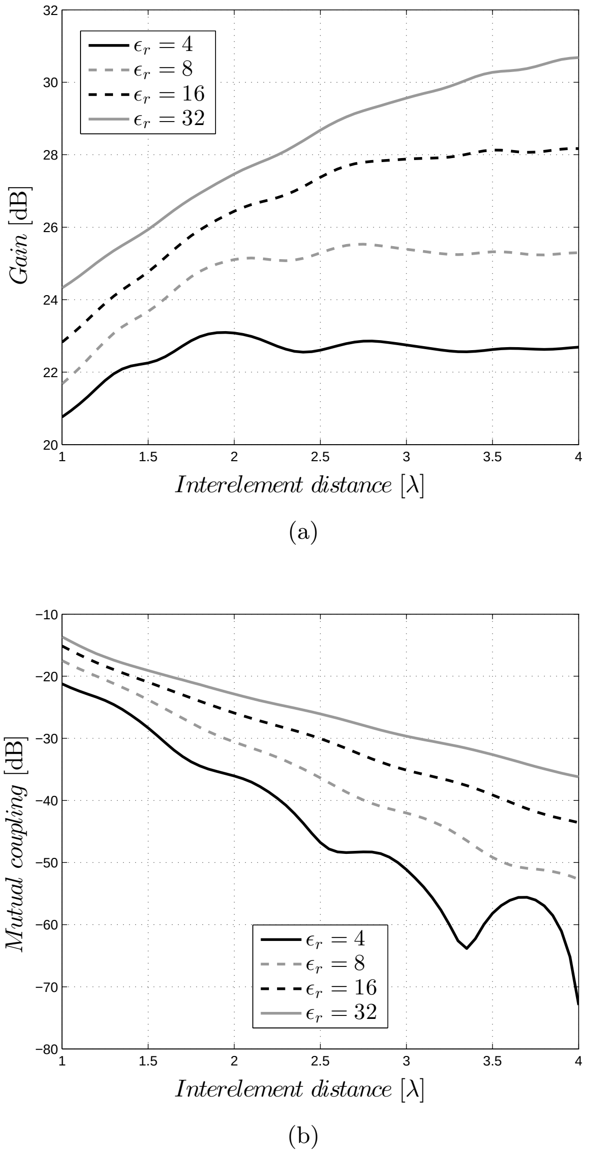

FIGURE 4.2: Gain (a) and mutual coupling (b) varying the interelement distance and the permittivity of the dielectric superstrate.

with permittivity $\epsilon_r = 32$, this distance increases to about $4\,\lambda$. On the other hand, also considering an interelement distance equal to $1.5\,\lambda$, the denser dielectric produces a gain almost 4 dB higher than the low-permittivity solution.

To have a wider view of the performance of this antenna we have to investigate its frequency behavior. The study is reported in Fig. 4.3. Here the broadside gain is plotted as a function of the frequency for the different permittivities of the dielectric slab. Three interelement distances are plotted: $1\,\lambda$ (a), $2\,\lambda$ (b), $4\,\lambda$ (c).

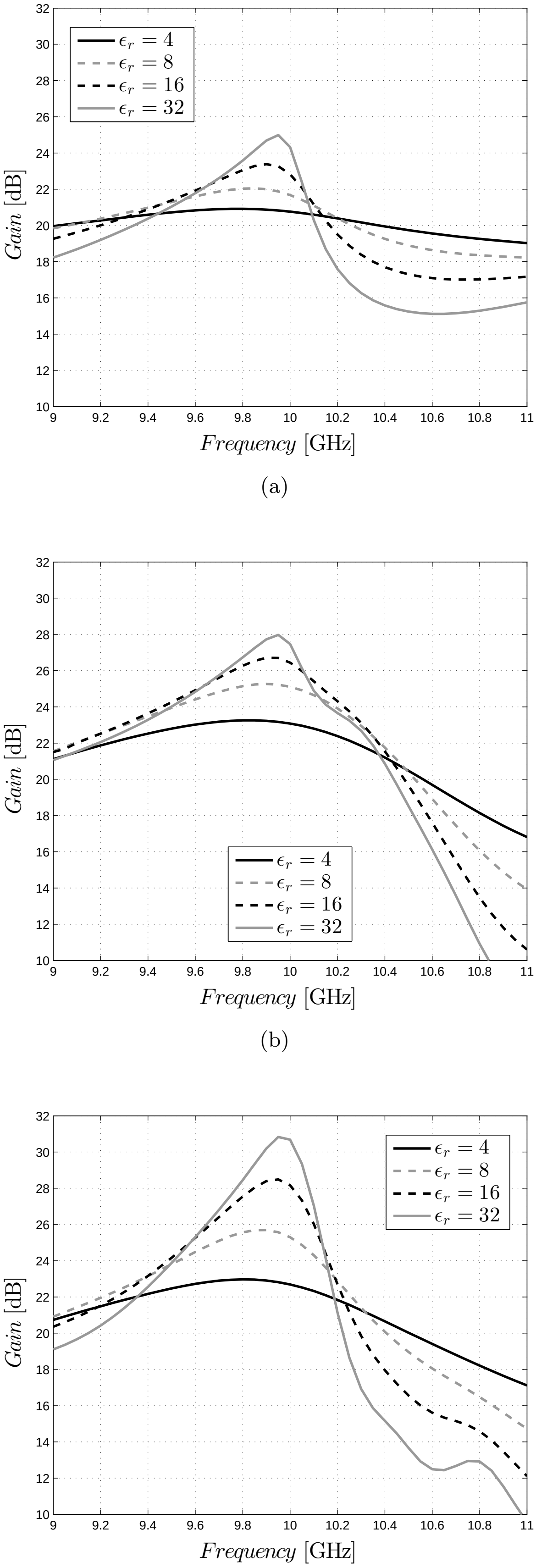

(a)

(b)

(c)

FIGURE 4.3: Broadside gain as a function of the frequency for three interelement distances: $1\,\lambda$ (a), $2\,\lambda$ (b), $4\,\lambda$ (c).

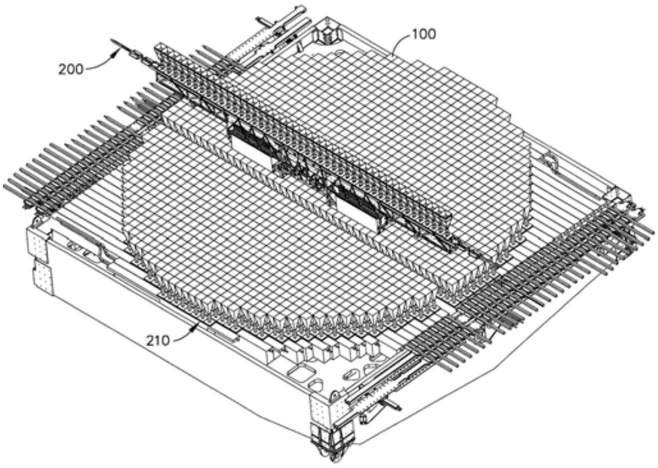

Figure 4.4: Phased array for the space segment [68].

The gain of the array with the low-permittivity dielectric increases of about 2 dB increasing the distance from 1 to 2 λ, while there is almost no difference comparing 2 λ with 4 λ. The gain of the high-permittivity configuration, instead, keeps increasing while spacing the elements up to 4 λ.

The dispersive behavior of the structure appears enhanced using a more reflective superstrate. It is worth noting how the gain variation is just moderately affected by the interelement distance, while the strongest contribution is given by the choice of the permittivity of the dielectric.

This parametric study shows how it is necessary to increase the distance between the elements to fully exploit a highly reflective superstrate. Once the array lattice is set, the permittivity of the superstrate rules the directivity and the gain variation over the frequency.

4.1.2 Space Segment

Using the information acquired through the parametric study, we can now efficiently design the arrays for space and user segments. The space segment is the most challenging one, as it requires high gain and wide bandwidths. Typical phased arrays for geosynchronous satellites can be made of $1,000 \sim 1,500$ elements in a square lattice with periodicities of $3 \sim 4$ λ, percentage bandwidth of $8-14\,\%$ and gain higher than 40 dB, as for the case in [68] (Fig. 4.4). These highly directive phased arrays are typically used for

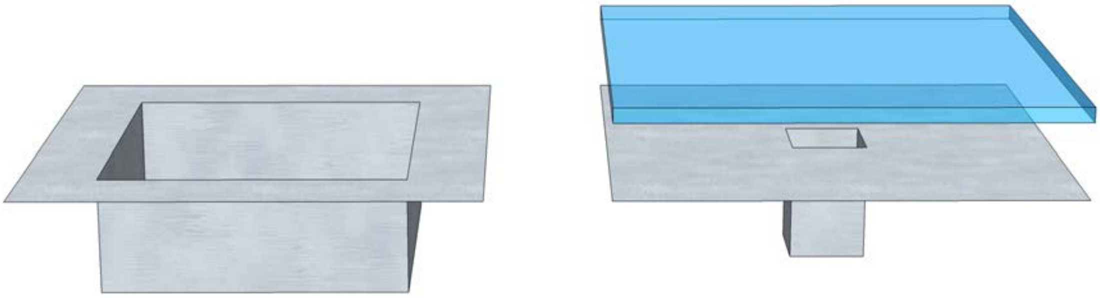

FIGURE 4.5: $4\,\lambda_0 \times 4\,\lambda_0$ bare aperture (on the left) and LWA (on the right).

multiple beam applications, providing user links over a regional or continental coverage. The size of a continent like Europe seen from a geostationary orbit corresponds to a $3^\circ \sim 4^\circ$ angular region. The antenna is designed to produce multiple fixed or steerable beams with a beamwidth of about 0.5 degrees or less within the angular range defined above.

We analyze, here, the possibility to replace standard aperture solutions with LWA arrays in the space segment and, potentially, to reduce the number of elements maintaining the link budget.

A benchmark solution has been chosen to understand if the superstrate structure can be used for the reduction of the number of elements. It consists of an arrangement of 18×18 square apertures on a square lattice with periodicity $4\ \lambda_0$. It is worth noting that the conclusions in the following hold also changing the number of elements. The side of each waveguide (Fig. 4.5, left) is $4\ \lambda_0$. The apertures are excited with a single TE_{10} mode.

A LWA array has been designed to have approximately the same gain at the design frequency. As we have shown in Secion 4.1.1, the gain of a LWA array element is modified by the presence of the neighboring elements. Therefore, the design of the superstrate must be done in the array environment. Such a LWA array can be designed using a square waveguide aperture with side $a = \lambda_0$ (excited with a single TE_{10} mode) below a quarter-wave dielectric slab with permittivity $\epsilon_r = 38$ (Fig. 4.5, right). The superstrate forms an half-wavelength cavity with the ground plane.

As clear from the parametric study in Secion 4.1.1, this antenna is extremely narrow band. We are going to analyze now the radiation properties both at element and array levels.

4.1.2.1 Single Element Performance

Before analyzing the array performance, it is interesting to compare the performance of the radiating elements of the designed arrays. In Fig. 4.6 we compare the radiation pattern of a single bare aperture (with a side of 4 λ_0) with the isolated LWA aperture (with a side of 1 λ_0 underneath the superstrate). In particular, the comparison is performed over a 8 % band, suitable for space applications.

At the central frequency, Fig. 4.6 (c) and (d), we notice how the superstrate structure suppresses the side lobes in the radiation pattern and makes symmetric the HPBW (half-power beamwidth) on the two main planes. It is worth noting that the asymmetric HPBW of the reference solution depends on the choice of the single-mode horn and alternatives (dual-mode) horns would provide more symmetric patterns, as discussed in Chapter 1.

The drawback of this particular highly directive leaky-wave structure rises up when we look at the frequency behavior. In the lower part of the band (Fig. 4.6 (b)), the leaky-modes are in cut-off and the gain drops of almost 10 dB. At higher frequencies (Fig. 4.6 (f)), the main couple of leaky-modes are not pointing broadside, where a local minimum occurs. The gain of the benchmark solution, instead, remains stable in the considered band, as we can see in Fig. 4.6 (a) and (e).

4.1.2.2 Array Performance

We analyze here the performance in the array configuration (18 × 18 elements). As reported in Fig. 4.7 (d), at the central frequency the LWA array proves to be a solid alternative to the benchmark solution (Fig. 4.7 (c)). In fact, the gain is comparable and the first grating lobes is reduced of about 3 dB on the H-plane. The superstrate structure provides a rejection of the grating lobes thanks to the higher roll-off figure at element level with respect to the bare aperture. No grating lobes appear in the E-plane of the benchmark solution, because their positions is the same as the zeros of the element pattern. This property, however is not preserved while scanning.

The issues of the LWA array appear, also in this case, when we look at the frequency behavior. In the same way as for the isolated element, the LWA array has a strong

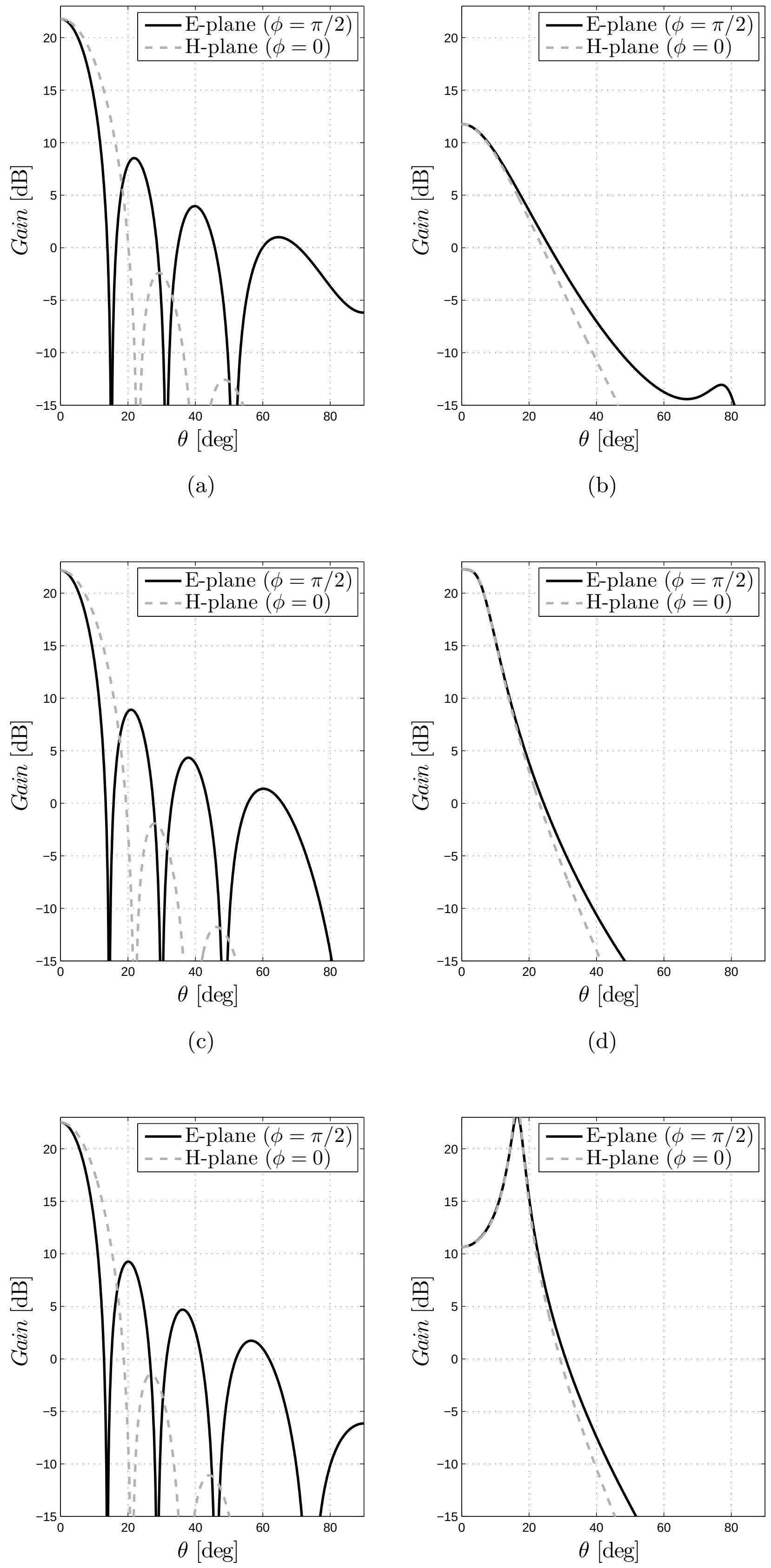

(a) (b)

(c) (d)

(e) (f)

FIGURE 4.6: Radiation pattern of the isolated element of the array designed for the space segment in a 8 % band: bare aperture at $0.96\,f_0$ (a), LWA at $0.96\,f_0$ (b), bare aperture at f_0 (c), LWA at f_0 (d), bare aperture at $1.04\,f_0$ (e), LWA at $1.04\,f_0$ (f).

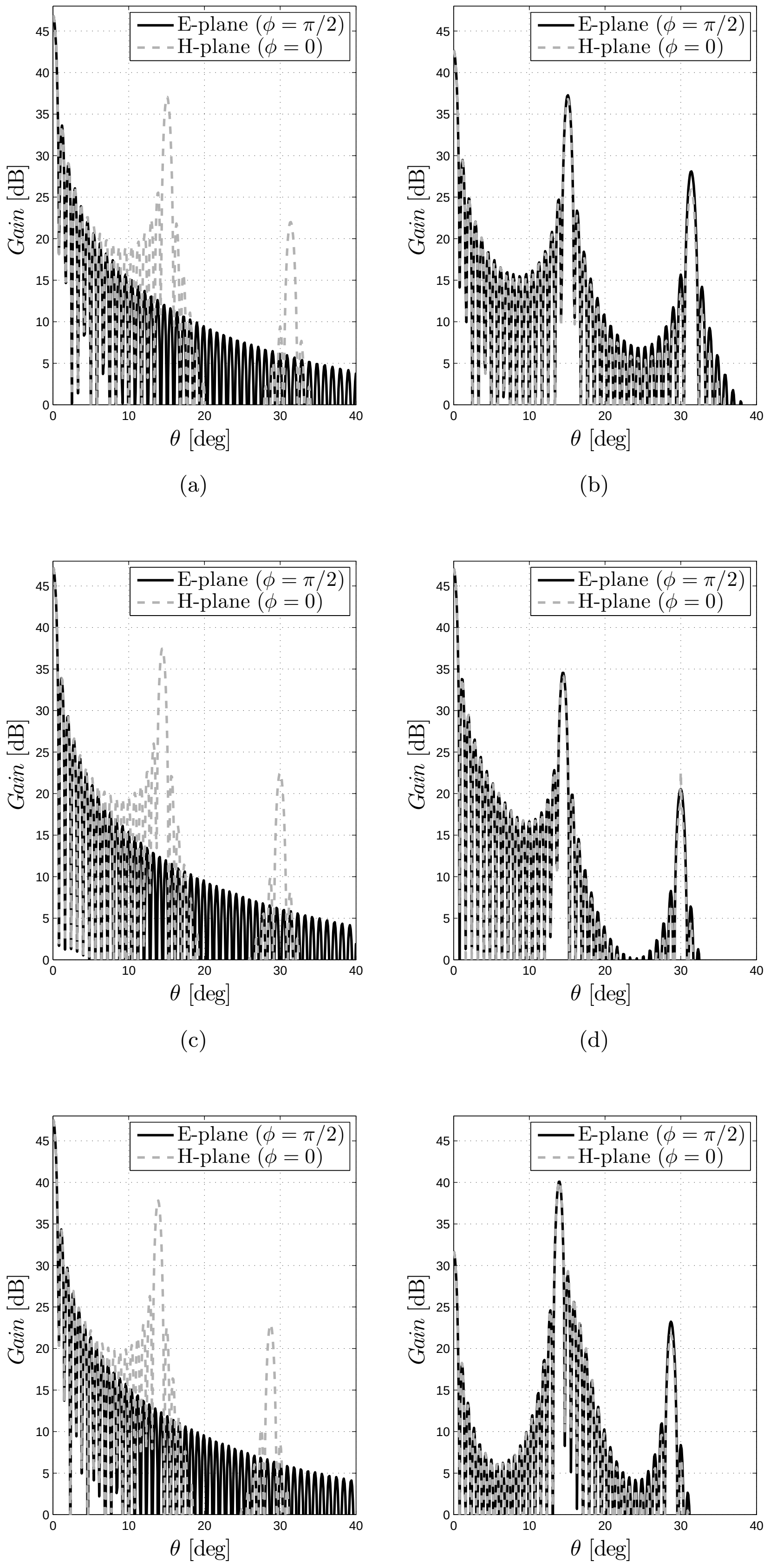

(a) (b)

(c) (d)

(e) (f)

FIGURE 4.7: Radiation pattern of the 18×18 elements array for the space segment in a 8 % band: bare apertures at $0.96\, f_0$ (a), LWA array at $0.96\, f_0$ (b), bare apertures at f_0 (c), LWA array at f_0 (d), bare apertures at $1.04\, f_0$ (e), LWA array at $1.04\, f_0$ (f).

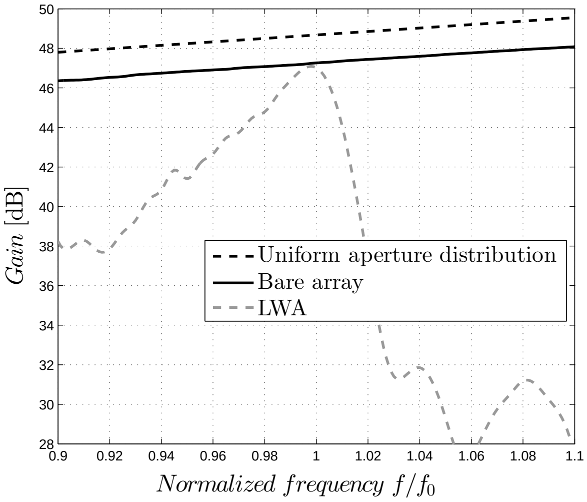

FIGURE 4.8: Arrays with 4 λ_0 periodicity and single aperture: broadside gain versus frequency.

gain variation with the frequency (Fig. 4.7 (b) and (f)). Moreover, the level of the first grating lobe is higher than the one of the benchmark solution (Fig. 4.7 (a) and (e)).

To have a clearer view of the frequency performance of the array, we report in Fig. 4.8 the broadside gain as a function of the frequency. The gain of a single aperture with the dimension of the array fed by a uniform field distribution is also reported for comparison. The broadside gain of the bare array is stable in the whole band. The leaky-wave array has a strong gain variation, 3 dB in a 3.5 % bandwidth.

We report, for completeness, the scanning performance of the two arrays. The scanning capabilities of phased arrays must be exploited when using them on GEO satellite systems. Indeed, phased arrays are typically used in multiple beam applications, where we are interested in scanning the beam over small angles, such as a continent like Europe, corresponding to a $3^\circ \sim 4^\circ$ angular region. We analyze here the performance of the designed arrays while scanning this angle.

Fig. 4.9 (a) shows the performance of the bare array at the design frequency scanning at 4° on the E-plane. For such a small angle, the scan losses are low. Nevertheless, the grating lobes appear in the visible space, as their position is no more on the zeros of the element pattern. The superstrate array enhances the radiation properties while scanning, if compared with the bare configuration. The radiation pattern is reported in Fig. 4.9 (b). The scan losses are 0.7 dB lower and the first grating lobe is reduced by

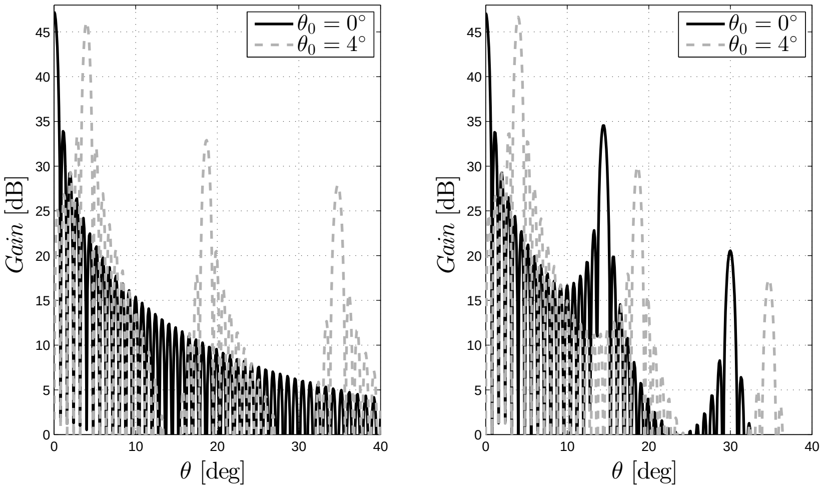

(a) (b)

FIGURE 4.9: Radiation pattern of the 18 × 18 elements array for the space segment at the design frequency scanning at 4°: bare apertures (a), LWA array (b).

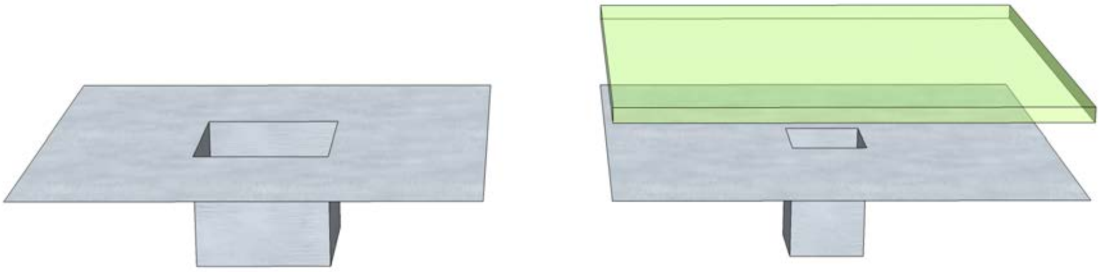

FIGURE 4.10: $1.8\,\lambda_0 \times 1.8\,\lambda_0$ bare aperture (on the left) and LWA (on the right).

3.5 dB in the superstrate array case. However, these properties get lost once we consider a frequency band of 8 %.

To conclude, the LWA can not be efficiently used in the space segment for the gain enhancement without releasing some of the constraints. Its most relevant drawback is the dispersive behavior of the structure, if we want to obtain extremely high gain levels, as in this case. However, some interesting properties in the pattern shaping of the LWA arrays can be exploited, as shown in this manuscript.

4.1.3 User Segment

If the LWA arrays are not the best solution to fulfill the requirements in gain and bandwidth on the space segment, they represent a solid alternative to the horn antennas in the ground segment. In fact, the ground antenna arrays use periodicities smaller than the ones for on-board satellite antennas and the bandwidth requirements are much less demanding. Typical percentage bandwidth are $1 \sim 3\,\%$. In the following, we compare a LWA with a benchmark bare array to understand the capabilities of the system for this application.

In this study we consider as benchmark solution an array of 18×18 square apertures on a ground plane, disposed on square grid with interelement distance 1.8 λ_0. The conclusions hold changing the number of array elements. Also in this case, the size of the side of each aperture (Fig. 4.10, left) is equal to the periodicity of the array (1.8 λ_0). All the array elements are excited with the TE_{10} mode.

A LWA array has been designed to produce a broadside gain comparable to the benchmark solution, while using the same number of elements and periodicity. Again, a square waveguide with the side $a = \lambda_0$ has been used. This time, a less reflective superstrate can be used, as the benchmark aperture is less directive than for the space segment. In particular, a quarter-wave dielectric slab with permittivity $\epsilon_r = 10$ has been selected to form the resonant cavity with the ground plane. The choice of the dielectric superstrate has been done in array configuration because the mutual coupling alters the value of the broadside gain, as seen in Secion 4.1.1.

Such a LWA is not extremely narrow band, as we can see from the parametric study in Secion 4.1.1.

4.1.3.1 Single Element Performance

We show here the radiation properties of the array elements in their isolated configuration. In Fig. 4.11 we report a comparison between the radiation pattern of the bare aperture (side of 1.8 λ_0) and the LWA (side of 1 λ_0 underneath the superstrate). The comparison is performed over a $3\,\%$ band, sufficient for user segment.

The superstrate structure provides an higher gain at the central frequency (Fig. 4.11 (d)), if compared with the bare aperture (Fig. 4.11 (c)). Also, the side lobes are reduced.

Conversely to the space segment case, here the variation of the radiation pattern in the considered bandwidth is moderately low (Fig. 4.11 (b) and (f)), and presents similar gain and lower SLL compared with the benchmark solution (Fig. 4.11 (a) and (e)).

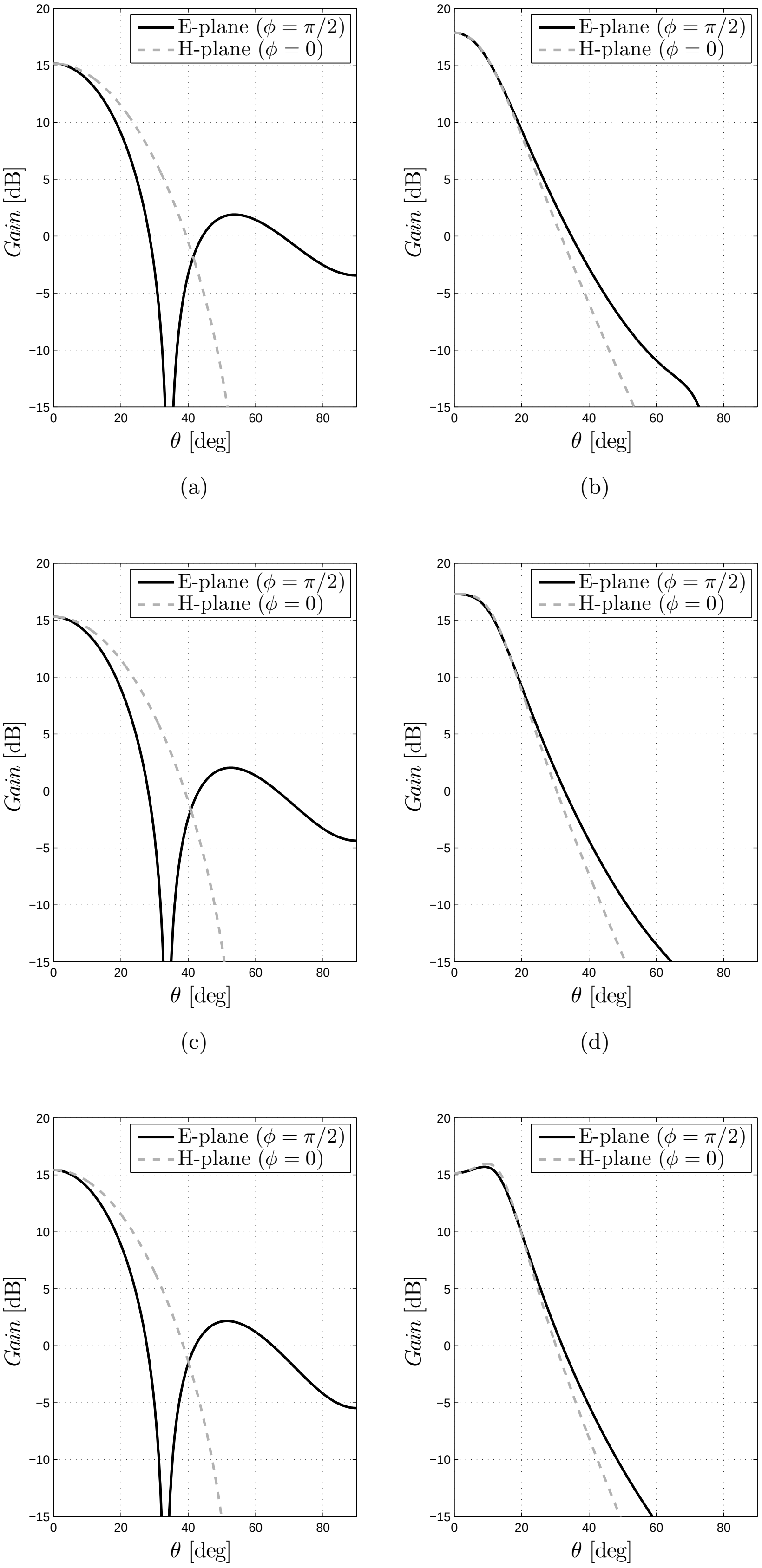

(a) (b)

(c) (d)

(e) (f)

Figure 4.11: Radiation pattern of the isolated element of the array designed for the user segment in a 3 % band: bare aperture at $0.985\, f_0$ (a), LWA at $0.985\, f_0$ (b), bare aperture at f_0 (c), LWA at f_0 (d), bare aperture at $1.015\, f_0$ (e), LWA at $1.015\, f_0$ (f).

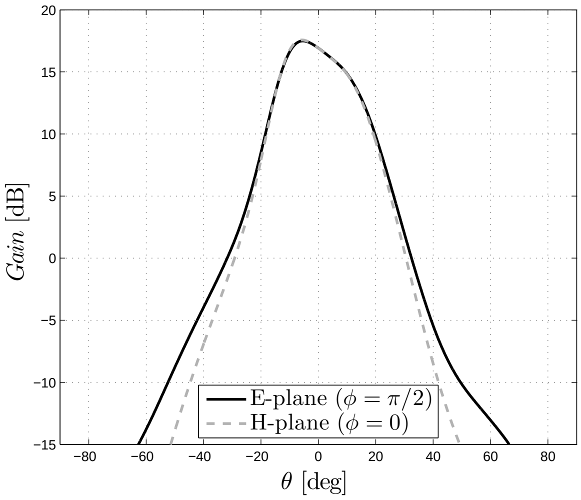

Figure 4.12: Embedded element pattern for the element at the corner of an array of apertures ($\lambda_0 \times \lambda_0$) on a ground plane underneath a dielectric stuperstrate ($\epsilon_r = 10$) forming a Fabry-Perot cavity.

It is worth noting that the effects of the coupling are not negligible once the aperture is embedded in an array configuration [51]. Even though the mutual coupling is lower than -25 dB, it dramatically modifies the shape radiation pattern. As an example, Fig. 4.12 shows the embedded element pattern of the element at the corner of the array, also evaluated with the analysis tool presented in Chapter 2. A clear asymmetry can be noticed along the θ-axis on both E- and H-planes.

4.1.3.2 Array Performance

The performance of the arrays designed for user segment (18×18 elements) are reported in Fig. 4.13. In the whole band, the filtering properties of the leaky-wave solution are fully exploited, as the grating lobe on the H-plane decreases of 7 to 10 dB if compared with the bare case. In the E-plane, the grating lobes of the bare solution are suppressed by the zeros of the element pattern, as also seen in the previous case.

Conversely to the space segment comparison, here the dispersive behavior appears mitigated and the gain remains stable in the whole considered band for the two configurations. Fig. 4.14 reports the broadside gain as a function of the frequency for the bare and the leaky-wave arrays. Also in this case, the gain of a single aperture with the dimension of the array fed by a uniform field distribution is reported. The gain of the two array configurations is comparable in a 8 % bandwidth. Since the bandwidth required

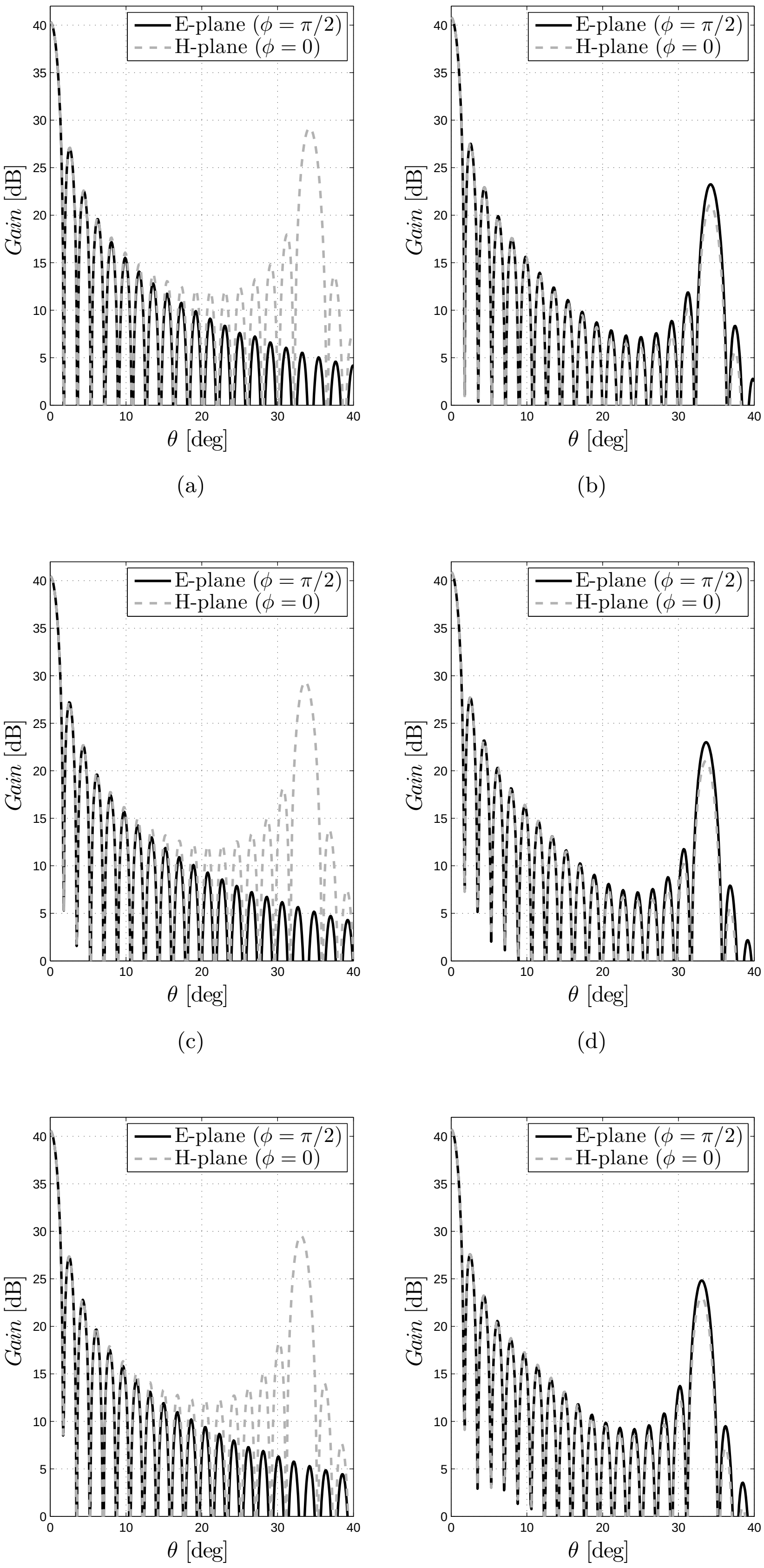

(a) (b)

(c) (d)

(e) (f)

Figure 4.13: Radiation pattern of the 18×18 elements array for the user segment in a 3 % band: bare apertures at $0.985\,f_0$ (a), LWA array at $0.985\,f_0$ (b), bare apertures at f_0 (c), LWA array at f_0 (d), bare apertures at $1.015\,f_0$ (e), LWA array at $1.015\,f_0$ (f).

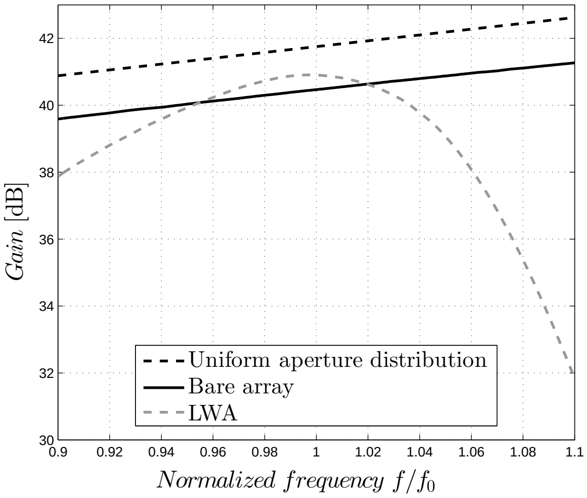

FIGURE 4.14: Arrays with 1.8 λ_0 periodicity and single aperture: broadside gain versus frequency.

for ground terminals is much narrower, a more reflective superstrate could be used to further enhance the gain or to remove some of the elements, reducing the complexity of the system. To quantify the reduction of elements we need a synthesis tool, that will be presented in Chapter 5.

We will not discuss the scanning performance for the array designed for user segment, as in this circumstance it is typically more convenient to perform the scanning mechanically.

To conclude, the superstrate array represents a solid alternative to the classical antenna solutions for ground applications.

4.2 Chessboard Superstrate Dual-Band Array

As clear from the analysis in the previous section, a main design issue when dealing with planar LWAs is the bandwidth limitation. In fact, as the gain of the antenna increases, the bandwidth decreases [29]. Part of the research studies performed during the Ph.D. activity have been devoted to find a way to improve the bandwidth of planar LWAs.

These studies ended up in the patch-superstrate antenna, a novel LWA configuration obtained truncating the superstrate of a regular planar configuration. A similar work has been eventually published by Al-Tarifi et al. in 2015 [69]. The antenna shares the gain enhancement property with the regular Fabry-Perot antennas, but on a larger band.

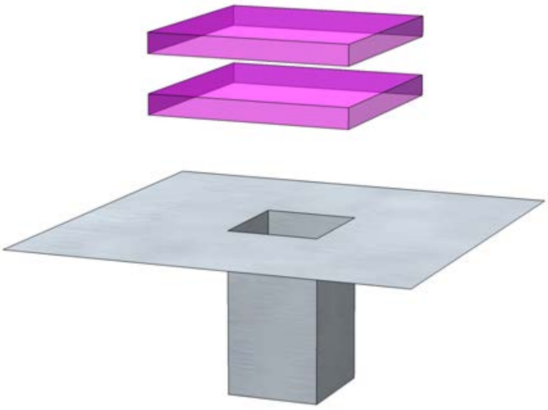

FIGURE 4.15: Patch-superstrate antenna.

The implementation in array configuration is not straightforward and needs a careful design, as a non-negligible empty space must be kept around the element to make it work properly. Since every element has its own superstrate, we decided to implement the patch-superstrate antenna in a dual-band array in K- and Ka-bands, corresponding to the transmit and receive bands of standard broadband satellite communications.

4.2.1 Patch-Superstrate Antenna

The patch-superstrate antenna is shown in Fig. 4.15. As in the classical case of a Fabry-Perot cavity, the antenna is formed by a small aperture on a ground plane underneath a superstrate. In this case, however, the superstrate is truncated. The truncated structure act as a filter for the counterproductive modes not radiating broadside (such the TM_0 typical of these structures) [38]. In fact, the reduced length of the superstrate does not allow the correct excitation of these modes. Furthermore, the gain of the antenna is enhanced by the edge effects [69]. The design parameters of the antenna remain the same in the longitudinal direction, while the size of the patch becomes a design parameter.

The main advantage of this truncated superstrate solution is the increased bandwidth, if compared with the infinite case. Also in this truncated case, an equivalence can be done between structures having different number of layers and permittivities. As an example we consider the antenna analyzed in Chapter 2 (Fig. 2.4), made of two dielectric layers with relative permittivity $\epsilon_r = 4$. We optimize here the length of the dielectric slab using HFSS. The goal is to get the smallest gain variation with the frequency, preserving a similar gain.

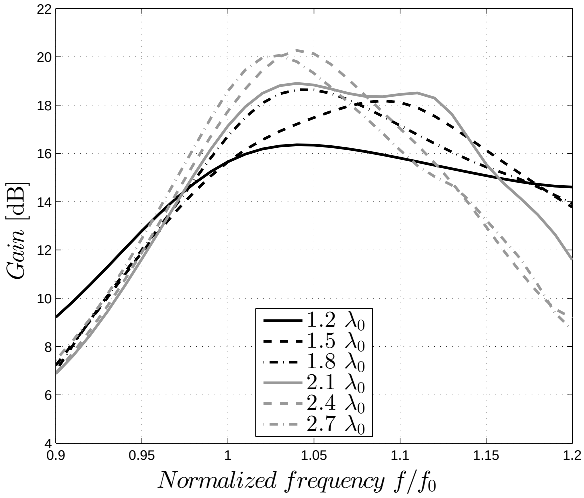

FIGURE 4.16: Broadside gain variation as a function of the frequency using superstrates with different lengths.

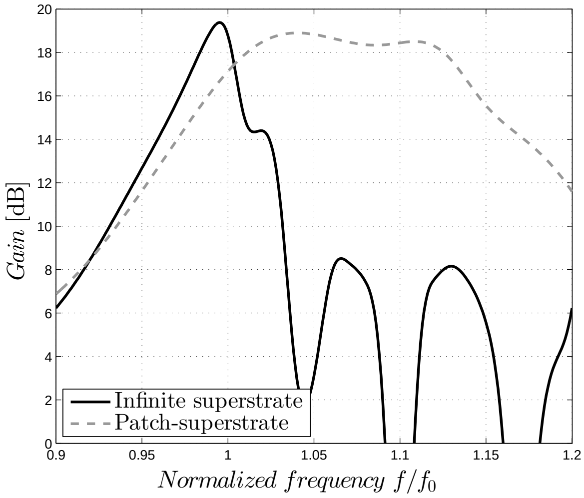

FIGURE 4.17: Broadside gain variation of infinite and optimized truncated cases.

The impact of the length of the superstrate has been simulated on HFSS and is shown in Fig. 4.16, where a square patch-superstrate is employed. Using a short superstrate we increase the bandwidth, but the gain is not maximized. On the other hand, a longer superstrate has an higher gain, but it might lead to a narrow band, tending to the infinite case as expected.

A trade-off between gain and bandwidth is needed. We select the patch-superstrate with the size of the side equal to 2.1 λ_0. The curves in Fig. 4.17 show the frequency dependence of the gain for a classical infinite superstrate and for the truncated superstrate

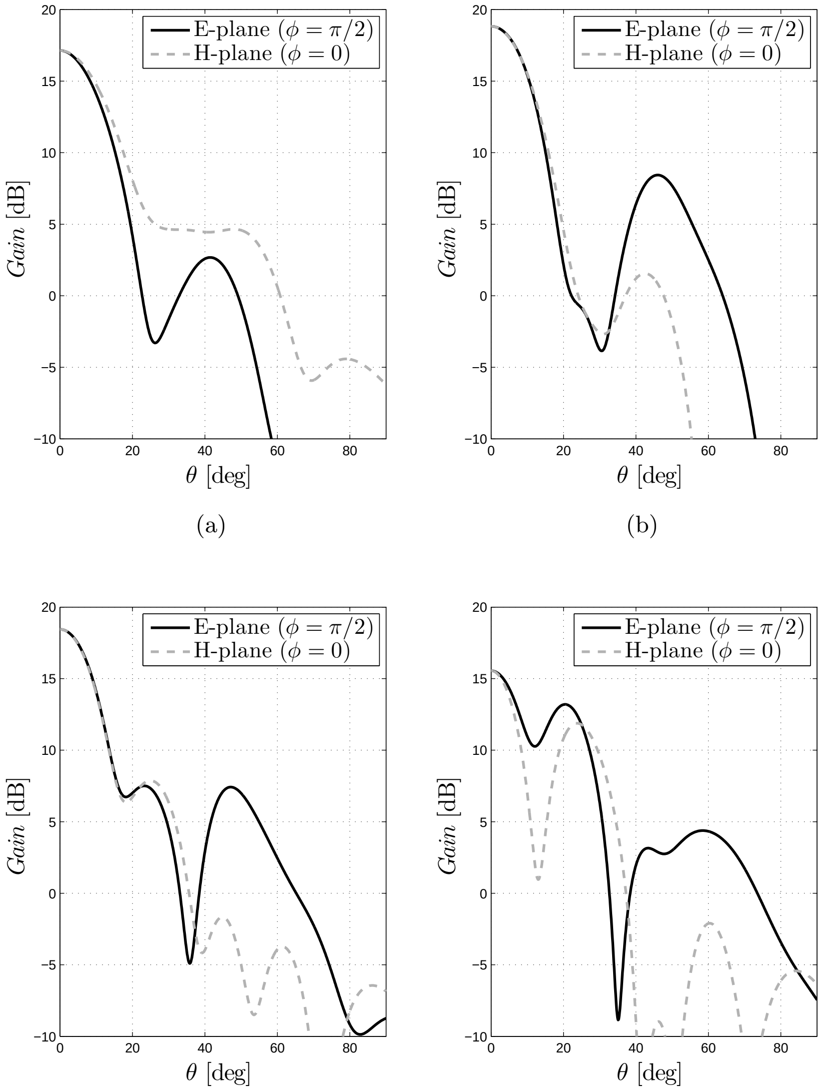

(a) (b)

(c) (d)

FIGURE 4.18: Simulated radiation pattern of the optimized patch-superstrate antenna in a 14 % band: f_0 (a), 1.05 f_0 (b), 1.1 f_0 (c), 1.15 f_0 (d).

configuration, simulated with HFSS. The peak gain of the patch-superstrate is slightly lower, but the 3 dB gain variation bandwidth passes from 3 % to 16 %.

Fig. 4.18 shows the radiation pattern of the proposed structure along a 14 % band. The dispersive behavior of the infinite superstrate case is no more present. As a drawback, the filtering effect on the SLL is mitigated if compared with the classical leaky-wave solution, but the bandwidth is tremendously enlarged.

The performance of a single radiator are outstanding and this solution seems to solve

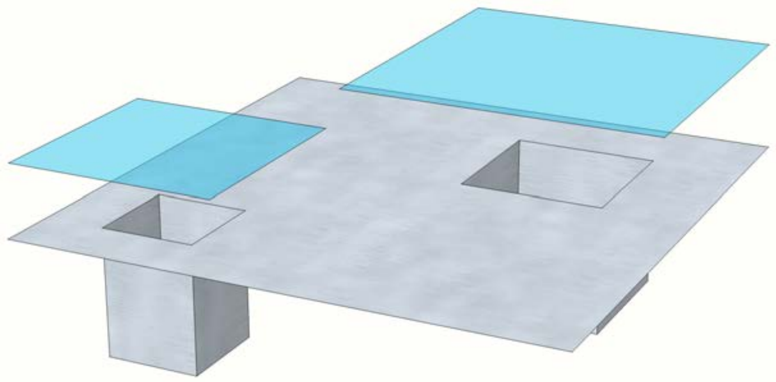

FIGURE 4.19: Unit cell of the dual-band chessboard array (size 41.74 mm × 41.74 mm).

the main issues of the Fabry-Perot cavity antennas, i.e. the narrow bandwidth. However, the implementation in an array configuration is not straightforward. In fact, the antenna needs to be surrounded by an empty region. A trade-off between the size of the superstrate and the interelement distance is needed.

4.2.2 Dual-Band Array

A useful characteristic of the patch-superstrate antenna is that, in array configuration, each element can have a different superstrate. It is interesting to exploit this peculiarity in the design of a dual-band array. In particular, two frequency bands used in satellite communications have been chosen for the design: $17.7 - 20.2$ GHz for Tx (K-band) and $27.5 - 30$ GHz for Rx (Ka-band). Since this array could be used as an on-board satellite antenna, we prefer to move from the dielectric superstrate to a configuration made of impedance sheets, synthesizable using metallic grids. Furthermore, we move to a configuration with a single-layered superstrate, to minimize the interference between elements.

4.2.2.1 Unit Cell Design

Fig. 4.19 presents the unit cell of the dual-band array. The smaller element covers the Ka-band, while the bigger one covers the K-band. The size of the waveguide apertures is $0.7\ \lambda$ at the central frequency of the respective band. The dimension of the unit cell is equal to 41.74 mm $\approx 4\ \lambda$ at 28.75 GHz, central frequency of the higher frequency band. The two elements are disposed in a cater-cornered position in the unit cell,

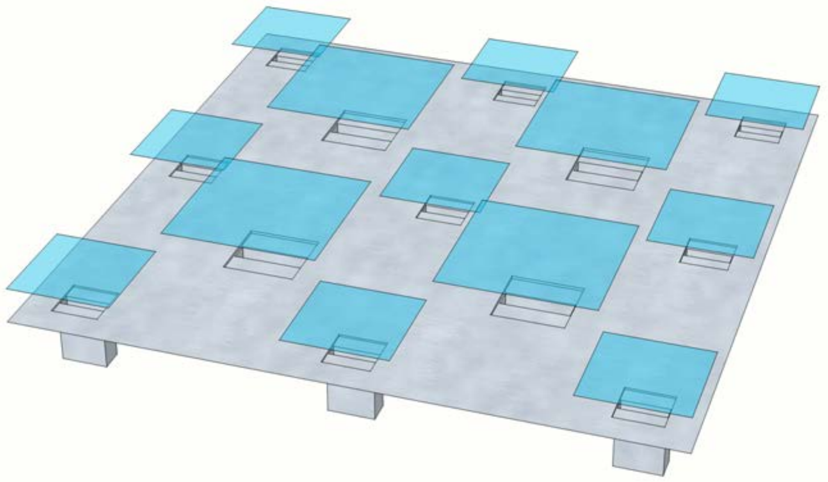

FIGURE 4.20: Optimization setup: the central element is excited and the other elements are connected to matched loads.

minimizing the coupling between the two apertures. Nevertheless, an optimization of the dimension of the superstrate is needed in the embedded configuration. All the following optimizations are performed on the high frequency element, because it is the most sensible to the presence of the neighbors.

The design parameters of the low frequency element are obtained scaling the dimensions of the high frequency element by a factor 1.52 equal to the ratio between the central frequencies of the two considered bands ($1.52 \approx 28.75/18.95$).

Superstrate Size Optimization

The optimization of the high frequency element is performed using the setup in Fig. 4.20: the central element (Ka-band) is the only one excited. It is surrounded by a first ring of 4 elements in K-band and an additional ring of 8 elements in Ka-band. The elements on the two rings are connected to matched loads. This setup allows the evaluation of the radiation characteristics of the central element in a reliable embedded configuration.

The superstrate chosen for the design is a capacitive reactive sheet with impedance $Z_s = -j\,94\ \Omega$ placed 6 mm above the ground plane. In the infinite case, this structure presents similar radiation characteristics as the dielectric structure presented above, with the main couple of leaky-modes radiating at the same angle. The values of impedance and height have been retrieved using the procedure described in [43]. We consider, here, a truncated superstrate with a square shape.

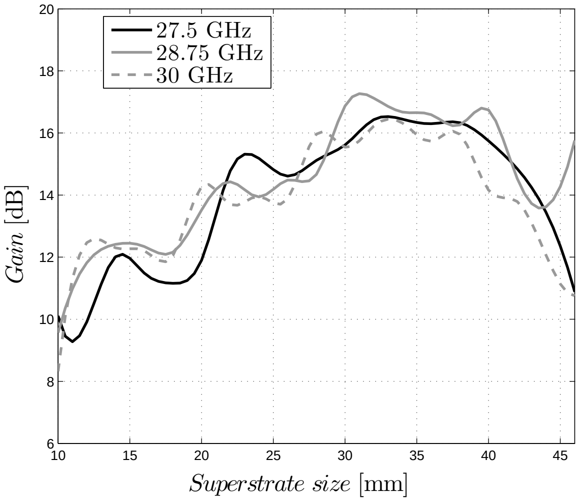

FIGURE 4.21: HFSS simulation of the broadside gain of the element in Ka-band as a function of the lateral size of the square patch-superstrate in the embedded configuration in Fig. 4.20: the solid gray curve refers to the central frequency, the solid black and the dashed gray curves refer to the gain at the lower and higher edges of the band, respectively.

The goal of the optimization is to maximize the gain in the whole band. Fig. 4.21 shows a parametric study performed with HFSS of the broadside gain value as a function of the lateral size of the superstrate. The solid gray curve refers to the central frequency. The other two curves report the gain values at the edges of the band. Increasing the lateral dimension of the superstrate, the directivity increases up to a point where the different impedance sheets start to overlap. Note that a variation of length δ_l of the superstrate for the high frequency element, corresponds to a variation $1.52 \cdot \delta_l$ for the low frequency element.

For the design of the dual-band array we chose a superstrate with a size equal to 32 mm × 32 mm. As shown in Fig. 4.21, this size allows the broadside gain to be maximized in the whole frequency band.

Impedance Sheet Synthesis

We synthesize the impedance sheet using a thin dielectric slab, metallized on both sides. Then, the metallizations are opportunely etched to obtain electrically small metallic square patches. In particular, a thin layer of silicon (relative permittivity $\epsilon_r = 11.9$) has been chosen as a dielectric substrate. HFSS has been used to retrieve the required

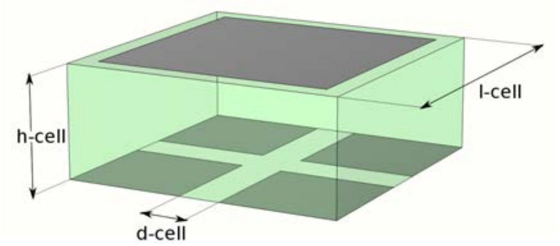

FIGURE 4.22: Unit cell of synthesized impedance sheet: square metallic patches etched on a metallized silicon slab. The parameters of the superstrate are *h-diel* = 0.203 mm, *d-cell* = 0.075 mm, *l-cell* = 0.5 mm.

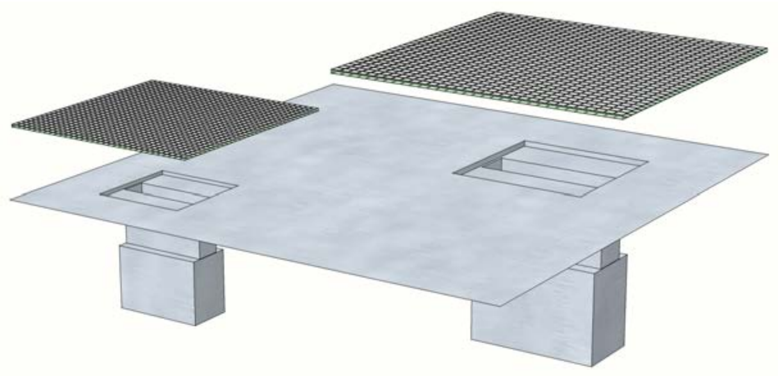

FIGURE 4.23: Unit cell of the dual-band chessboard array.

impedance value of $Z_s = -j\,94\ \Omega$ at the central frequency. The procedure to synthesize the impedance has been presented in Section 3.1.2.1: a single unit cell, as the one shown in Fig. 4.22, is embedded in a cell with periodic boundary conditions in the transverse direction. Two Floquet-ports, placed in the longitudinal direction, excite the structure. The reference planes are positioned at the center of the dielectric. Using this setup, the Z-parameters of the simulation correspond to the impedance of the cell. Referring to Fig. 4.22, the values needed to synthesize a reactance $Z_s = -j\,94\ \Omega$ are: *h-diel* = 0.203 mm, *d-cell* = 0.075 mm, *l-cell* = 0.5 mm. The top pattern is the same as the bottom one, shifted on the transverse direction of *l-cell*/2. The dispersion of this structure is moderately low and the impedance changes of 5 % in the considered frequency band.

The impedance parameters for the low frequency element are obtained scaling the previous ones by a factor 1.52.

Element Design

The final design of the unit cell is shown in Fig. 4.23. A re-tuning of the height of the superstrate has been necessary once the ideal impedance sheet has been substituted with the real one to recover the radiation performance. The reason is linked to the difference on the edge effects once we consider a thick superstrate instead of a sheet. The height of the superstrate for the high frequency element is now 5.5 mm.

The two elements of the unit-cell are connected to standard waveguides, WR-28 and WR-51, for Ka- and K-bands, respectively. The standard waveguides are connected to the square aperture through waveguide matching transition. The reflection coefficient is lower than -10 dB in a $4\,\%$ band for both sources. A larger band can be obtained using more advanced passive matching techniques, as the one presented in Chapter 2.

Fig. 4.24 shows the simulated embedded element pattern for the Ka- and K-band elements at the central frequencies (28.75 GHz for the Ka-band element, 18.95 GHz for the K-band element) and at the edges of their respective bands (27.5 and 30 GHz for the Ka-band element, 17.7 and 20.2 GHz for the K-band element). The simulation setups are the same described before (Fig. 4.20), where the element under analysis is surrounded by a first ring of 4 elements in the other band and a second ring of 8 elements in its same band. This setup allows an accurate representation of the element pattern. The broadside gain proved to be stable in the two bands. All the radiation patterns exhibit good roll-off figures.

4.2.2.2 Array Performance

We analyze here the performance of the truncated superstrate in the dual-band array configuration. The goal is to increase the gain of classical dual-band horn arrays, keeping a large bandwidth.

An arrangement of 20×20 unit cells has been disposed in a square lattice. The periodicity of the array is 41.74 mm $\approx 4\ \lambda$ at the central frequency of the higher band so that the first grating lobe appears for $\theta_{GL} = 14.5^{\circ}$. Since a geostationary satellite intercepts the Earth in an angle of $\pm 8.6^{\circ}$, this periodicity allows to scan the beam for 5°, approximately the size of a continent, without having the grating lobes pointing towards the Earth.

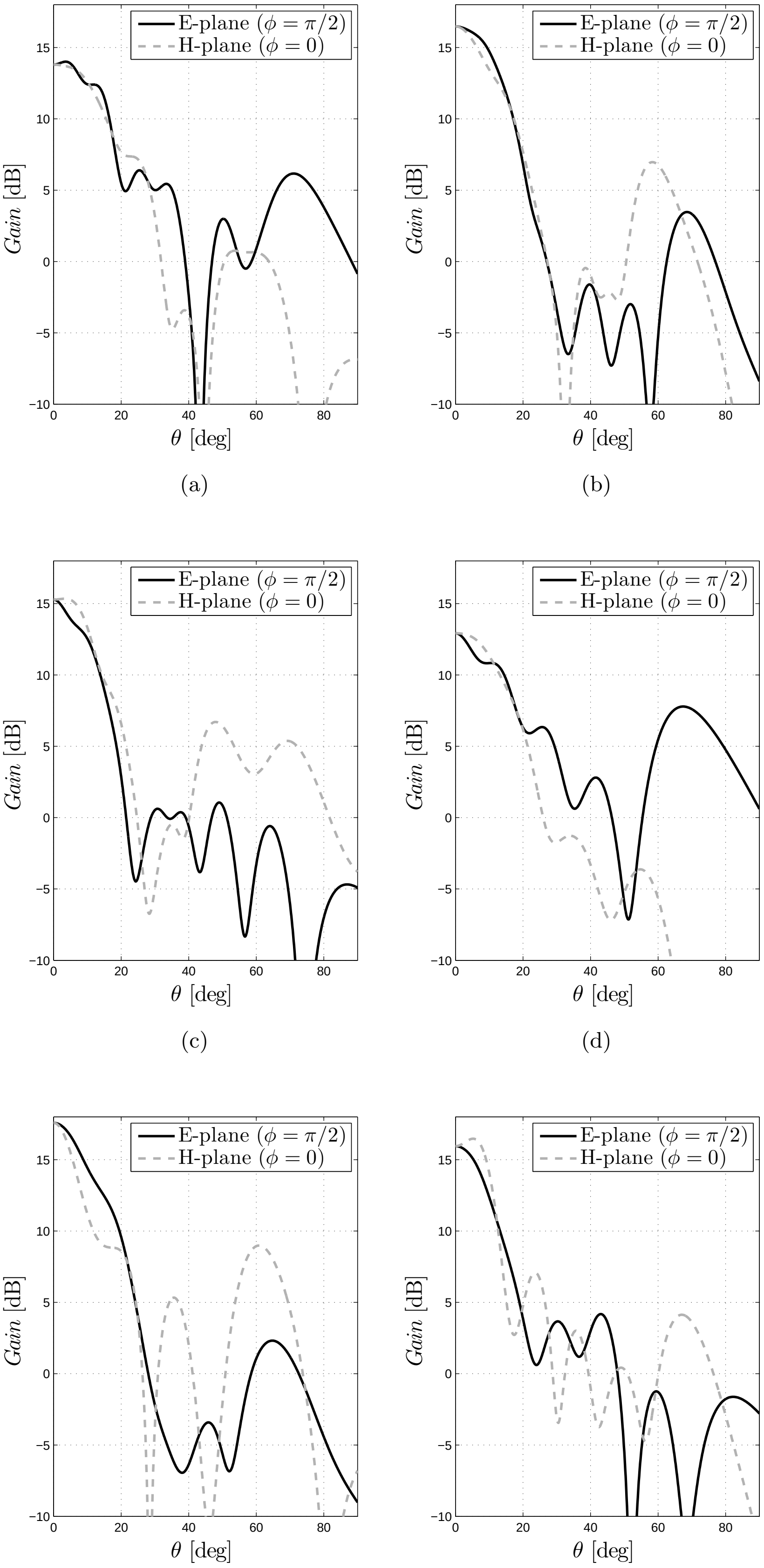

(a) (b)

(c) (d)

(e) (f)

FIGURE 4.24: Simulated radiation pattern of the elements in the embedded configuration: Ka-band element at 27.5 GHz (a), 28.75 GHz (b), 30 GHz (c). K-band element at 17.7 GHz (d), 19.95 GHz (e), 20.2 GHz (f).

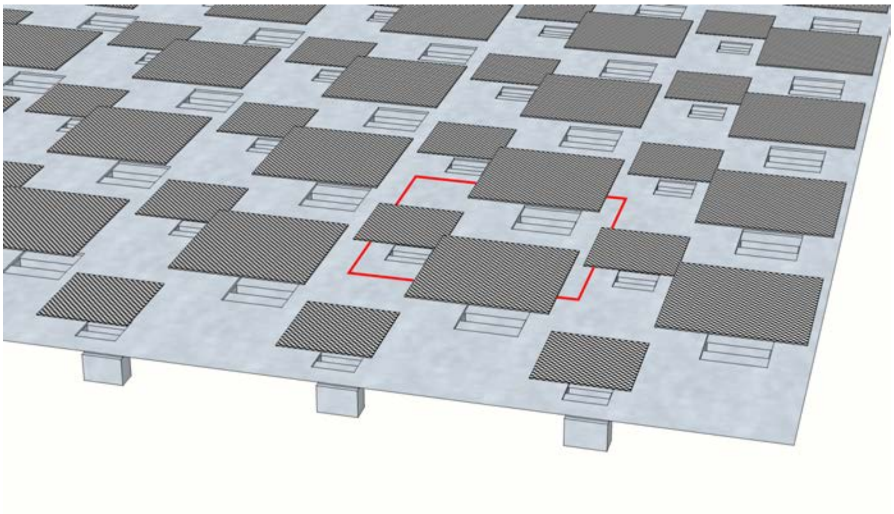

Figure 4.25: Sample of the dual-band chessboard array (unit cell in red).

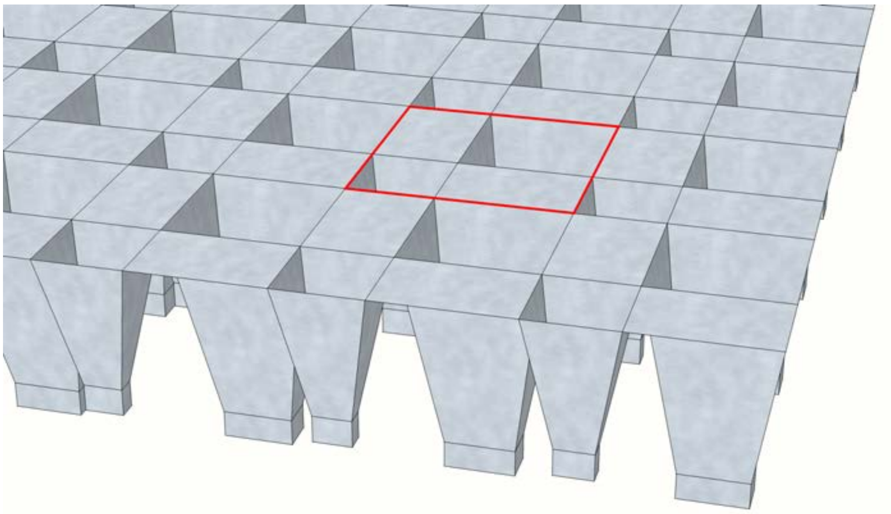

Figure 4.26: Sample of the dual-band benchmark bare array (i) (unit cell in red).

A sample of the array is shown in Fig. 4.25. Two benchmark arrays of square horn antennas have been chosen to test the performance of the proposed array.

The radiation properties of the arrays, shown in the following, are evaluated applying the array factor to the element pattern. The latter is evaluated in its embedded configuration, as for the case analyzed in Fig. 4.20. This approximation leads to accurate results, since we are considering large arrays with regular lattices (Sec. 2.3.1).

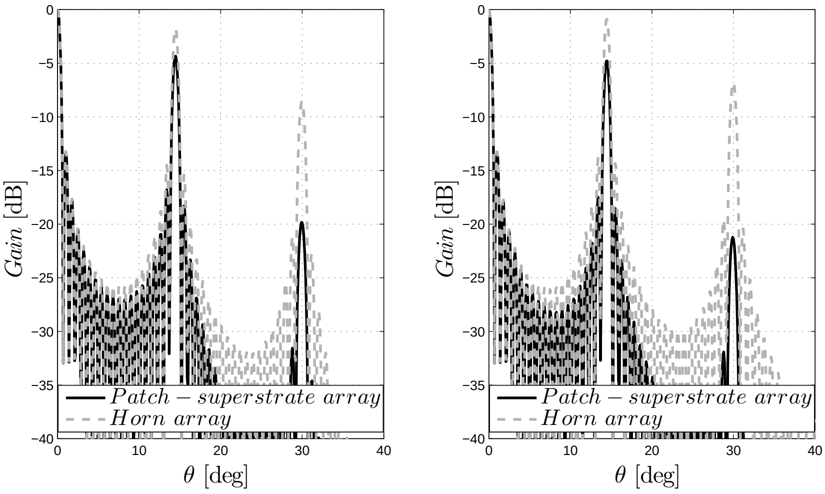

(a) (b)

FIGURE 4.27: Simulated radiation patterns in Ka-band (28.75 GHz) of patch-superstrate array and benchmark bare array (*i*): E-plane (a) and H-plane (b).

Benchmark Bare Array (*i*)

The unit cell of the first test configuration, benchmark bare array (*i*), has the same dimension of the patch-superstrate array (41.74 mm).

It is made of two horn antennas with the same electrical size at the respective design frequency: the horn antenna with a physically smaller aperture is used for Ka-band, while the horn with a bigger mouth for K-band. For both cases, the length of the flare of horn antennas is equal to 40 mm. The Ka-band horns are fed by WR-28 standard waveguides, while the K-band horns are fed by WR-51 waveguides. The size of the radiating aperture is 1.58 $\lambda \times 1.58\ \lambda$ at the wavelength of the central frequency of the respective band. The selected size allows the maximization of the dimension of the square apertures in the unit cell. Also in this case, an array of 20 × 20 unit cells is considered. A sample of the array is shown in Fig. 4.26.

A comparison between the radiation patterns of the patch-superstrate array and the benchmark bare array (*i*) is reported in Fig. 4.27 and Fig. 4.28 for the central frequency of the Ka- and K-bands, respectively. For both the bands, the use of the patch-superstrate array leads to a significant reduction of the side lobe envelope. Also the level of the first grating lobe is reduced: in K-band the grating lobe level is reduced by 4 dB and 6 dB

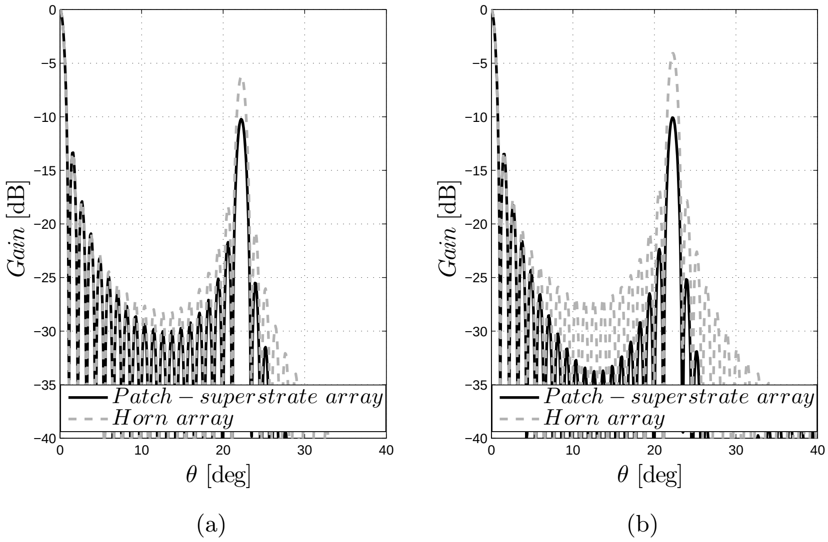

(a) (b)

FIGURE 4.28: Simulated radiation patterns in K-band (18.95 GHz) of patch-superstrate array and benchmark bare array (i): E-plane (a) and H-plane (b).

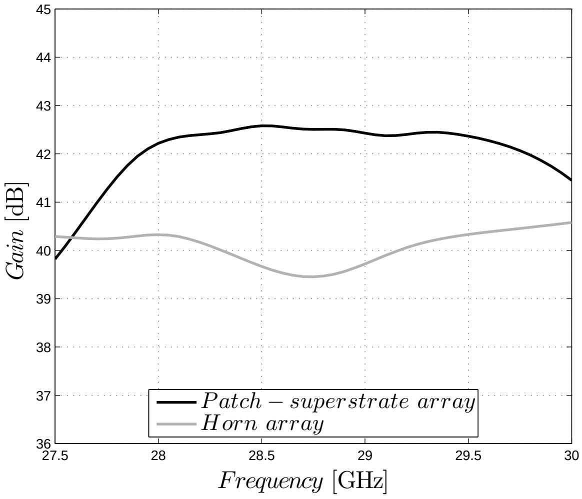

FIGURE 4.29: Broadside gain as a function of the frequency for patch-superstrate array and benchmark bare array (i) in Ka-band.

on E- and H-plane, respectively, while in Ka-band is reduced by 2.5 dB and 3.9 dB on E- and H-plane, respectively.

The patch-superstrate configuration is, indeed, more directive than the benchmark bare array (i). The frequency variation of the broadside gain is shown in Fig. 4.29 and Fig. 4.30 for Ka- and K-bands, respectively. The gain of the proposed array is higher than the one of the horn array in almost all the desired bands.

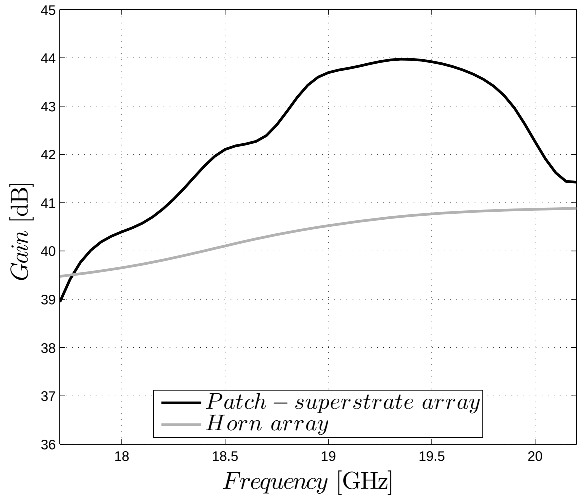

Figure 4.30: Broadside gain as a function of the frequency for patch-superstrate array and benchmark bare array (*i*) in K-band.

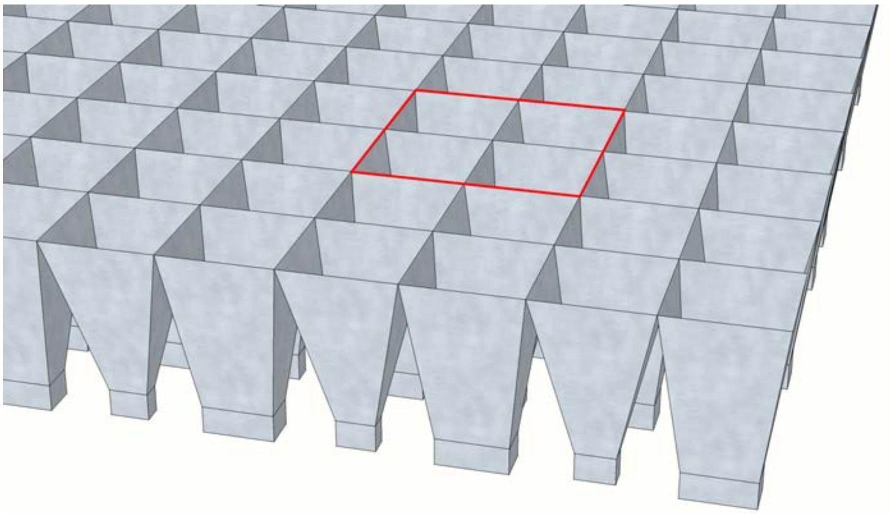

Figure 4.31: Sample of the dual-band benchmark bare array (*ii*) (unit cell in red).

Benchmark Bare Array (*ii*)

A second test configuration, the benchmark bare array (*ii*), has been designed using the same arrangement of 20 × 20 unit cells in a square lattice with periodicity 41.74 mm. In this configuration, shown in Fig. 4.31, the unit cell is formed by four horn antennas: two horns in cater-cornered position are for Ka-band and the remaining two for K-band. The horn are fed by WR-28 and WR-51 standard waveguides and their length is 40 mm.

The advantage of this solution is that it uses all the available space of the antenna. On the other hand, the gain is different for the two frequency bands, as the aperture for the

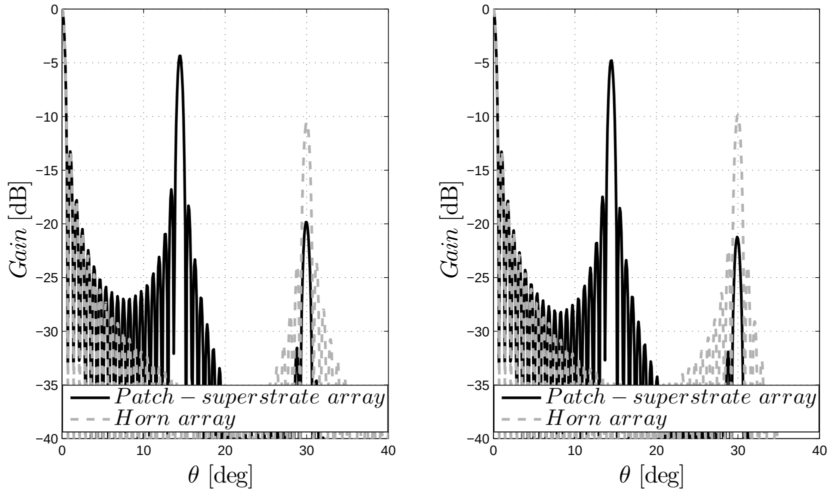

(a) (b)

FIGURE 4.32: Simulated radiation patterns in Ka-band (28.75 GHz) of patch-superstrate array and benchmark bare array (*ii*): E-plane (a) and H-plane (b).

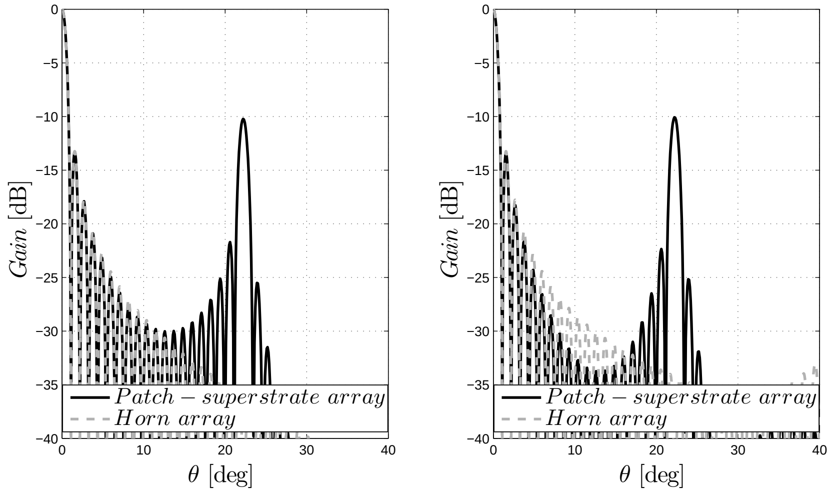

(a) (b)

FIGURE 4.33: Simulated radiation patterns in K-band (18.95 GHz) of patch-superstrate array and benchmark bare array (*ii*): E-plane (a) and H-plane (b).

low frequency case is electrically smaller than the aperture for the high frequency case.

The unit cell of the benchmark bare array (*ii*) has two radiating apertures per frequency band. The array has the same size, but an amount of elements double with respect to the patch-superstrate case. For this reason, the position of the first grating lobe of the benchmark bare array (*ii*) corresponds to the position of the second grating lobe of the

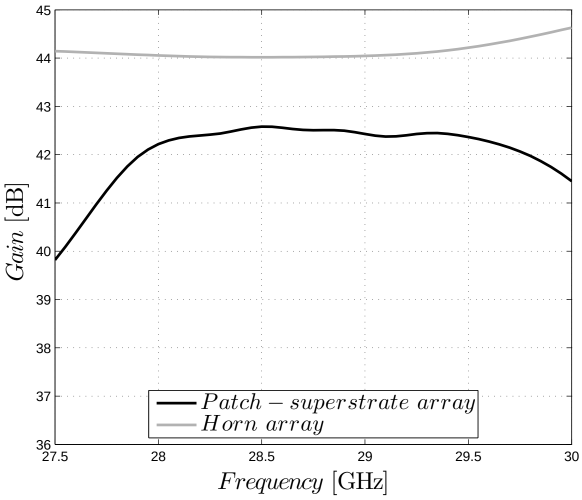

FIGURE 4.34: Broadside gain as a function of the frequency for patch-superstrate array and benchmark bare array (*ii*) in Ka-band.

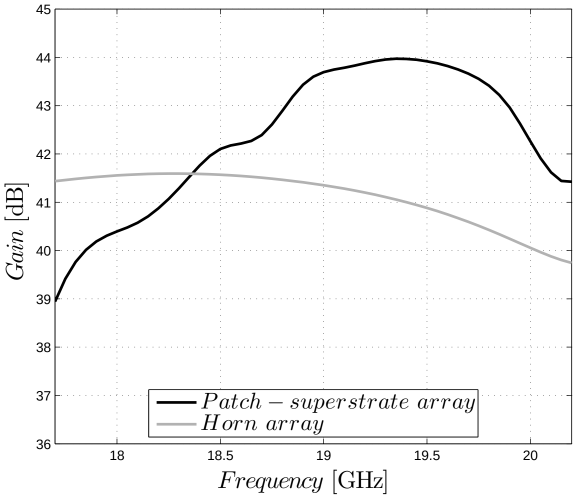

FIGURE 4.35: Broadside gain as a function of the frequency for patch-superstrate array and benchmark bare array (*ii*) in K-band.

patch-superstrate case. The radiation pattern is reported in Fig. 4.32 and Fig. 4.33 for the central frequencies of the Ka- and K-band cases, respectively.

The gain of the benchmark structure in the Ka-band is more than 1 dB higher than the one of the patch-superstrate array, as shown in Fig. 4.34. In this band, the two horns are, indeed, electrically large ($2\,\lambda \times 2\,\lambda$). In the K-band, instead, the patch-superstrate array is more directive than the bare array in the largest part of the considered band.

When comparing the proposed patch superstrate array with benchmark bare array (*ii*), the advantages from an electromagnetic point of view are not as strong as for the benchmark bare array (*i*). However, other considerations might be done concerning the increased complexity and bulkiness of the benchmark bare array (*ii*), which has a number of elements double compared to the proposed structure.

Array of Dual-Band Horns

An alternative benchmark solution is an array made of dual-band horn antennas. Each horn fills the 41.74 mm×41.74 mm cell, covering both K- and Ka-bands by using a diplexer. The effective area of the antenna appears increased and the gain is higher than the one of the proposed patch-superstrate structure in both the bands. However, a full comparison with this kind of antenna design should be performed at system level and is beyond the scope of this study.

4.3 Summary

In this chapter we analyzed the possibility to reduce the number of elements of classical aperture antenna arrays using arrangements of small waveguide apertures underneath a superstrate.

A parametric study has been presented in the first section, to understand the effects of the superstrate structure on the array gain. Interelement distance and permittivity of the dielectric superstrate are the parameters of the study. The results were needed to understand and quantify the benefits and the limitation of the superstrate, such as the reduced bandwidth. Following these results, two LWA array have been designed, for space and user segments. The large periodicities ($3 \sim 4\,\lambda$) combined to the high aperture efficiencies make the LWA unsuitable for on-board satellite applications, when comparing just the broadside gain. In fact, the high reflectivity of the superstrate needed to reach the high gain value of the benchmark solution, leads to a bandwidth too narrow for the application. On the other hand, when dealing with smaller periodicities and bandwidths as for the user segment, the LWA array represents a solid alternative to the benchmark solutions. In particular, we analyzed a configuration with interelement distance equal to $1.8\,\lambda$. The designed leaky-wave-based array has a broadside gain comparable to the one of the benchmark solution in a $8\,\%$ bandwidth. Since we are typically dealing with smaller bands, one could increase the reflectivity of the superstrate to enhance the gain of the structure and, eventually, reduce the number of elements. The reduction of elements on the regular lattice would increase and/or modify the direction of the grating lobes. A synthesis procedure, as the one presented in Chapter 5, can be used to maintain the grating lobes under control.

A novel configuration, the patch-superstrate antenna, has been introduced in the second section. This antenna consists of a regular Fabry-Perot cavity with a truncated superstrate. The main advantage of this solution is the enlargement of the bandwidth, if compared with fully-covering superstrate structures. A dual-band array for on-board satellite applications has been designed using the patch superstrate antennas. Each unit cell is formed by two sources, one for Ka- and one for K-band. The gain performance of the proposed array has been tested using two horn arrays as a benchmark. The first benchmark array has been designed to have two apertures, one for each band, with the same electrical size. The gain of the patch-superstrate array is higher than the horn array on both the considered bands. The second benchmark array has been designed to maximize the radiating aperture of the array. The unit cell is formed by four horns, two for each frequency band. The horns have the same dimension and the electrical size is different for the two frequency bands. In K-band, the gain performance of benchmark and patch-superstrate arrays are comparable, but in Ka-band the benchmark array has an higher gain. However, the horn array might result more complex and bulky, since it has a number of elements double compared to the proposed structure.

Chapter 5

Array Synthesis

In the previous chapter we have seen how the superstrate configuration can be efficiently used for the design of antenna arrays for the user segment. As extensively discussed in Chapter 1, a main design goal for the design of antennas for this segment is the reduction of the interference with the other Earth equipment. Strict rules have been drawn for this scope [4], fixing the limits for the maximum accepted SLL (side lobe level).

In this chapter we introduce two of our works addressed to the control of the SLL. In the first section we present a synthesis method for thinned leaky-wave arrays. An iterative optimization procedure based on a convex ℓ_1 minimization is used to reduce the number of array elements, maintaining the radiated field within a predefined mask and controlling the SLL. All the embedded element patterns are evaluated for each source through the fast tools developed in Chapter 2, taking into account the effects of the mutual coupling during the optimization procedure. The use of a superstrate provides array structures with a reduced number of elements and enhanced aperture efficiency with respect to configurations without superstrate. In the second section, we introduce the irregular superstrate array, a novel technique to control the SLL of the array using an isophoric excitation. In this work, we recreate the desired power distribution of the excitation moving it to the directivity of the element. The array is fed with a uniform excitation and an irregular superstrate is used to change the directivity of each element. Design techniques are given in the chapter. Finally, a design is performed on a linear array of 20 elements.

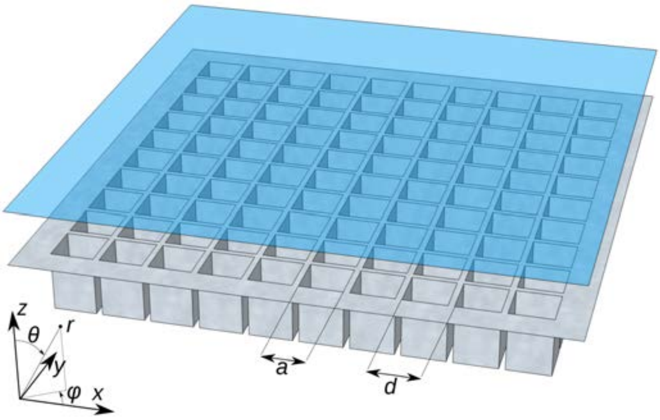

FIGURE 5.1: Planar superstrate array structure.

5.1 Thinned Array Synthesis

Superstrate antennas are suitable candidates for sparse or thinned array configurations. They allow to mitigate the effects of the reduced aperture efficiency [16], since each array element possesses a radiating aperture larger than its physical size. However, the synthesis of a configuration generating shaped or focused beams fulfilling predetermined constraints is not straightforward. As a matter of fact, the mutual coupling due to the reflective layers strongly influences the radiation pattern and must be considered during the thinning procedure [29].

Here we propose a synthesis procedure for the thinning of planar LWA arrays. In particular, we extend the optimization procedure described in [70] to a more general case of superstrate configurations, taking into account the mutual coupling between array elements. The scattering parameters are evaluated analytically with and without the superstrate (in the following we will refer to the latter configuration as bare case) through the fast Green's function spectral approach presented in Chapter 2. Thereupon, the scattering parameters are used in the computation of the total electric field to perform the array synthesis. The goal of the optimization is to minimize the number of array elements, while maintaining the radiation pattern within a defined mask. We reach the target by using an iterative procedure based on a convex ℓ_1 minimization [71].

As shown in this section, the reduced side lobe level introduced by the superstrate on the element pattern allows to further reduce the number of elements in the LWA array, if compared with a bare array synthesized with the same constraints. Despite the fewer elements, the superstrate array presents an enhanced gain. On the other hand, the bandwidth decreases as the reflectivity of the superstrate increases [29, 72] and a trade-off is required, as presented in the followings.

5.1.1 Problem Formulation

An iterative optimization procedure based on the convex ℓ_1 minimization has been developed to reduce the number of elements in linear and planar phased arrays [70, 71, 73]. This synthesis procedure is applied here to arrays of generic apertures over a ground plane, with and without covering superstrate. The superstate can be made of dielectric slabs, impedance sheets or metasurfaces. In the statement of the problem we consider a square arrangement of N array elements lying on the (x, y)-plane, as represented in Fig. 5.1. In the following we assume the electric field on the aperture feed polarized along the y-axis. The extension to other polarizations is straightforward.

5.1.1.1 Evaluation of the Array Radiation Pattern

The radiation pattern of the array is computed considering the effects of the mutual coupling between elements. This is extremely important for a superstrate configuration due to the impact of the mutual coupling on the radiation pattern [29].

The electric field radiated by the array can be expressed as

$$\mathbf{E}^a(\theta, \phi) = \sum_{n=1}^{N} \mathbf{E}_n^e(\theta, \phi) \cdot w_n, \tag{5.1}$$

where w_n is the complex excitation of the n^{th} array element to be determined and $\mathbf{E}_n^e$ is the corresponding embedded element pattern, i.e. the pattern of the array when the n^{th} element is excited and all the others are connected to matched loads [50]. The embedded element pattern can be evaluated using the expression (2.11). The evaluation of the radiated field through the embedded element pattern allows us to consider the mutual coupling between the elements. For this purpose, the Y- and S-matrices have to be calculated. This can be done analytically using the expressions (2.13) and (2.14).

5.1.1.2 Thinned Array Synthesis

Considering the planar array on the (x, y)-plane represented in Fig. 5.1, we describe the synthesis procedure on the two-dimensional (θ, ϕ)-space.

The array synthesis is done by imposing a mask to the normalized total radiated field $\mathbf{E}^a(\theta, \phi)$ given by (5.1): the main beam is pointing at (θ_0, ϕ_0), while a maximum side lobe level (SLL) $\rho(\theta, \phi)$ is imposed over the angular region T. We can express these constraints as follows

$$\text{Mask} \begin{cases} \Re\{\mathbf{E}^a(\theta_0, \phi_0)\} = 1 \\ |\mathbf{E}^a(\theta, \phi)| \leq \rho(\theta, \phi), \forall(\theta, \phi) \in T \end{cases} . \tag{5.2}$$

Note that enforcing the real part of the derived field, instead of the amplitude, is necessary to maintain the convexity of the problem [70]. It leads to the same results as constraining the amplitude, since the excitations are determined up to a phase.

The goal of the optimization procedure is to minimize the number of excitations, described in the excitation vector $\boldsymbol{w}$. This optimization problem can be expressed in a mathematical form as

$$\min_{\boldsymbol{w}} ||\boldsymbol{w}||_{\ell_0} \text{ subject to Mask}, \tag{5.3}$$

where $||\boldsymbol{w}||_{\ell_0} = |\{i : w_i \neq 0\}|$ counts the number of non-zero excitations. However, minimizing the ℓ_0 norm is not suitable for practical use because it leads to intractable combinatorial searches [71]. A good and well-known alternative is the minimization of the ℓ_1 norm

$$\min_{\boldsymbol{w}} ||\boldsymbol{w}||_{\ell_1} \text{ subject to Mask}, \tag{5.4}$$

with $||\boldsymbol{w}||_{\ell_1} = \sum_{n=1}^{N} |w_n|$. Problem (5.4) is convex and can therefore be efficiently solved [71] using available routines. In our case, the MATLAB convex optimization toolbox CVX [74] is used.

The minimization of the ℓ_1 norm leads to one of the following results:

(i) A solution exists and the excitation vector $\boldsymbol{w}$ presents some zeros, i.e. not all the sources are excited.

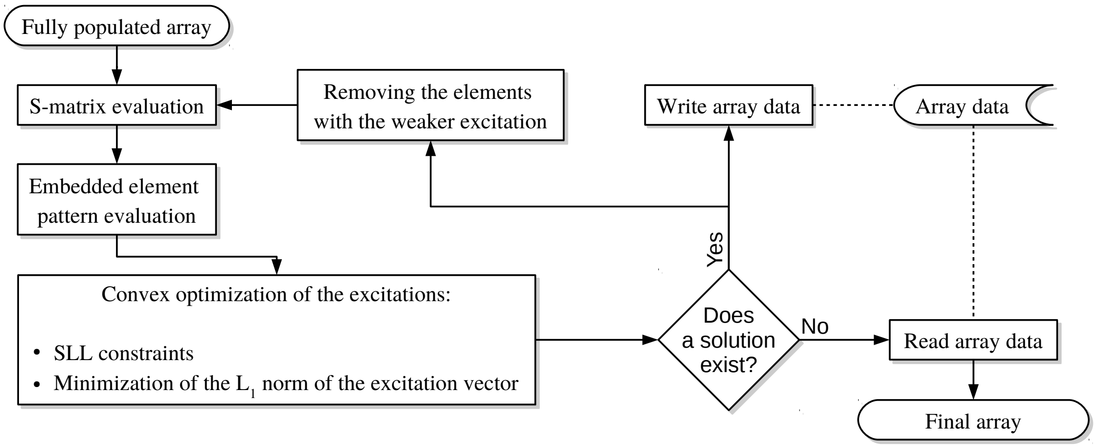

FIGURE 5.2: Optimization procedure: the starting point is a fully populated array. At each cycle, the embedded element pattern is evaluated for each source. The ℓ_1 norm minimization is applied on the excitation vector, considering the constraints on the SLL. If a solution is found, the elements with weaker excitation are removed and the cycle restart on this new array configuration. If there is no solution, the optimization ends. The final array structure is the last existing configuration.

(*ii*) A solution exists and the excitation vector $\boldsymbol{w}$ does not present any zero, i.e. all the sources are excited.

(*iii*) There is no solution, i.e. no excitation set allows the compliance with the mask.

If there is no solution at the first step of the optimization, this means that the constraints are too stringent for the given array and/or specifications.

An iterative synthesis procedure is used to perform the array thinning. A fully populated array can be used as a starting point. The periodicity of the lattice is chosen smaller than the free-space wavelength λ_0, to avoid appearance of grating lobes in the visible region. The optimization process consists of the following steps:

1. Evaluate the S-matrix (formulae (2.13) and (2.14)) and the embedded element pattern (formula (2.11)) for each element of the array. Then solve the problem (5.4),
2. If a solution exists (cases (*i*) and (*ii*)), remove the elements with the weakest excitation from the array and move to step 1. If there is no solution (case (*iii*)), stop the iterative process and give as output the array obtained in the previous cycle.

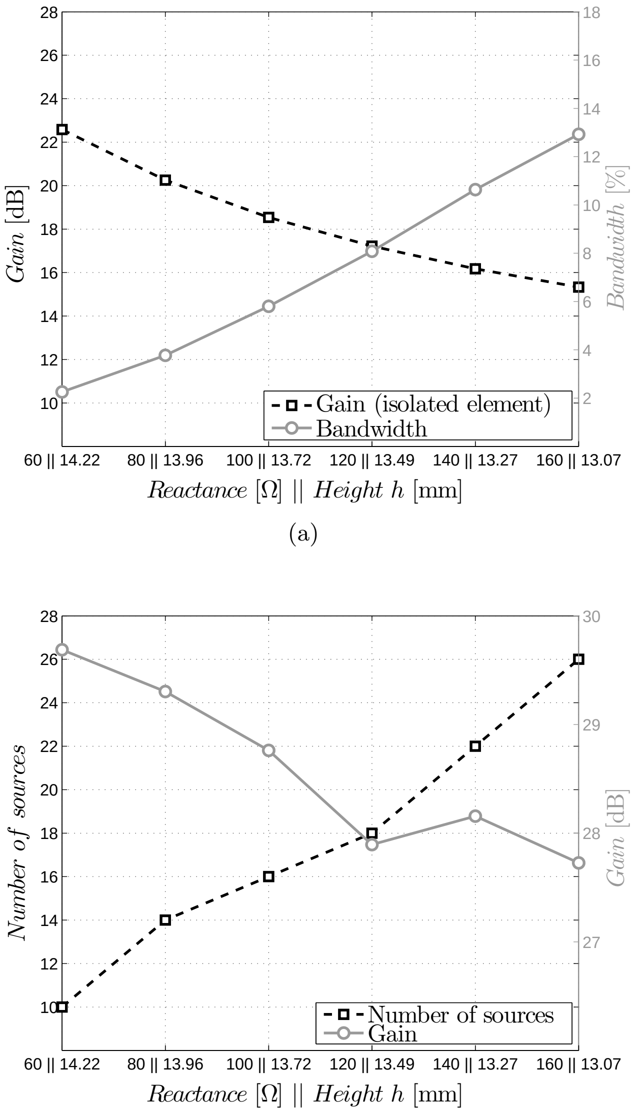

(a)

(b)

FIGURE 5.3: Parametric study of the superstrate configuration varying the parameters of the superstrate. The gain and bandwidth dependencies are shown in (a) for the isolated element. The results of the optimizations on the superstrate array are shown in (b) in terms of number of sources and gain.

The optimization routine is graphically represented by the flow chart in Fig. 5.2.

Contrary to [70, 73], the coupling between the elements is considered in this synthesis procedure. This implies that the element patterns $\mathbf{E}^e$ change at each iteration because of the array thinning.

The result of the iterative process provides a thinned array with a radiation pattern fitting the mask.

5.1.2 Parametric Analysis

The use of leaky-wave sources radically changes the thinning process of a phased array. In particular, the effective radiating aperture of each elementary source is larger in a superstrate configuration with respect to the bare case. This provides more degrees of freedom in shaping the radiation pattern and at the same time reducing the number of elements with an increased gain and aperture efficiency. On the other hand, highly reflective superstrates drastically affect the bandwidth of the antenna and the mutual coupling among the sources of the array [29]. For this reason, a crucial point in the array design is the trade-off between gain enhancement and antenna bandwidth.

A parametric study has been performed in order to understand the effects of the Fabry-Perot cavity in the optimization process. In this study, an inductive impedance sheet is placed above the radiating square waveguide apertures (side $a = 0.7\lambda_0$) etched on the ground plane. The design frequency is $f_0 = 10$ GHz. Note that the following conclusions still hold choosing different design parameters and/or kind of superstrate.

The properties of the superstrate configurations used in the parametric study are shown in Fig. 5.3. The values of reactances considered are between 60 Ω and 160 Ω. The distances h of the superstrate above the ground plane is within 13.07 mm (least directive source) and 14.22 mm (most directive source). The heights are selected in such a way to have the main couple of leaky-poles radiating close to broadside, maximizing the gain for each surface impedance. The gain of the isolated element and its bandwidth are plotted in Fig. 5.3 (a). In this case, the bandwidth is defined as the frequency range with a 3 dB variation of the broadside gain and is reported in its percentage form. A single antenna in the most directive considered configuration has a gain of 22.6 dB, but a bandwidth close to 2 %. The gain in the least directive case is much lower, 15.3 dB, and the bandwidth is almost 13 %.

The results of the thinning process are reported in Fig. 5.3 (b). The starting point is the same for all the array configurations: an arrangement of 10×10 square apertures (side $a = 0.7\lambda_0$) opened in a square lattice (interelement distance $d = 0.8\lambda_0$) underneath a reactive sheet, as in Fig. 5.1. For this parametric study we considered a pencil beam synthesis. The main beam is pointing at broadside ($\theta_0 = 0°$) and a SLL lower than -20 dB is required for $|\theta| > 10°$ on every azimuthal plane. The use of a highly reflective superstrate allows a greater reduction of the number of array elements and, at the same

Table 5.1: Normalized excitations of the superstrate thinned array in Fig. 5.4.

Element #	Position $x/\lambda_0,\ y/\lambda_0$	Excitation Amplitude
1	2.4, 0.0	0.482
2	1.6, 1.6	0.63
3	3.2, 1.6	1
4	5.6, 1.6	0.634
5	0.0, 2.4	0.614
6	4.8, 2.4	0.684
7	1.6, 3.2	0.874
8	3.2, 3.2	0.85
9	7.2, 3.2	0.432
10	0.0, 4.0	0.432
11	4.0, 4.0	0.85
12	5.6, 4.0	0.874
13	2.4, 4.8	0.684
14	7.2, 4.8	0.614
15	1.6, 5.6	0.634
16	4.0, 5.6	1
17	5.6, 5.6	0.63
18	4.8, 7.2	0.482

time, an enhancement of the broadside gain, if compared with a less reflective case, at the expense of a reduced bandwidth. Even in the most directive configuration, the mutual coupling remains lower than -15 dB, thanks to the increased distance between the sources [29]. The limiting factor in the choice of a highly reflective configuration is, indeed, the bandwidth.

5.1.3 Thinned Array Design

In this section we analyze a single superstrate thinned array configuration in order to understand its capabilities in a realistic environment. A complete design is performed, analyzing the reliability of the optimization tool and the effects of the matching network on the radiation pattern. To underline the benefits of the superstate configuration, the designed superstrate array is, then, compared with two bare array antennas, synthesized using the same specifications. The use of the superstrate leads to a considerable reduction of number of elements, if compared with the bare benchmark solutions.

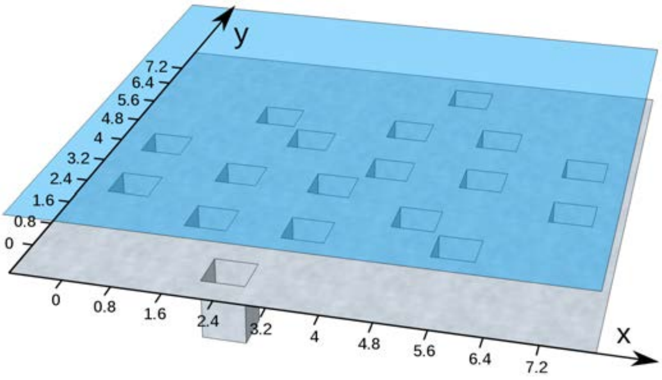

FIGURE 5.4: Synthesized superstrate array. The array is composed by an arrangement of 18 square waveguide apertures in a ground plane. The superstrate is a reactive sheet with surface impedance $Z_s = j\,140\ \Omega$ placed at an height of $h = 13.2$ mm above the ground plane. On the axes, the distance is reported in wavelengths λ_0.

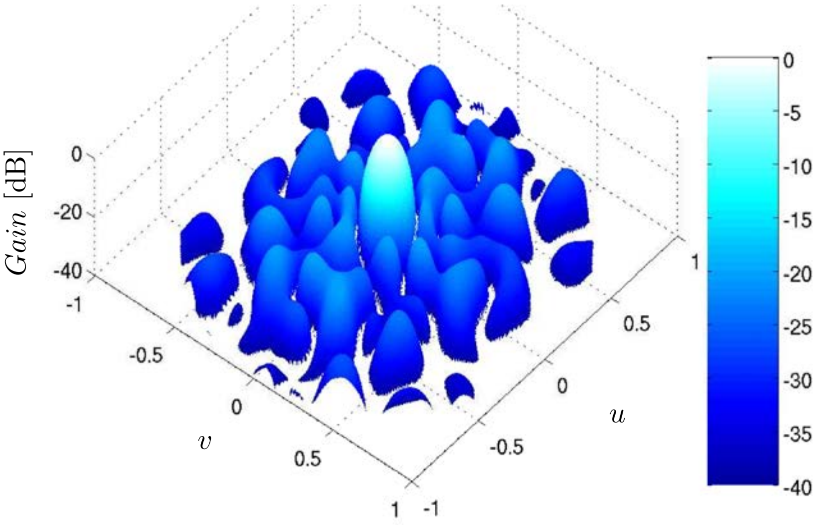

FIGURE 5.5: Radiation pattern of the superstrate array in Fig. 5.4 at the design frequency ($f_0 = 10$ GHz) evaluated using our in-house analysis tool. The synthesized array produces a radiation pattern fitting the defined mask. The radiation pattern is represented in the u/v coordinate system, with $u = \sin\theta\cos\phi$ and $v = \sin\theta\sin\phi$.

A planar array formed by the same arrangement of 10×10 square waveguide apertures as in the previous Section (side $a = 0.7\lambda_0$, interelement distance $d = 0.8\lambda_0$) has been selected as a starting point for the optimization. As in the previous cases, the design frequency is $f_0 = 10$ GHz. The specifications of the design are a main beam radiating broadside $\theta_0 = 0°$, a SLL lower than -20 dB for $|\theta| > 10°$ on every azimuthal plane and a bandwidth of 7%. An impedance sheet has been chosen in light of the trade-off between directivity and bandwidth. A superficial reactance with impedance $Z_s = j\,140\ \Omega$ has been placed above the array at an height $h = 13.2$ mm. The height has been slightly

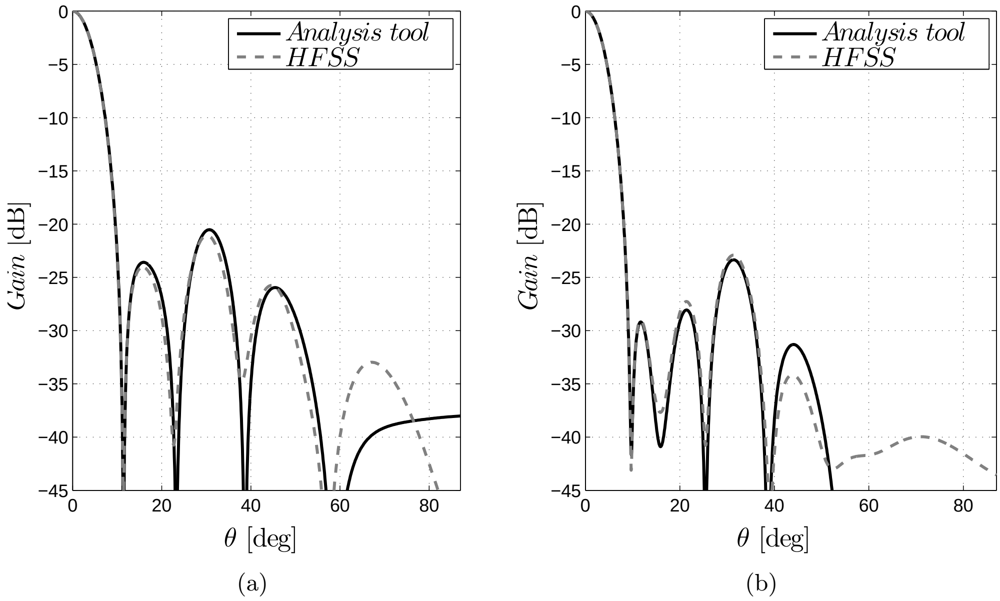

(a)

(b)

FIGURE 5.6: Comparison between the radiation patterns of the array in Fig. 5.4 at the design frequency ($f_0 = 10$ GHz) evaluated with the analysis tool (solid curves) and HFSS (dashed curves) in E-plane ($\phi = 90°$) (a) and H-plane ($\phi = 0°$) (b).

tuned (with respect to the optimization performed in Section 5.1.2) in order to further decrease the number of sources to the detriment of the broadside gain.

5.1.3.1 Synthesis Results

The amount of time necessary to perform the whole synthesis is about 15 minutes on our standard workstation. The final structure, shown in Fig. 5.4, consists of a sparse arrangement of only 18 elements. No symmetries have been used during the optimization process.

It is worth noting that during the synthesis of such a sparse configuration, the optimization tool must control also the level of the grating lobes. This is particularly challenging when designing thinned arrays as the distance between elements remains a multiple of the original array spacing.

The derived excitations for the elements of the arrays are given in Table 5.1. The maximum phase difference between the elements of the array is very small (9°) and will be neglected during the following analysis.

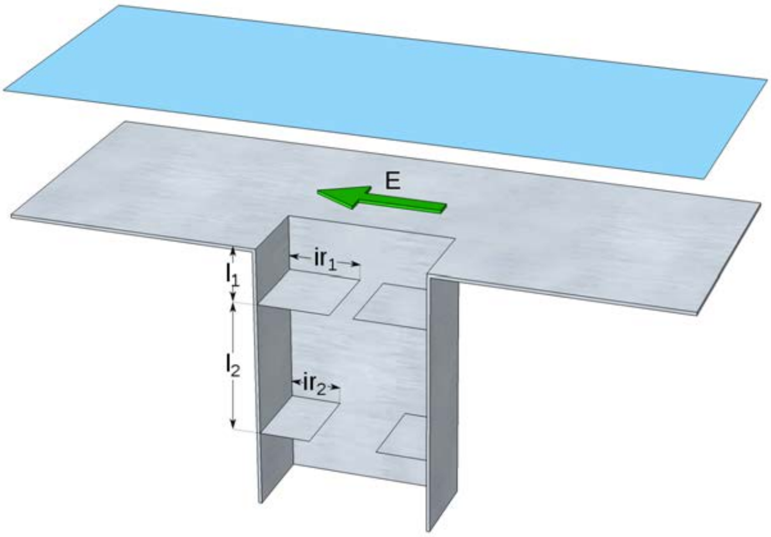

FIGURE 5.7: Section of the feeding network. Two capacitive irises are used for matching purpose inside the waveguide.

Fig. 5.5 represents the radiation pattern evaluated by our analysis tool, where the −20 dB SLL is achieved. The maximum gain is 27 dB. The sparsity achieved through the thinning process allows a reduction of the mutual coupling, with respect to a fully populated array with the same superstrate. The maximum level of mutual coupling is lower than −15 dB. However this value is observed just for three couples of array elements. The mutual coupling is lower than −23 dB for any other pair of elements.

The radiation pattern of the superstate array in Fig. 5.4 has been, then, simulated using the full wave software ANSYS HFSS 16. The sides of the array have been extended by $3\,\lambda_0$ in each direction so that the edge effects can be considered as negligible. The HFSS results are in excellent agreement with the radiation pattern evaluated with our analysis tool, as shown in Fig. 5.6, proving the reliability of the analysis method.

5.1.3.2 Matching Network

The superstrate layer above the array in Fig. 5.4 dramatically increases the reflection coefficient on the source. Therefore, a matching network has been designed. As shown in Fig. 5.7, the network is formed by two capacitive irises, allowing the matching in two frequency points. Referring to the same figure, the parameters of the matching network are $ir_1 = 8.22$ mm, $ir_2 = 5.55$ mm, $l_1 = 5.1$ mm and $l_2 = 27.7$ mm. These values have been evaluated using the procedure described in Section 2.2.3.

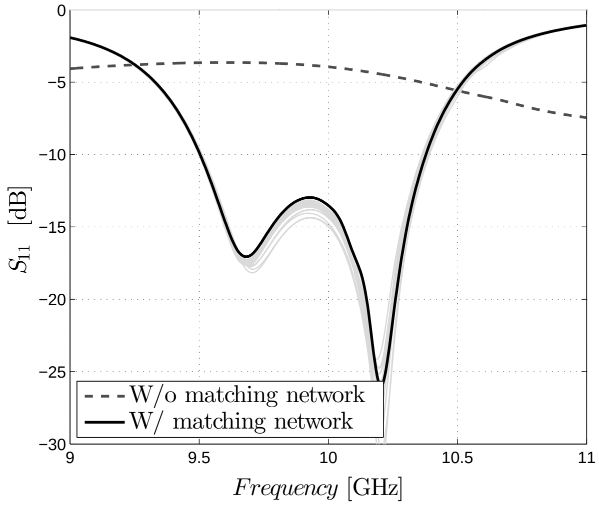

Figure 5.8: Reflection coefficient. Without a matching network (dashed curve) the S_{11} is considerably higher than the acceptable level of -10 dB. After the insertion of the matching network (solid lines, worst case in black), the structure is matched over a 9 % band.

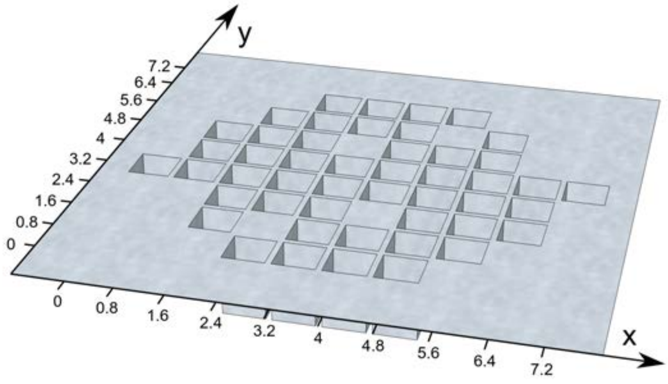

Figure 5.9: Synthesized bare array without gain constraints. It is composed by an arrangement of 68 square waveguides over a ground plane. On the axes, the distance is reported in wavelengths λ_0.

Fig. 5.8 reports the reflection coefficient for all the elements of the array. The curves have been obtained using HFSS. The S_{11} of the structure is lower than -10 dB over a 9% bandwidth.

5.1.3.3 Benchmark Bare Arrays

In order to fully understand the benefits of the superstrate, two bare arrays have been designed using the same starting configuration.

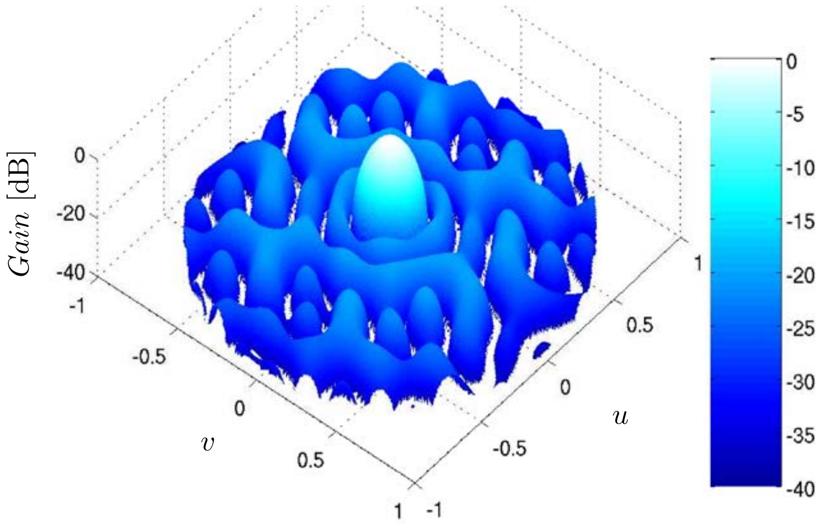

FIGURE 5.10: Radiation pattern of the bare array in Fig. 5.9 (48 elements) at the design frequency (f_0 = 10 GHz) evaluated using our in-house analysis tool. The radiation pattern is represented in the u/v coordinate system, with $u = \sin\theta\cos\phi$ and $v = \sin\theta\sin\phi$.

The first benchmark array is obtained applying the same procedure and specifications as for the superstrate array designed above. The resulting array is shown in Fig. 5.9. The number of sources after the optimization is 48, a number 2.7 times higher than the superstrate case. Despite the higher number of elements, the gain is 1.8 dB lower at the design frequency. The radiation pattern is reported in Fig. 5.10.

A second bare array has been designed with an additional constraint on the broadside gain, allowing the superstrate array to be compared with a benchmark solution characterized by a similar aperture efficiency. A simple but effective method to control the gain in the optimization process is to stop the iterative cycle once a certain gain threshold is reached. In this case, we limit the number of elements removed per iteration. The array resulting from this synthesis process is shown in Fig. 5.11. The number of sources necessary to reach a broadside gain of 26.7 dB is 68, almost four times more than the superstrate case (18 elements). The resulting radiation pattern is reported in Fig. 5.12.

5.1.3.4 Performance Comparison

The thinned arrays represented in Fig. 5.4 (with and without matching network), 5.9 and 5.11 have been analyzed with HFSS, to validate the optimization procedure and

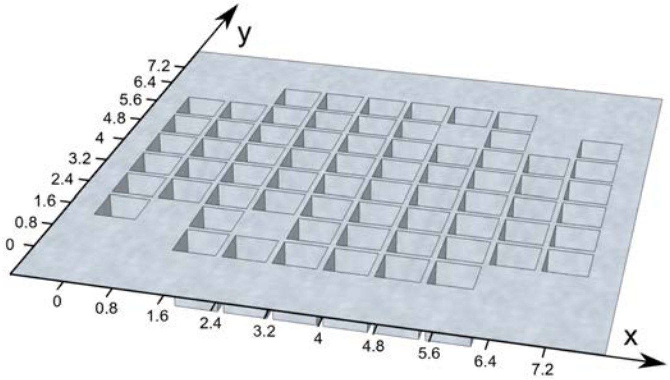

FIGURE 5.11: Synthesized bare array with broadside gain constraint. It is composed by an arrangement of 68 square waveguides over a ground plane. On the axes, the distance is reported in wavelengths λ_0.

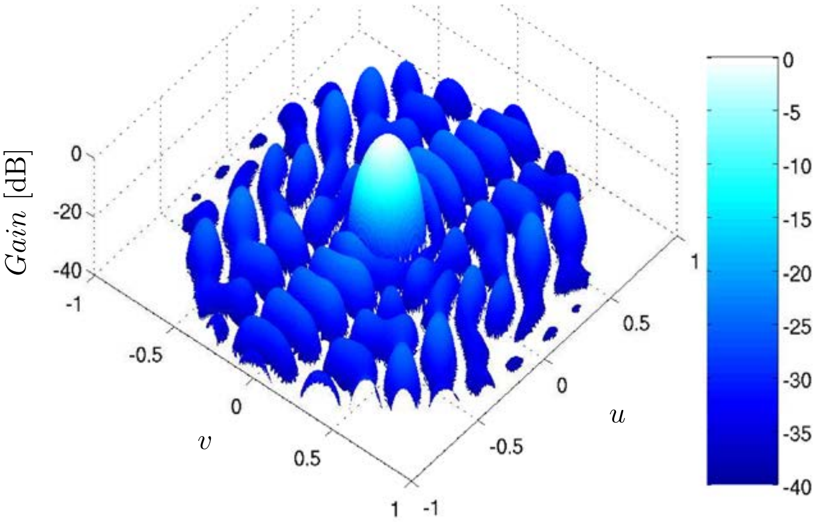

FIGURE 5.12: Radiation pattern of the bare array in Fig. 5.11 (68 elements) at the design frequency ($f_0 = 10$ GHz) evaluated using our in-house analysis tool. The synthesized array produces a radiation pattern fitting the defined mask. The radiation pattern is represented in the u/v coordinate system, with $u = \sin\theta\cos\phi$ and $v = \sin\theta\sin\phi$.

comprehend the effects of the matching network on the radiation pattern in the superstrate case. All simulations have been performed by extending the side of the array by 3 λ_0 in each direction. The field at the edges can be, then, considered almost attenuated in all the four configurations.

The analysis highlights an excellent agreement between predicted radiation pattern and simulation results. The simulated radiation patterns on three different planes ($\phi = 0°, 45°, 90°$) are reported in Fig. 5.13 for the four considered configurations. Fig. 5.13 (a) and (b) refer to the superstrate array (18 elements) without and with matching network. Minor differences are observed between the two patterns. The patterns of the

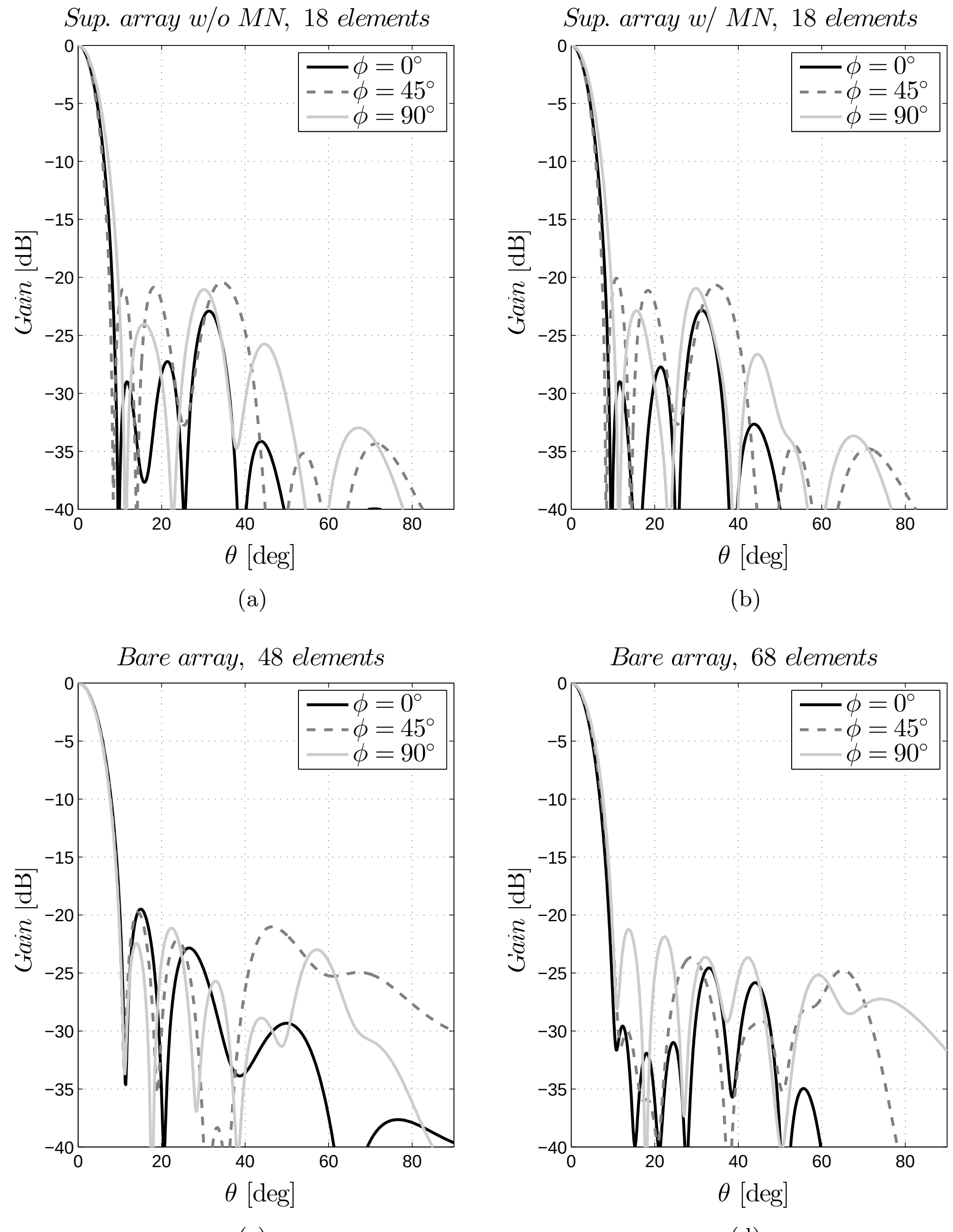

(a) (b)

(c) (d)

FIGURE 5.13: Radiation patterns (HFSS simulations) of the designed arrays on the planes $\phi = 0°, 45°$ and $90°$ at the frequency $f_0 = 10$ GHz: superstrate array without matching network (MN) (a), superstrate array with matching network (b), bare array without gain constraint (c), bare array with gain constraint (d).

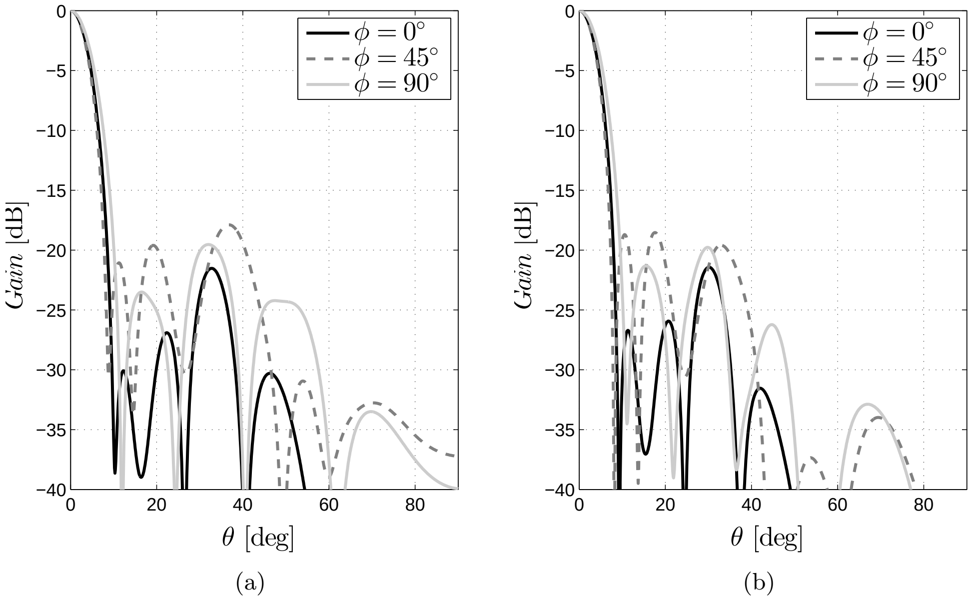

(a)

(b)

FIGURE 5.14: Radiation patterns (HFSS simulations) of the superstrate array with matching network on the planes $\phi = 0°, 45°$ and $90°$ at the edges of the considered frequency band: 9.6 GHz (a), 10.3 GHz (b).

bare array configurations made of 48 and 68 elements are shown in Fig. 5.13 (*c*) and (*d*), respectively.

We also report in Fig. 5.14 the radiation pattern at 9.6 and 10.3 GHz, edges of the considered band, for the superstrate array with matching network. We remark how the SLL remains sufficiently steady in the band.

Fig. 5.15 shows the maximum gain and side lobe level (in the whole two-dimensional space) as a function of frequency. The solid grey curves correspond to the simulation of the superstrate array (18 elements) without matching network, representing the same setup as in the synthesis tool. As we can see, the SLL is −20 dB at $f_0 = 10$ GHz. The broadside gain is 27.3 dB. The aperture efficiency is 70 % considering the physical area as the surface occupied by the radiating apertures ($7.9\,\lambda \times 7.9\lambda$). Then, the matching network has been added to the structure, and the results are represented by the solid black curves. In this case the gain is basically unchanged, and the SLL increases only by 0.6 dB at the design frequency. However, we notice that including the matching network does not have a strong impact on the antenna performance and can be typically overcome by a re-tuning of the antenna parameters. The dashed black curves correspond to the bare array design without gain constraints (48 elements). Despite the considerably

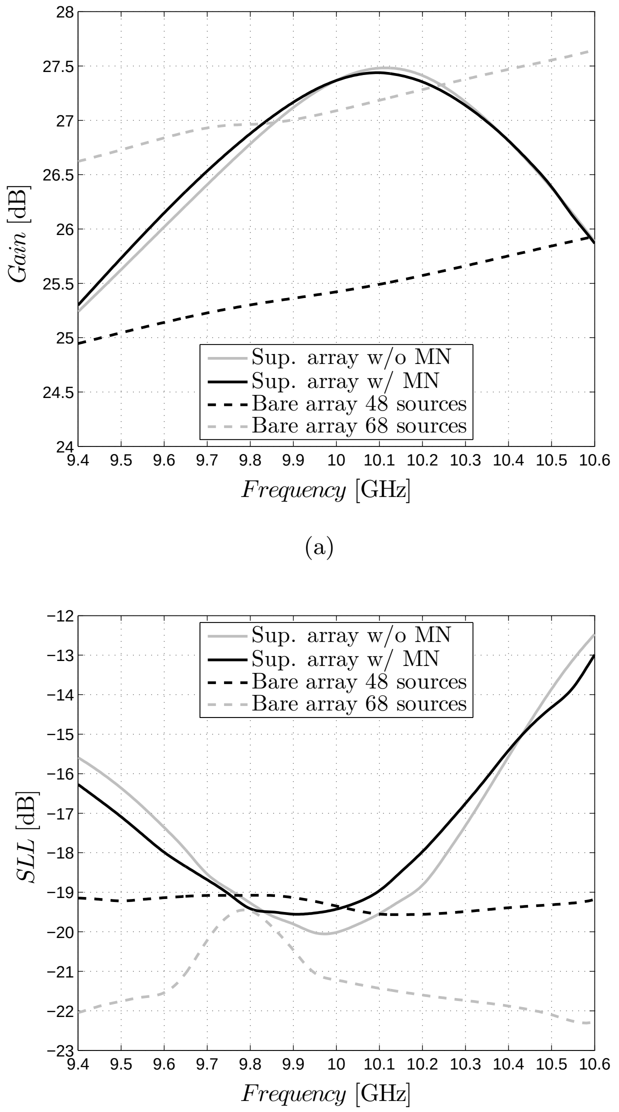

(a)

(b)

FIGURE 5.15: Frequency performance of the designed arrays: gain (a), side lobe level (b). The solid grey curves refer to the superstrate array without matching network (MN). The matching network was added in the drawing of the solid black lines. The dashed lines show the performance of the bare arrays used as benchmark solutions.

higher number of elements, the gain is lower than the one of the superstrate array in a frequency band of 13 %. The SLL is -19.4 dB at the central frequency. In the case of the bare array with gain constraint (68 elements) the final results in terms of SLL and gain are represented by the dashed grey curves. In this case, the gain is slightly lower than the superstrate case in a 5 % band but the number of elements is almost 4 times larger than the superstrate case. The SLL is -21.2 dB at the design frequency ($f_0 = 10$ GHz).

The analysis of the frequency characteristic of the designed thinned array underlines how the dispersive behavior of the superstrate structure influences the SLL, especially in comparison with the bare array case (Fig. 5.15). However, the raise of the side lobes is fairly low and the variation is within 2 dB over a 7 % band (between 9.55 and 10.25 GHz) for the case with the matching network. Also the gain variation is moderately low, 1.5 dB in the considered band, with the benefit of a larger aperture efficiency with a reduced number of sources with respect to the bare case.

5.2 Irregular Superstrate Array

As discussed above, a main design goal for satellite communication antennas for user segment is the reduction of the interference with other sources and, because of this, the side lobe envelope is subject to strict rules [4]. When dealing with antenna arrays, the reduction of the SLL is generally achieved by applying ad-hoc amplitude laws to elements of the array. This is also the case for the antennas in Section 5.1. However, in the case of active antennas with distributed amplification, this approach leads to an inefficient use of the amplifiers, some of the amplifiers not working at their optimal operating point due to either reduced input signals in the case of transmitting antennas or to losses introduced by attenuators in the case of receiving antennas. In the latter case, the noise figure is also affected. In passive antennas, this also means added complexity to the beam forming network design as proper custom power distribution needs to be implemented.

In this section we present an antenna array using isophoric excitations within an irregular superstrate configuration. The amplitude tapering needed to reduce the SLL is here achieved by locally changing the reflectivity of the superstrate, so that each element has

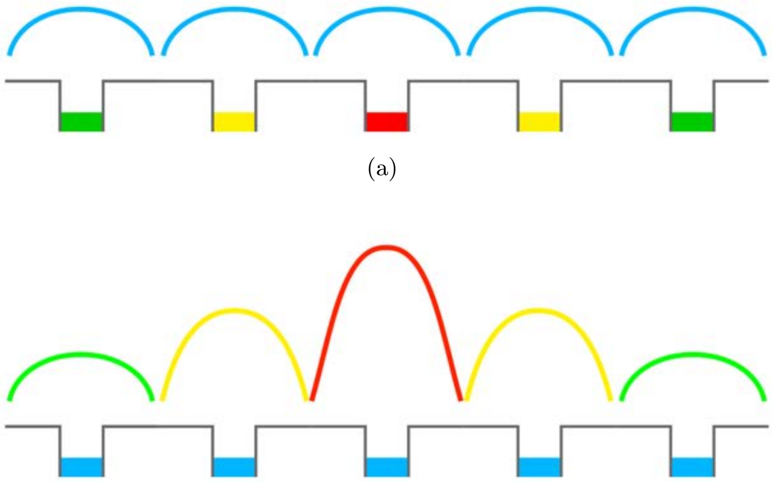

(a)

(b)

FIGURE 5.16: Working principle: instead of using a different excitation amplitude for each element (a), we apply a uniform excitation and we use elements with different gain to recreate the tapering (b).

a different directivity. Using this solution, the amplifiers can work at the same operating point or, in case of receiving antennas, there is no need of attenuators. In the case of passive antennas, this drastically simplifies the beam forming network design as only one component (a balanced power divider/combiner) needs to be optimized and duplicated as many times as needed to produce the equi-amplitude distribution required.

5.2.1 Working Principle

To reduce the interference with the other equipment on the Earth surface, the side lobe envelope must be kept under control. In particular, when dealing with periodicities larger than a wavelength, the grating lobes must be also considered. The reduction of side lobes and grating lobes has to be addressed in separate ways.

Several techniques are employed in literature to control the SLL of antenna arrays. The most widely used consists in the application of a particular amplitude distribution scheme to the elements of the array, such as Taylor or Chebyshev distributions (Fig. 5.16 (a)) [11, 12]. The proposed solution consist in the use of an irregular superstrate configuration: the array elements lay underneath the same superstrate. The latter is divided in tiles and each tile has a different reflectivity. Each array feed “sees” its own tile and radiates with a different gain. This can be seen as a extension of the solution

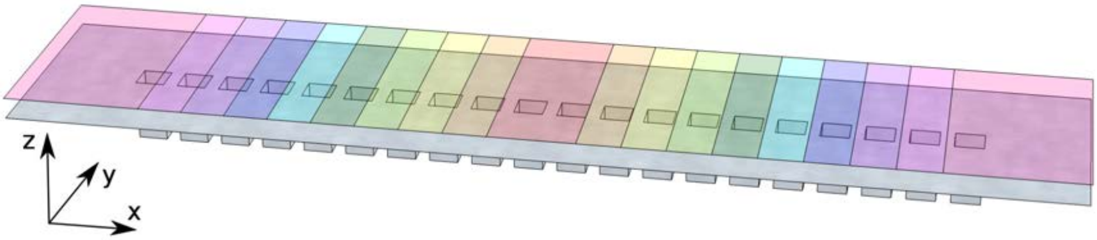

Figure 5.17: Irregular superstrate array of 20 elements in a linear lattice.

described in Section 4.2, except that here the inter-element distance being smaller, the different superstrates are side by side. The innovative idea proposed here is to recreate the amplitude tapering on the gain of the elements to control the SLL of the array. In this way, we move this task from the beam forming network to the superstrate, exciting the array with a uniform amplitude distribution (Fig. 5.16 (b)).

The amplitude tapering does not affect the level of the grating lobes, appearing in the visible space in array antennas with periodicities larger than a wavelength. Dealing with antennas for user segment, a high level of grating lobe can not be tolerated, as a main design goal is the minimization of the interference. General techniques used to reduce the level of the grating lobes break the array periodicity. This is the case of the sparse arrays [11, 12, 16]. The drawback of sparse array is the inefficient use of the available surface and the corresponding poor aperture efficiency. In the present work, we use the element pattern to filter the grating lobe, using the same principle as in Section 3.1.2. In particular we exploit the roll-off figure and the reduction of the SLL at element level to reduce the grating lobes of the array.

The structure of the proposed array is shown in Fig. 5.17. Square waveguide apertures are used as feed. Each one of them is underneath a different superstrate tile, represented in the figure by a different color, leading to a different element gain. Instead of an amplitude tapering on the sources, the array uses a gain tapering through the irregular superstrate, reducing the SLL.

5.2.2 Design Procedure

The novelty of the proposed structure is the reduction of the SLL achieved through the use of an irregular superstrate. We describe here the design procedure, considering a linear array of $N = 20$ elements. The procedure holds using different configurations or

Table 5.2: Taylor amplitude distribution for a linear array of 20 elements numbered from one side to the other.

Element #	1	2	3	4	5	6	7	8	9	10
Excitation [dB]	0	0.3	1	1.8	2.7	3.5	4.3	4.9	5.3	5.5

Element #	11	12	13	14	15	16	17	18	19	20
Excitation [dB]	5.5	5.3	4.9	4.3	3.5	2.7	1.8	1	0.3	0

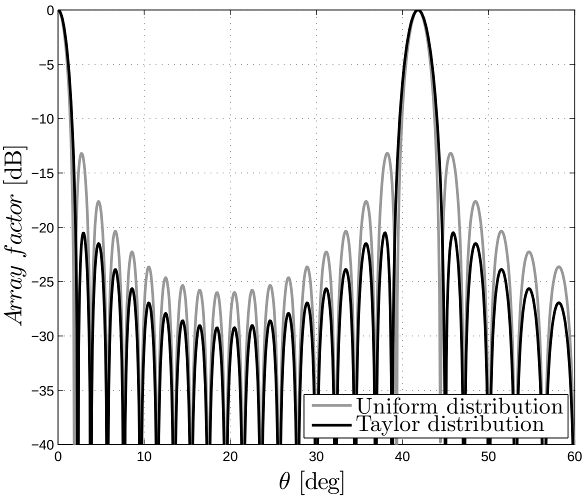

Figure 5.18: Array factor for the linear array of 20 elements fed with a uniform and Taylor amplitude distribution.

number of elements. The elements of the considered array are regularly spaced and the interelement distance is equal to $1.5\,\lambda_0$ (with λ_0 the wavelength at the design frequency f_0). This distance has been chosen in light of a trade-off between the position of the grating lobe and the mutual coupling: to correctly filter the grating lobe, it must be sufficiently distant from broadside. On the other hand, the spacing must be sufficiently large to have an acceptable level of mutual coupling. The goal is to use the irregular superstrate to get a SLL lower than −20 dB.

The design procedure begins with the definition of an equivalent excitation law. As shown in the following, the excitation law is not used here to determine the amount of power to feed the elements of the array, but to choose the parameters of the superstrate. For this example we choose a Taylor amplitude distribution [11]. The corresponding excitation vector is reported in Table 5.2. The dynamic of the excitation, i.e. the ratio between the highest and lowest amplitude, is 5.5 dB. The array factor in Fig. 5.18 shows that the requested $SLL \leq -20$ dB is obtained.

Table 5.3: Gain of the elements associated to the Taylor amplitude distribution in Table 5.2 and reactance value needed to retrieve it.

Element #	1	2	3	4	5	6	7	8	9	10
Gain [dB]	12	12.3	13	13.8	14.7	15.5	16.3	16.9	17.3	17.5
Reactance [$-\Omega$]	1088	742	491	319	242	176	133	111	100	92

Element #	11	12	13	14	15	16	17	18	19	20
Gain [dB]	17.5	17.3	16.9	16.3	15.5	14.7	13.8	13	12.3	12
Reactance [$-\Omega$]	92	100	111	133	176	242	319	491	742	1088

At this point we move the problem from the excitation to the superstrate. We use here capacitive impedance sheets as a superstrate, easy to manufacture in PCB (printed circuit board) technology. The conclusions hold using different kind of superstrates. As an additional constraint, we set the height of the superstrate to be the same for all its tiles. This expedient helps the manufacturing process and prevents undesired edge effects. The height chosen to design this array is equal to $0.53\,\lambda_0$, allowing the elements to reach fairly high directivities even in the embedded configuration. In the following, we consider waveguide apertures with the side equal to λ_0 as feeds. The values of the reactive sheets are, now, the parameter allowing us to tune the gain of each element.

The idea behind the design procedure is to relate the directivity of the elements to the equivalent excitation vector. Following the notation used in Chapter 2, the directivity of an array for a fixed ϕ can be evaluated as:

$$\mathbf{D}(\theta) = \frac{4\pi}{2\eta_0}\frac{|\mathbf{E}^a(\theta)|^2}{P_{in}}, \tag{5.5}$$

where $|\mathbf{E}^a|$ is the field radiated by the array. Its expression is:

$$\mathbf{E}^a(\theta) = \sum_{n=1}^{N} \mathbf{E}^e_n(\theta)\cdot a_n, \tag{5.6}$$

where $\mathbf{E}^e_n$ is the element pattern of the n^{th} element and a_n its excitation. In the classical designs analyzed in literature, the weight of each array element is defined by the term a_n. In the irregular superstrate array case, instead, we consider a uniform excitation and we change, with the superstrate, the directivity of each element. In this case, the coefficients a_n assume the same value a_0 for all the elements of the array. The field radiated by the array is:

$$\mathbf{E}^a(\theta) = a_0 \cdot \sum_{n=1}^{N} \mathbf{E}_n^e(\theta), \tag{5.7}$$

and its directivity is:

$$\mathbf{D}(\theta) = \frac{4\pi|a_0|^2}{2\eta_0} \frac{\left|\sum\limits_{n=1}^{N} \mathbf{E}_n^e(\theta)\right|^2}{P_{in}}. \tag{5.8}$$

If all the elements are matched and the mutual coupling sufficiently low, the accepted power is the same for all the elements of the array. The total accepted power is:

$$P_{in} = N \cdot P_0, \tag{5.9}$$

Where P_0 is the accepted power for each element of the array. The directivity becomes:

$$\mathbf{D}(\theta) = \frac{4\pi|a_0|^2}{2\eta_0} \frac{\left|\sum\limits_{n=1}^{N} \mathbf{E}_n^e(\theta)\right|^2}{N \cdot P_0} \leq \frac{4\pi|a_0|^2}{2\eta_0} \frac{\sum\limits_{n=1}^{N} |\mathbf{E}_n^e(\theta)|^2}{N \cdot P_0} = \frac{1}{N} \sum_{n=1}^{N} \mathbf{D}_n^e(\theta), \tag{5.10}$$

where $\mathbf{D}_n^e$ is the directivity of the n^{th} element when all the other elements are connected to matched loads. The directivity of the array can be modified tuning the directivities, or the gain, of the elements. Note that, under the considered circumstance and for loss-less structures, we can indifferently talk of gain and directivity.

From a practical point of view, the procedure consists in selecting the element gain proportional to the corresponding power in the equivalent excitation vector $\mathbf{w}$. This relation can be written as:

$$\frac{|w_1|^2}{|w_n|^2} \equiv \frac{G_1}{G_n}, \text{ for } 2 \leq n \leq N. \tag{5.11}$$

In such a way, we know the relation between gain of the elements of the array, but we need to define the absolute values.

Since the ratio between the elements is defined, we need to choose the absolute gain for a single element to derive the other ones. In this case, we set the gain of the first source G_1. It is worth noting that this value determines the bandwidth and the grating lobe rejection, as it affects gain associated to all the array elements. If G_1 is too low, the roll-off figures of the element patterns will not be sufficient to reduce the grating lobe below the desired threshold, as clear from the analysis in Section 4.1. For this example we set the first source to have a broadside gain equal to 12 dB. Table 5.3 shows the derived gain for the other elements of the array.

HFSS is used to tune the values of the impedance sheet tiles. In fact, the analysis tool in Chapter 2 can not be used in this irregular environment for the evaluation of the radiation pattern. Note that considering a superstrate with different impedance tiles is not equivalent to truncate the superstrate as we did in Section 4.2, since each element radiates part of the energy in the neighbor tiles depending on the interelement spacing.

As shown in Fig. 5.17, the simulated structure consists of a linear array of 20 square waveguide apertures along the x-axis on a ground plane, underneath the irregular superstrate. The waveguides have a side equal to λ_0 and they are fed with a single TE_{10} mode in y-direction. The interelement distance is $1.5\,\lambda_0$. The irregular superstrate is formed by 20 impedance tiles, with a length of $1.5\,\lambda_0$ on the x-axis, centered on the apertures. Ground plane and superstrate are extended for a length of $4\,\lambda_0$ beyond the waveguide array in both x- and y-directions. An impedance matching is needed to correctly evaluate the final gain level of any single element in embedded configuration. Since each element "sees" a different superstrate, it needs a different matching network. The matching is performed using a single capacitive iris evaluating its parameters with the method described in Section 2.2.3.

The tuning of the impedances needs the generation of several different configurations in terms of impedance sheets and matching networks. For this reason, the HFSS user interface results impractical. HFSS-MATLAB-API [75] has been used and expanded to interface MATLAB with HFSS. In this way, MATLAB is used to select the parameters of the structure, while HFSS is employed as the solver.

The final value of reactances found to synthesize the desired gain at element level is reported in Table 5.3.

The radiation pattern of the array on the plane of the array (H-plane) is shown in Fig. 5.19 at the design frequency. All the elements are fed with the same excitation, but the SLL is close to -20 dB. The small difference compared to the predicted result is given by the fluctuations of the radiation pattern of the elements in the position of the first lobe. Also the grating lobe result filtered using this method.

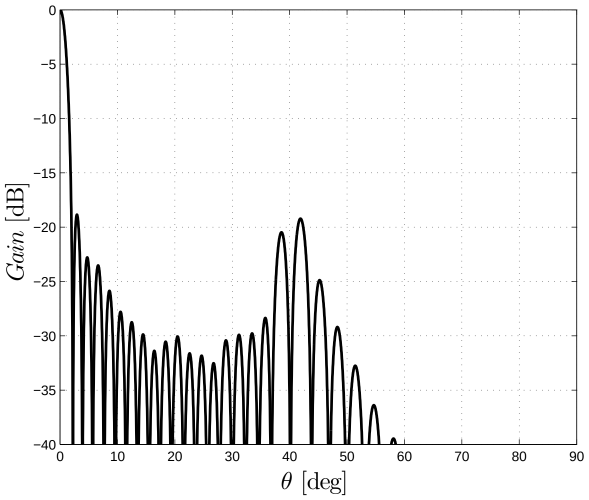

FIGURE 5.19: Simulated radiation pattern on the H-plane at the central frequency of the irregular superstrate array of 20 elements fed with a uniform amplitude distribution.

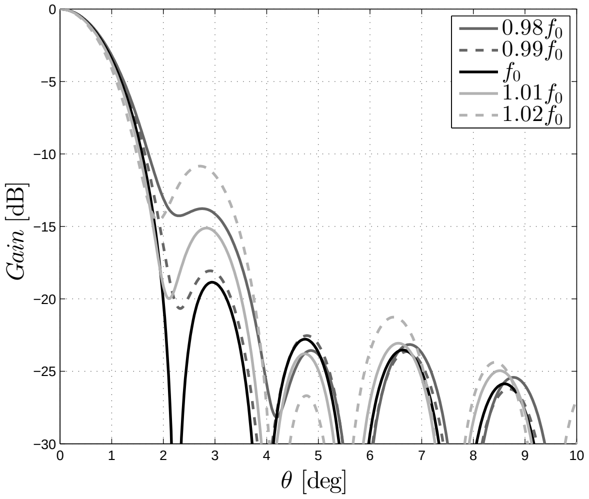

FIGURE 5.20: Frequency performance (HFSS simulation) of the irregular superstrate array of 20 elements fed with a uniform amplitude distribution (H-plane).

The drawbacks of this solution arise looking at the frequency performance, reported in Fig. 5.20. The SLL increases of almost 10 dB in a 4 % band. The bandwidth limitation will be addressed in the following.

5.2.3 Performance Improvement

In Section 5.2.2 we demonstrate that it is possible to reduce the SLL of a linear array using the irregular superstrate. However, the structure suffers from important limitations in terms of bandwidth. In fact, the SLL quickly increases changing the working frequency. To mitigate the dispersive behavior, the ratios between the gain of the elements must be preserved along the band.

Two are the main parameters affecting the strong dispersion of the structure. The first parameter is the dynamic of the equivalent excitation associated to the superstrate. Having large dynamics, as in this case, let the radiation pattern of the different elements varying differently with the frequency. On the other hand, a certain dynamic is needed to bring the SLL from the level of the uniform excitation/regular lattice (-13.2 dB [11]) to the desired value and to reach a lower SLL we need a larger dynamic. Targeting a fixed level of side lobes, the dynamic can be reduced having a lower SLL as a starting point or using a less demanding equivalent excitation law. The second parameter affecting the dispersion is the gain of the element chosen as starting point. This gain must be selected sufficiently high to filter the grating lobe [30], but an high gain increases the dispersion.

In this section we present the most effective paths explored to reduce the dispersion of the irregular superstrate array.

5.2.3.1 Excitation Law

As shown in Section 5.2.2, a key point in the design of the irregular superstrate array is the definition of an equivalent excitation law. The latter, is not applied to the sources but is used to choose the impedance of each superstrate tile. In particular, for a given SLL, the excitation law determines the dynamic of the excitation. A narrower dynamic would help to decrease the dispersion of the structure.

The MATLAB convex optimization toolbox CVX [74] is used for this scope. The excitation law is found imposing a mask to the array factor $\mathbf{AF}(\theta) = \sum_{n=1}^{N} w_n \, e^{jk_0 x_n \sin\theta}$, where N is the number of elements of the array, w_n is the excitation amplitude of the n^{th} element and x_n its position. We consider the main lobe pointing at $\theta_0 = 0$, while a maximum side lobe level $\rho(\theta)$ is allowed over the angular region T on the plane of the

TABLE 5.4: Taylor and CVX amplitude distributions for a linear array of 20 elements numbered from the side to the center.

Element #	1	2	3	4	5	6	7	8	9	10
Taylor excitation [dB]	0	0.3	1	1.8	2.7	3.5	4.3	4.9	5.3	5.5
CVX excitation [dB]	0	0	0	0	0	2.5	2.5	3.7	3.7	3.7

array. These constraints can be expressed as:

$$\text{Mask}\begin{cases}\mathbf{AF}(\theta_0) = 1\\ |\mathbf{AF}(\theta)| \leq \rho(\theta), \forall(\theta) \in T\end{cases}. \tag{5.12}$$

In this case, the goal of the optimization is to minimize the dynamic of the excitation, described in the excitation vector $\boldsymbol{w}$. The optimization problem can be expressed in a mathematical form as follows:

$$\min_{\boldsymbol{w}}\{\max(\boldsymbol{w}) - \min(\boldsymbol{w})\} \text{ subject to Mask,} \tag{5.13}$$

Let us consider, as example, the same linear array of 20 sources with interelement distance equal to $1.5\,\lambda_0$ analyzed in Section 5.2.2. Asking for a SLL $\rho \leq -20$ dB in the angular region between the main beam and the first grating lobe, CVX evaluates an excitation law with a dynamic of 3.7 dB, 1.8 dB lower than the one of the Taylor distribution. The values of the excitation are reported in Table 5.4. Note that the excitation is symmetrical with respect to the x-axis and we report just the values from the side to the center of the array.

The comparison between the array factors computed with Taylor and CVX distributions is shown in Fig. 5.21. The pattern evaluated with CVX respects the radiation mask and the requested SLL is obtained with a sensible reduction in the dynamic of the excitation. Also the beamwidth remains the same for the two configurations.

5.2.3.2 Element Spacing

Another way to reduce the dynamic and the dispersion of the structure, consists in using an irregular array lattice.

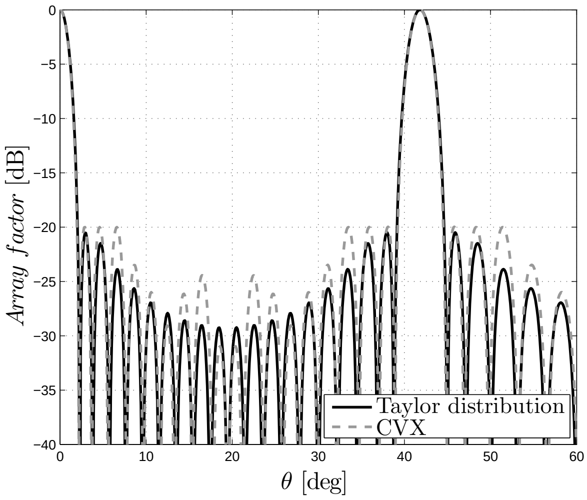

Figure 5.21: Array factor for the linear array of 20 elements fed with Taylor and CVX-derived amplitude distribution.

As we have shown above, the SLL of a regular array with uniform illumination is equal to −13.2 dB [11]. A certain excitation dynamic is needed to decrease the SLL to a desired value. Having a more advantageous starting point would help to reduce the dynamic. A way to decrease the SLL of the starting point is the use of an irregular lattice.

The idea is to consider an array of the same length as a reference one but with an irregular, or sparse, array lattice. In this way, the starting point might have a lower SLL and grating lobe level [15–17]. A side effect is given by the enhanced coupling due to the fact that some of the elements of the array will be put closer to each other, as remarked in Secion 4.1.1.

This method helps to reach the goal of increasing the band of the irregular superstrate array. However, we do not use it in the following to avoid the mixture of too many aspects in the design.

5.2.3.3 Beam-Forming Network

As explained above, one of the needs behind the idea of the irregular superstrate array is to avoid complicated power distributions, simplifying the BFN. In this way, the BFN might be realized using simple power dividers. However, the introduction of some irregularities in the BFN might help to reduce the dynamic associated to the superstrate.

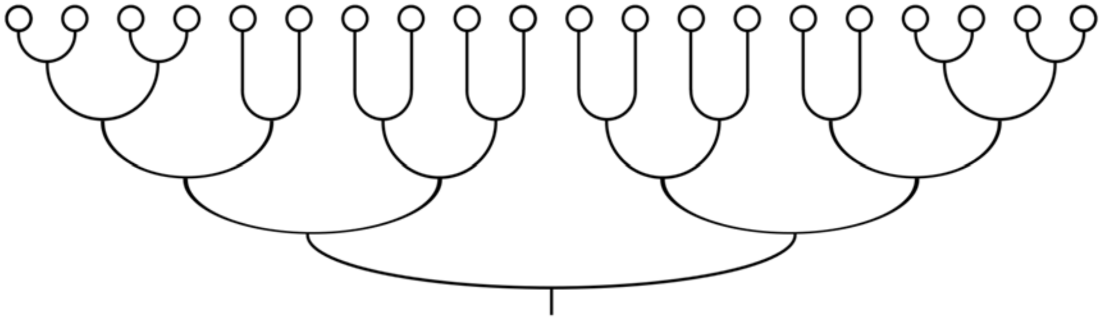

FIGURE 5.22: BFN made of 3 dB power splitters for the linear array of 20 elements.

TABLE 5.5: Amplitude distributions for a linear array of 20 elements with the BFN in Fig. 5.22.

Element #	1	2	3	4	5	6	7	8	9	10
BFN distribution [dB]	0	0	0	0	3	3	3	3	3	3
CVX excitation [dB]	0.2	0	0	0	0	0	1.5	1.5	1.5	1.5
Resulting distribution [dB]	0.2	0	0	0	3	3	4.5	4.5	4.5	4.5

A way to reach this goal without overcomplicating the BFN consists in the appropriate redistribution of the power dividers.

Instead of feeding all the elements with the same power, we create a network of simple 3 dB power splitters to feed the elements at the side of the array with a weaker amount of power. This approach recreates an approximate tapered distribution, without complicating the BFN. The result is a more convenient starting point to define the equivalent excitation law, lightening the duty of the superstrate.

Considering the same linear array of 20 elements studied above, a possible layout for a BFN introducing some tapering is illustrated in Fig. 5.22: the four elements at both sides of the array are fed through an additional stage of power dividers and they receive half of the power than the elements at the center.

CVX has been used to find the excitation law to apply to get the $SLL \leq -20$ dB. It is reported in Table 5.5. The dynamic of the excitation addressed to the superstrate has been reduced from 3.7 to 1.5 dB.

Figure 5.23 shows the array factor before and after the application of the excitation law. Using the additional stage of power dividers, decreases the SLL of the starting point to -16.6 dB. A reduced dynamic associated to the superstrate is, then, needed to decrease the SLL below the desired threshold.

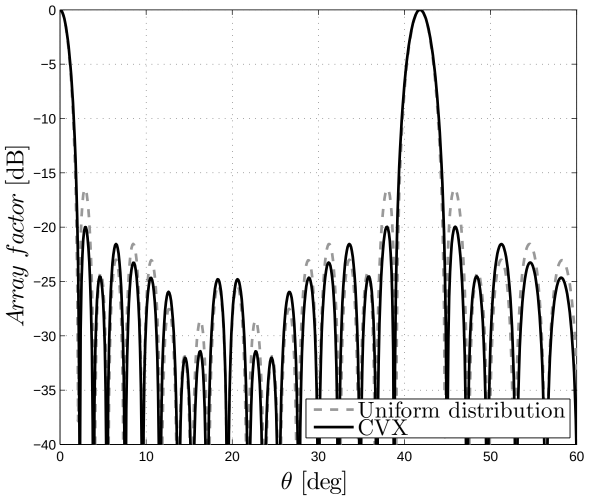

FIGURE 5.23: Array factor for the linear array of 20 elements with the BFN in Fig. 5.22.

TABLE 5.6: Parameters for the irregular superstrate array of 20 elements numbered from the side to the center.

Element #	1	2	3	4	5	6	7	8	9	10
Gain [dB]	15	13.9	13.9	13.9	13.9	13.9	16.1	16.1	16.1	16.1
Reactance [-Ω]	258	315	320	319	311	290	147	135	133	135

5.2.4 Irregular Superstrate Array Design

A new irregular superstrate array has been designed. The requirements are the same as in Section 5.2.2, with a linear array of 20 elements, interelement distance equal to 1.5 λ_0 and a requested SLL lower than -20 dB. Also in this case we use square waveguide apertures as feeds, with the lateral size equal to λ_0. The structure is the same as in Fig. 5.17.

The array is designed for the band 19.7-20.2 GHz, typically used in the space-to-Earth link [76].

For this design, the BFN presented in Section 5.2.3.3 is used. To compensate the residual dispersion, we choose a $SLL \leq -22.5$ dB as threshold for the definition of the equivalent excitation law, obtained using CVX (Section 5.2.3.1). Note that a trade-off is needed for the choice of the threshold, as a more demanding value would lead to an increased excitation dynamic.

The gain value requested to the least directive element has been chosen *a posteriori*, selecting the lowest value able to filter the grating lobe. This value is equal to 13.9 dB with the chosen distribution. As explained in Section 5.2.2, the gain needed from each element is associated to the equivalent amplitude distribution. These values are reported in Table 5.6. In the same table, we show the value of reactance associated to each superstrate tile to retrieve the respective gain. The impedance values have been evaluated using HFSS simulations with the same setup described in Section 5.2.2. The height of the superstrate has been tuned to fulfill the requirements, and it is equal to 8.02 mm (0.53 λ_0).

The simulated radiation pattern on the plane of the array (H-plane) is shown in Fig. 5.24. The side lobes and grating lobe remain below the threshold in the whole considered band. Note that the radiation pattern remains below -40 dB in the angular region $\theta > 50°$ and is not shown in the figure.

A benchmark bare array has been designed to compare the performance of the irregular superstrate array and it is shown in Fig. 5.25. The interelement distance and the overall dimension is the same as for the irregular superstrate array. The feeds are square waveguide apertures with side equal to $1.5\,\lambda_0$, as the interelement distance, fed with a single TE_{10} mode. In this case, a Taylor amplitude tapering has been applied to the sources to get the $SLL \leq -20$ dB. The radiation pattern is reported in Fig. 5.26. The requested SLL has been reached, but the grating lobe is 9 dB higher.

As shown in Fig. 5.27, the gain of the irregular superstrate array is ~ 1 dB higher that the classic benchmark solution in the considered band.

To have a clearer view of the electromagnetic characteristics of the proposed structure, we shown in Fig. 5.28 the matching of the array elements. The reflection coefficient is lower than -10 dB in the considered band for all of them. Also, the mutual coupling between neighbor elements is reported in Fig. 5.29. The elements at the center of the array are the most directive ones and they present the highest level of mutual coupling, about -18 dB.

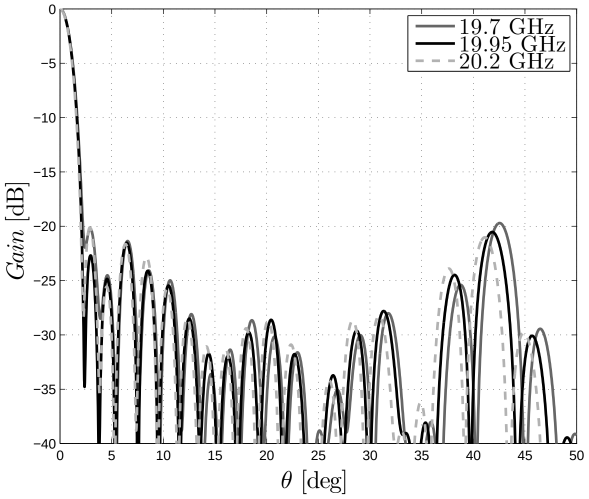

(a)

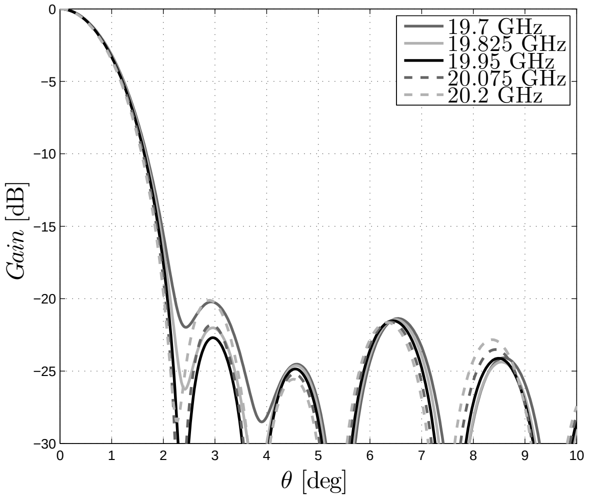

(b)

Figure 5.24: HFSS simulation of the linear irregular superstrate array of 20 elements in a 2.5 % band: up to 50° (a) and an enlargement up to 10° (b).

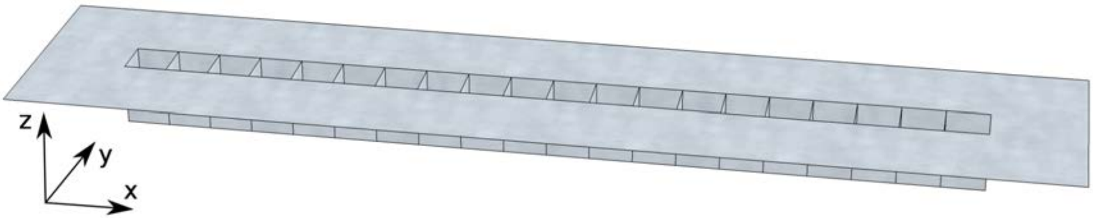

Figure 5.25: Benchmark aperture array of 20 elements.

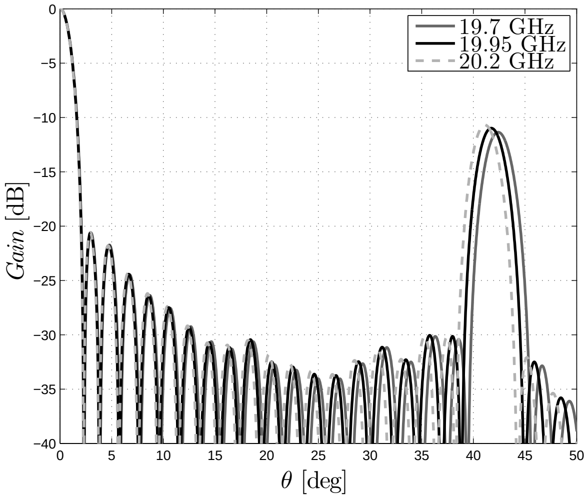

FIGURE 5.26: HFSS simulation of the benchmark array of 20 elements in a 2.5 % band.

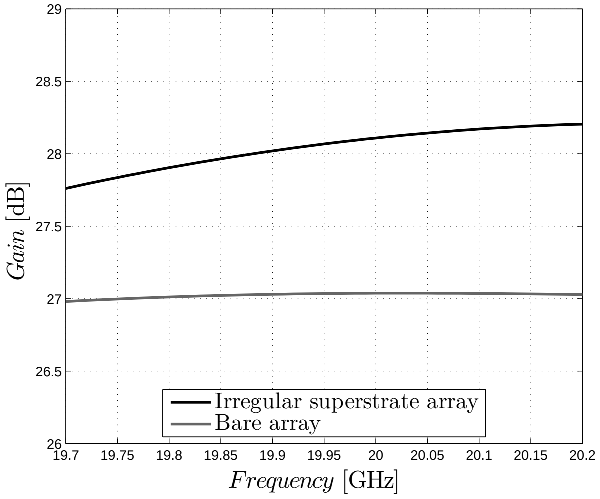

FIGURE 5.27: Broadside gain of irregular superstrate and benchmark arrays.

5.3 Summary

In this chapter we presented novel techniques to control and reduce the SLL of LWA arrays, necessary to use this solution for ground applications.

In the first section, a synthesis method for thinned LWA array has been presented. The optimization procedure is based on the ℓ_1 minimization of the excitation vector. The goal is to minimize the number of sources keeping the radiated field inside a radiation mask. The effects of the mutual coupling are considered during the optimization. The use of the superstrate provides a reduction in the number of elements of the array. As

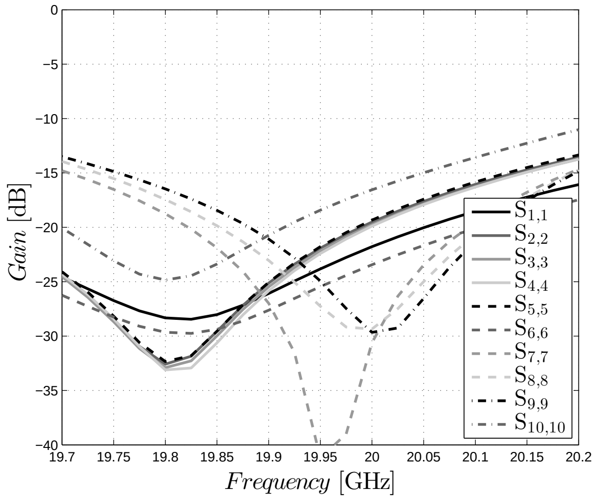

FIGURE 5.28: Matching of the array elements.

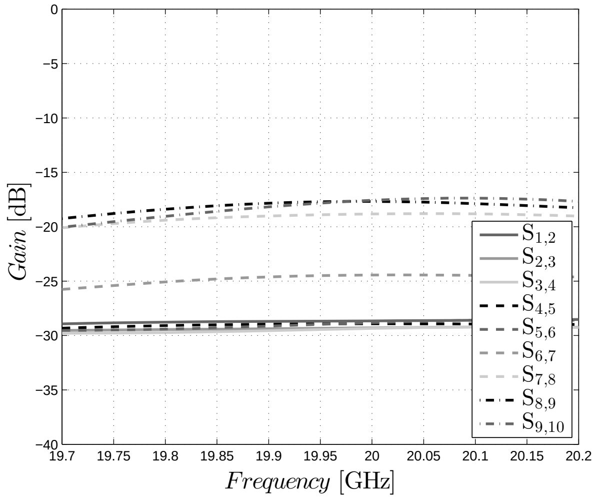

FIGURE 5.29: Mutual coupling between neighbor elements.

shown in the example, a superstrate array working on a 7 % band with the same gain and SLL of a benchmark array can be designed reducing the elements of a factor 4.

In the second section we proposed the irregular superstrate array, a novel configuration where the superstrate is divided in tiles with different reflectivity. With this method, we can create an equivalent amplitude tapering using the different gain at element level, feeding the elements with a uniform excitation. A linear array of 20 elements with $SLL \leq -20$ dB and a gain 1 dB higher than a benchmark bare solution has been designed in K-band, exhibiting the filtering performance in the desired 2.5 % band. The prototype of this structure will be shortly realized and tested at ESA/ESTEC.

Chapter 6

Conclusions

This thesis has dealt with the possibility to enhance the performance of phased arrays antennas for space application by using superstrate-like leaky-wave structures. The structures considered are arrays of apertures on a ground plane, exciting leaky-wave modes between a partially reflective superstrate and the ground plane itself.

This Ph.D. topic has been challenging from several points of view. Leaky-wave structures are well-known antennas thanks to their capability of gain enhancement and pattern shaping. However, these advantages come with an inherently narrow-band behavior ($1 \sim 8\,\%$ band) and an increased level of mutual coupling (up to -10 dB) in array environment. These aspects are very challenging design limitations especially for space communication applications, where the antenna solutions typically employed have high aperture efficiency (higher than $80\,\%$) and high-end performance. In addition, space applications may require antenna with high gain (> 40 dB) and, therefore, electrically large radiating apertures.

It has been clear since the beginning that studying these electrically large structures using commercial simulators was not a convenient solution. On the other hand, approximations at array factor level for phased array designs incorporating leaky-wave phenomena could not be applied due to the strong impact of the mutual coupling among the elements. In addition, periodic boundary conditions can not be enforced when irregular lattices are considered, as in the framework of this thesis. The first part of the doctorate studies has been devoted to the development of an in-house tool to analyze these structures. This analysis tool is based on a Green's function spectral approach and has been extensively illustrated in Chapter 2. It is capable to evaluate the radiation characteristics of leaky-wave antenna arrays with the least level of approximation. Most of all, it can evaluate in a fast and reliable way the scattering parameter of the structure, so that the real embedded configuration can be studied. The main achievement obtained through this code has been the ability to generate and characterize a huge amount of superstrate structures in a short time, opening the way to the development of synthesis procedures for leaky-wave-based phased arrays.

One of the first example of leaky-wave antenna designed exploiting the capabilities of the analysis tool is presented in Chapter 3. The tool has been used to develop a universal synthesis method for the radiation pattern of leaky-wave antennas. Giving as input a mathematical function, the synthesis tool returns the physical parameters of the antenna structure with the required radiation pattern. The most interesting structure synthesized for space applications is an antenna radiating a flat-topped radiation pattern. A demonstrator in X-band working in a 7 % bandwidth has been manufactured and tested at IETR, showing an excellent agreement with the predicted results. The interest behind this kind of radiation pattern is its adoption as element pattern in phased arrays for geostationary satellites minimizing the scan losses and suppressing the grating lobes due to the large periodicity generally adopted for such applications. In the same chapter, clearly devoted to the element pattern synthesis, a second novel antenna design has been presented. It consists of a planar leaky-wave antenna using a truncated superstrate to generate a cosecant-squared radiation pattern. The extreme simplicity of the antenna makes it a very attractive solution. Also in this case, a design approach is proposed.

In Chapter 4 we moved to the design of antenna arrays for space applications. In particular, the gain enhancement in the array configuration and the possibility to reduce the number of elements of classical aperture antenna arrays are studied using the analysis tool developed in Chapter 2. The first part of the chapter is focused on the design of phased arrays for space and user segments. Different requirements in terms of gain, array periodicity, and bandwidth lead to significantly different results, due to the mutual coupling introduced by the superstrate. A parametric study on the reflectivity of the superstrate and the interelement distance has been performed to understand and quantify the effects on the coupling and on the bandwidth, helping us in the design of the arrays for satellite link. The parametric study clearly shows that leaky-wave-based phased arrays are not always the best solution for the space segment. In fact, the combined requirements of broad bands ($8 \sim 14\,\%$), large array periodicities ($3 \sim 4\ \lambda$) and high aperture efficiencies ($> 80\,\%$) make the leaky-wave technology difficult to handle. Conversely, in the user segment the superstrate structure can be fully exploited, because of the shorter periodicities and the narrower frequency bands of about $1 \sim 3\,\%$. In particular, it is shown that leaky-based structure with gain comparable with classical solution can be achieved in $8\,\%$ bandwidth with a reduction of the number of elements of the array. In the second part of the chapter, we presented the patch-superstrate antenna, consisting of a Fabry-Perot cavity with a truncated superstrate able to enlarge the bandwidth of regular leaky-wave structures. This novel configuration has been used for the design of a dual-band array in Ka- and K-band for on-board satellite applications. Comparing it to a classical dual-band horn array with the same periodicity and number of element, the gain of the patch-superstrate array is $1 \sim 2$ dB higher in the most part of the considered bands.

The strength of the leaky-wave arrays is fully exploited in the two antenna designs presented in Chapter 5. In the first part of the chapter, the analysis tool developed in Chapter 2 is used for the development of a synthesis procedure for thinned leaky-wave arrays. The goal of the procedure is the minimization of the array elements maintaining the radiated field inside a radiation mask, defined through the beamwidth and the accepted side lobe level. Under those circumstances, the generated leaky-wave solutions present a terrific reduction of the array elements, keeping gain levels comparable to the classical aperture solutions. In the example, we designed a leaky-wave-based thinned array working in a $7\,\%$ band with a side lobe level lower than -20 dB. Using the superstrate, we managed to reduce the number of array elements of a factor 4, with respect to a classical aperture array solution. In the second part of the chapter, a novel configuration, the irregular superstrate array, has been presented. The superstrate is divided in tiles with different reflectivities and each element of the array presents a different gain. This peculiarity is used to recreate a power tapering on the superstrate able to control the side lobe level of the array, while the elements are fed with an uniform amplitude distribution. A prototype demonstrator in K-band will be shortly manufactured and tested at ESA/ESTEC.

Future Developments

In this thesis we focused on the performance enhancement of phased arrays for satellite applications using superstrate-like leaky-wave antennas. Several interesting solutions has been studied, leaving space for improvement for both space and user segments.

We proved in Chapter 3 that the shaping capabilities of leaky-waves can be used to enhance the performance of on-board satellite antennas. The benefits in terms of scan losses and grating lobe rejection are undeniable, but to satisfy the requirements in terms of aperture efficiency, the periodicity of the array must not be higher than $1.5\,\lambda$. As clear from the analysis in Chapter 4, some of the constraints between bandwidth, periodicity and aperture efficiency should be relaxed to fully exploit the potential of this solution.

The specification for user segment, instead, allow the complete exploitation of the leaky-wave technology. The reduced bandwidth needed for this application is the key point. Besides the unsurprising gain enhancement shown in Chapter 4, the shaping of the radiation pattern is, again, the most interesting feature. The superstrate structure helps us to modify the radiation characteristics at element and array level, leading to novel array configurations. High aperture efficiencies can be reached in narrow-bands $(1 \sim 3\,\%)$ and small array periodicities $(1 \sim 2\ \lambda)$.

The performance of the leaky-wave technology are exploited in the design of the thinned array in Chapter 5. Using the tools of this method, the leaky-wave arrays can be finally compared to classical solutions having the same radiation properties in terms of gain, SLL and beamwidth. Further improvements are achievable using irregular array element disposition. The resulting sparse array might reduce the side lobes and/or the number of elements of the array. The procedures presented in literature for the design of sparse arrays might be extended using the analysis tool developed in Chapter 2, as we did for the thinned array case.

Also the irregular superstrate array presented in Chapter 5 makes use of the benefits derived from the user segment specifications. This array is able to control the side lobes and grating lobes using a superstrate with different impedance tiles. The array concept might pave the way to a new branch of isophoric regular arrays with reduced side lobe level. However, its benefit should be validated in planar configurations, where the effects of the mutual coupling become stronger, but a careful design of the the corresponding feeding network might solve some of the design issues.

Bibliography

[1] J. L. Volakis, *Antenna Engineering Handbook,* McGraw-Hill, 2007.

[2] S. K. Rao, L. Shafai, and S. K. Sharma, *Handbook of Reflector Antennas and Feed Systems*, Volume 3, Artech House, 2013.

[3] R. Dybdal, *Communication satellite antennas: system architecture, technology, and evaluation,* McGraw-Hill, 2009.

[4] Recommendation ITU-R S.465-6, "Reference radiation pattern of earth station antennas in the fixed-satellite service for use in coordination and interference assessment in the frequency range from 2 to 31 GHz," Jan. 2010.

[5] C. A. Balanis, "Modern antenna handbook," *Wiley-Interscience* New York, NY, USA, 2008.

[6] B. Elbert, *Introduction to satellite communication,* Artech House, 2008.

[7] B. G. Evans, *Satellite communication systems,* Iet, 1999.

[8] P. D. Potter, *A new horn antenna with suppressed sidelobes and equal bandwidths,* Jet Propulsion Laboratory, California Institute of Technology, 1963.

[9] T. Katagi and Y. Takeichi, "Shaped-beam horn-reflector antennas," *IEEE Trans. Antennas Propag.*, vol. 23, no. 6, pp. 757-763, Nov. 1975.

[10] S. K. Rao, "Design and analysis of multiple-beam reflector antennas," *IEEE Antennas and Propagation Magazine*, vol. 41, no. 4, pp. 53-59, Sep. 1999.

[11] R. J. Mailloux, *Phased Array Antenna Handbook,* Artech House, 1994.

[12] R. C. Hansen, Phased array antennas, *Phased Array Antennas,* John Wiley & Sons, 2009.

[13] S. P. Skobelev, “Methods of constructing optimum phased-array antennas for limited field of view,” *IEEE Antennas and Propagation Magazine*, vol. 40, no. 2, pp. 39-50, Apr. 1998.

[14] R. E. Collin and F. J. Zucker, *Antenna Theory,* McGraw-Hill, 1969.

[15] Doyle, W. L., “On Approximating Linear Array Factors”, Santa Monica, CA: RAND Corporation, 1963.

[16] G. Toso, C. Mangenot, and A. G. Roederer, “Sparse and thinned arrays for multiple beam satellite applications,” *Proceedings of the 2nd European Conference on Antennas and Propagation (EuCAP), 2007*, Nov. 2007.

[17] O. M. Bucci, T. Isernia, A. F. Morabito, S. Perna, and D. Pinchera, “Aperiodic arrays for space applications: An effective strategy for the overall design,” *Proceedings of the 3rd European Conference on Antennas and Propagation (EuCAP), 2009*, pp. 2031-2035, Mar. 2009.

[18] O. M. Bucci, M. D’Urso, T. Isernia, P. Angeletti, and G. Toso, “Deterministic Synthesis of Uniform Amplitude Sparse Arrays via New Density Taper Techniques,” *IEEE Transactions on Antennas and Propagation*, vol. 58, no. 6, pp. 1949-1958, Jun. 2010.

[19] A. Catalani, L. Russo, O. M. Bucci, T. Isernia, A. F. Morabito, S. Perna, and G. Toso, “Sparse arrays for satellite communications: from optimal design to realization.” *32nd ESA Antenna Workshop on Antennas for Space Applications*, Vol. 4, Oct. 2010.

[20] S. J. Stirland and A. D. Craig, “Phased Arrays for Satellite Communications: Recent Developments at Astrium Ltd,” *Proceedings of the* 2^{nd} *European Conference on Antennas and Propagation (EuCAP)*, pp. 11-16, Nov. 2007.

[21] R. J. Mailloux, “An overlapped subarray for limited scan application,” *IEEE Transactions on Antennas and Propagation*, vol. 22, no. 3, pp. 487-489, May 1974.

[22] S.P. Skobelev, “Analysis and synthesis of an antenna array with sectoral partial radiation patterns”, *Telecommun. Radio Eng.*, Vol. 45, pp. 116-119, Nov. 1990

[23] G. V. Trentini, “Partially reflecting sheet arrays,” *IRE Trans. Antennas Propag.*, vol. 4, no. 4, pp. 666-671, Oct. 1956.

[24] D. R. Jackson and N. Alexopoulos, "Analysis of planar strip geometries in a substrate-superstrate configuration," *IEEE Trans. Antennas Propag.*, vol. 34, no. 12, pp. 1430-1438, Dec. 1986.

[25] D. R. Jackson, A. A. Oliner, and A. Ip, "Leaky-wave propagation and radiation for a narrow-beam multiple-layer dielectric structure," *IEEE Trans. Antennas Propag.*, vol. 41, no. 3, pp. 344-348, Mar. 1993.

[26] R. Sauleau, Ph. Coquet, D. Thouroude, J.-P. Daniel, and T. Matsui, "Radiation characteristics and performance of millimeter wave horn-fed gaussian beam antennas," *IEEE Trans. Antennas Propag.*, vol. 51, no. 3, pp. 378-387, Mar. 2003.

[27] G. Lovat, P. Burghignoli, and D.R. Jackson, "Fundamental properties and optimization of broadside radiation from uniform leaky-wave antennas," *IEEE Trans. Antennas Propag.*, vol. 54, no. 5, pp. 1442-1452, May 2006.

[28] L. Leger, T. Monediere, and B. Jackson, "Enhancement of gain and radiation bandwidth for a planar 1-D EBG antenna," *IEEE in Microwave and Wireless Components Letters*, vol. 15, no. 9, pp. 573-575, Sep. 2005.

[29] R. Gardelli, M. Albani, and F. Capolino, "Array thinning by using antennas in a Fabry-Perot cavity for gain enhancement," *IEEE Trans. Antennas Propag.*, vol. 54, no. 7, pp. 1979-1990, Jul. 2006.

[30] D. Blanco, N. Llombart, and E. Rajo-Iglesias, "On the use of leaky wave phased arrays for the reduction of the grating lobe level," *IEEE Trans. Antennas Propag.*, vol. 4, no. 4, pp. 1789-1795, Apr. 2014.

[31] I. J. Bahl and K. C. Gupta, "A leaky-wave antenna using an artificial dielectric medium," *IEEE Trans. Antennas Propag.*, vol. 22, no. 1, pp. 119-122, Jan. 1974.

[32] C. Cheype, C. Serier, M. Thevenot, T. Monediere, A. Reineix, and B. Jecko,"An electromagnetic bandgap resonator antenna," *IEEE Trans. Antennas Propag.*, vol. 50, no. 9, pp. 1285-1290, Sep. 2002.

[33] D. R. Jackson and A. A. Oliner, "A leaky-wave analysis of the high-gain printed antenna configuration," *IEEE Trans. Antennas Propag.*, vol. 36, no. 7, pp. 905-910, Jul. 1988.

[34] T. Zhao, D. R. Jackson, J. T. Williams, and A. A. Oliner, "General formulas for 2-D leaky-wave antennas," *IEEE Trans. Antennas Propag.*, vol. 53, no. 11, pp. 3525-3533, Nov. 2005

[35] T. Zhao, D. R. Jackson, J. T. Williams, H. D. Yang, and A. A. Oliner, "2-D periodic leaky-wave antennas-part I: metal patch Design," *IEEE Trans. Antennas Propag.*, vol. 53, no. 11, pp. 3505-3514, Nov. 2005.

[36] T. Zhao, D. R. Jackson, and J. T. Williams, "2-D periodic leaky-wave antennas-part II: slot design," *IEEE Trans. Antennas Propag.*, vol. 41, no. 11, pp. 3515-3524, Nov. 2005.

[37] Neto, A., Llombart, N., "Wideband Localization of the Dominant Leaky Wave Poles in Dielectric Covered Antennas," *IEEE Antennas and Wireless Propagation Letters*, vol. 5, no. 1, pp. 549-551, Dec. 2006.

[38] A. Neto, N. Llombart, G. Gerini, M. D. Bonnedal, and P. De Maagt, "EBG enhanced feeds for the improvement of the aperture efficiency of reflector antennas," *IEEE Trans. Antennas Propag.*, vol. 55, no. 8, pp. 2185-2193, Aug. 2007.

[39] N. Llombart, A. Neto, G. Gerini, D. M. Bonnedal, and P. De Maagt, "Leaky wave enhanced feed arrays for the improvement of the edge of coverage gain in multibeam reflector antennas," *IEEE Trans. Antennas Propag.*, vol. 56, no. 5, pp. 1280-1291, May 2008.

[40] A. Neto, M. Ettorre, G. Gerini, and P. De Maagt, "Leaky wave enhanced feeds for multibeam reflectors to be used for Telecom satellite based links," *IEEE Trans. Antennas Propag.*, vol. 60, no. 1, pp. 110-120, Sep. 2006.

[41] R. Chantalat, C. Menudier, M. Thevenot, T. Monediere, E. Arnaud, and P. Dumon, "Enhanced EBG resonator antenna as feed of a reflector antenna in the Ka band," *IEEE Antennas and Wireless Propagation Letters*, vol. 7, pp. 349-353, 2008.

[42] H. Chreim, R. Chantalat, M. Thevenot, U. Naeem, S. Bila, T. Monediere, B. Palacin, Y. Cailloce, G. Caille, and P. de Maagt, "An enhanced Ka-band reflector focal-plane array using a multifeed EBG structure," *IEEE Antennas and Wireless Propagation Letters*, vol. 9, pp. 1152-1156, 2010.

[43] M. Ettorre, "Analysis and design of efficient planar leaky-wave antennas," *PhD thesis,* University of Siena, Siena, Italy, 2008.

[44] L. B. Felsen and N. Marcuvitz, "Radiation and Scattering of Waves," *Wiley*, 1994.

[45] S. J. Orfanidis, "Electromagnetic waves and antennas," *Rutgers University*, 2002.

[46] N. Llombart, "Development of integrated printed aray antennas using EBG substrates," *Ph.D. dissertation*, Universidad Politecnica de Valencia, Spain, May 2005.

[47] V. Galdi and I. M. Pinto, "A Simple Algorithm for Accurate Location of Leaky-Wave Poles for Grounded Inhomogeneous Dielectric Slabs," *Microwave and optical technology letters*, vol. 24, no. 2, pp. 135-140, Jan. 2000.

[48] R. F. Harrington., "Time-Harmonic Electromagnetic Fields," *Wiley*, 2001.

[49] C. A. Balanis, *Antenna Theory, Analysis and Design,* Wiley, New York, 2012.

[50] D. M. Pozar, "A relation between the active input impedance and the active element pattern of a phased array," *IEEE Trans. Antennas Propag.*, vol. 51, no. 9, pp. 2486–2489, Sep. 2003.

[51] N. Llombart, A. Neto, G. Gerini, D. M. Bonnedal, and P. De Maagt, "Impact of mutual coupling in leaky wave enhanced imaging arrays," *IEEE Trans. Antennas Propag.*, vol. 56, no. 4, pp. 1201-1206, Apr. 2008.

[52] J.L. Gomez-Tornero, Adl.T. Martinez, D.C. Rebenaque, M. Gugliemi, and A. Alvarez-Melcon, "Design of tapered leaky-wave antennas in hybrid waveguide-planar technology for millimeter waveband applications," *IEEE Trans. Antennas Propag.*, vol. 53, no. 8, pp. 2563-2577, Aug. 2005.

[53] I. Ohtera, "Diverging/focusing of electromagnetic waves by utilizing the curved leakywave structure: application to broad-beam antenna for radiating within specified wide-angle," *IEEE Trans. Antennas Propag.,* vol. 47, no. 9, pp. 1470-1475, Sep. 1999.

[54] R. Sauleau, Ph. Coquet, and J.-P. Daniel, "Validity and accuracy of equivalent circuit models of passive inductive meshes. Definition of a novel model for 2D grids," *International Journal of Infrared and Millimeter Waves*, vol. 23, no. 3, pp. 475-498, Mar. 2002.

[55] M. Diblanc, E. Rodes, E. Arnaud, M. Thevenot, T. Monediere, and B. Jecko, "Circularly polarized metallic EBG antenna," *IEEE Microwave and Wireless Components Letters*, vol. 15, no. 10, pp. 638-640, Oct. 2005.

[56] P. Franchi and R. J. Mailloux, "Theoretical and experimental study of metal grid angular filters for sidelobe suppression," *IEEE Trans. Antennas Propag.*, vol. 31, no. 3, pp. 445-450, May 1983.

[57] G. L. Matthaei, E. M. T. Jones, and L. Young, *Microwave filters, impedance-matching networks, and coupling structures,* McGraw-Hill, New York, 1964.

[58] N. T. Nguyen, R. Sauleau, and L. Le Coq, "Reduced-size double-shell lens antenna with flat-top radiation pattern for indoor communications at millimeter waves," *IEEE Trans. Antennas Propag.,* vol. 59, no. 6, pp. 2424-2429, Jun. 2011.

[59] R. J. Mailloux, "An overlapped subarray for limited scan application," *IEEE Trans. Antennas Propag.,* vol. 22, no. 3, pp. 487-489, May 1974.

[60] R. J. Mailloux, "Synthesis of spatial filters with Chebyshev characteristics", *IEEE Trans. Antennas Propag.*, vol. AP-24, no. 2, p. 174-181, Mar. 1976.

[61] R. Sauleau, Ph. Coquet, T. Matsui, and J.-P. Daniel, "A new concept of focusing antennas using plane-parallel Fabry-Perot cavities with non-uniform mirrors," *IEEE Trans. Antennas Propag.*, vol. 51, no. 11, pp. 3171-3175, Nov. 2003.

[62] G. Minatti, S. Maci, P. De Vita, A. Freni, and M. Sabbadini, "A Circularly-Polarized Isoflux Antenna Based on Anisotropic Metasurface," *IEEE Trans. Antennas Propag.*, vol. 60, no. 11, pp. 4998-5009, Nov. 2012.

[63] A. Brunner, "Possibilities of dimensioning doubly curved reflectors for azimuth-search radar antennas," *IEEE Transactions on Antennas and Propagation*, vol. 19, no. 1, pp. 52-57, Jan. 1971.

[64] R. S. Elliott and G. J. Stern, "A new technique for shaped beam synthesis of equispaced arrays," *IEEE Transactions on Antennas and Propagation*, vol. 32, no. 10, pp. 1129-1133, Oct. 1984.

[65] M. Arrebola, J. A. Encinar, and M. Barba, "Multifed printed reflectarray with three simultaneous shaped beams for LMDS central station antenna," *IEEE Transactions on Antennas and Propagation*, vol. 56, no. 6, pp. 1518-1527, Jun. 2008.

[66] R. Sauleau and B. Bares, “A complete procedure for the design and optimization of arbitrarily-shaped integrated lens antennas,” *IEEE Transactions on Antennas and Propagation*, vol. 54, no. 4, pp. 1122-1133, Apr. 2006.

[67] I. Ohtera, “On a forming of cosecant square beam using a curved leakywave structure,” *IEEE Transactions on Antennas and Propagation*, vol. 49, no. 6, pp. 1004-1006, Jun. 2001.

[68] W. Davis and R. Hladek, “Phased array antenna architecture having digitally controlled centralized beam forming,” *U.S. Patent*, no. 6,972,716, Dec. 2005.

[69] M. A. Al-Tarifi, D. E. Anagnostou, A. K. Amert, and K. W. Whites, “The puck antenna: a compact design with wideband, high-gain operation,” *IEEE Trans. Antennas Propag.*, vol. 63, no. 4, pp. 1868-1873, Apr. 2015.

[70] B. Fuchs, “Synthesis of sparse arrays with focused or shaped beampattern via sequential convex optimizations,” *IEEE Trans. Antennas Propag.*, vol. 60, no. 7, pp. 3499-3503, Jul. 2012.

[71] E. J. Candès, M. B. Wakin, and S. P. Boyd, “Enhancing sparsity by reweighted ℓ_1 minimization,” *Journal of Fourier Analysis and Applications*, vol. 14, pp. 877-905, Dec. 2008.

[72] R. Sauleau, Ph. Coquet, J.-P. Daniel, T. Matsui, N. Hirose, “Analysis of millimeter wave Fabry-Perot cavities using the FDTD technique,” *IEEE Microw. Guided Wave Lett.*, vol. 9, no. 5, pp. 189-191, Nov. 1999.

[73] G. Prisco and M. D’Urso, “Maximally sparse arrays via sequential convex optimizations,” *IEEE Antennas and Wireless Propagation Letters*, vol. 11, pp. 192-195, 2012.

[74] M. Grant and S. Boyd, CVX: Matlab software for disciplined convex programming, http://cvxr.com/cvx, Sep. 2013.

[75] HFSS-MATLAB-API, https://github.com/yuip/hfss-api, Oct. 2014.

[76] Recommendation ITU-R S.1329, “Frequency sharing of the bands 19.7-20.2 GHz and 29.5-30.0 GHz between systems in the mobile-satellite service and systems in the fixed-satellite service”, Sep. 1997.

Biography

Francesco Scattone was born in Rome, Italy, in 1987. He received the B.S. degree in electronic engineering and the M.S. degree (*summa cum laude*) in information and communications technology engineering from the University of Roma Tre, Rome, Italy, in 2009 and 2011, respectively. He is a Ph.D. candidate at the Institut d'Electronique et de Télécommunications de Rennes (IETR), University of Rennes 1, France. The Ph.D. project is in cooperation with the European Space Research and Technology Centre (ESA/ESTEC), Noordwijk, The Netherlands, where he spent four months.
His research interests include the analysis and design of antennas, with emphasis on arrays and leaky-wave antennas.

Publications

Journal Papers

F. Scattone, M. Ettorre, R. Sauleau, N. T. Nguyen, and N. J. G. Fonseca, "Optimization procedure for planar leaky-wave antennas with flat-topped radiation patterns," forthcoming on *IEEE Transactions on Antennas and Propagation.*

F. Scattone, M. Ettorre, B. Fuchs, R. Sauleau, and N. J. G. Fonseca, "Synthesis procedure for thinned leaky-wave-based phased array antennas with reduced number of controls," *IEEE Transactions on Antennas and Propagation*, under review.

Conference Proceedings

F. Scattone, M. Ettorre, R. Sauleau, and N. J. G. Fonseca, "A flat-topped leaky-wave source for phased arrays with reduced scan losses," *Proceedings of the 8th European Conference on Antennas and Propagation (EuCAP) 2014*, The Hague, The Netherlands, Apr. 2014.

F. Scattone, M. Ettorre, R. Sauleau, and N. J. G. Fonseca, "Generation of a cosecant-squared radiation pattern with a superstrate-like leaky-wave antenna," *Proceedings of the 9th European Conference on Antennas and Propagation (EuCAP) 2015*, Lisbon, Portugal, Apr. 2015.

F. Scattone, M. Ettorre, B. Fuchs, R. Sauleau, and N. J. G. Fonseca, "Synthesis procedure for thinned leaky-wave phased array antennas," *Proceedings of the 9th European Conference on Antennas and Propagation (EuCAP) 2015*, Lisbon, Portugal, Apr. 2015.

F. Scattone, M. Ettorre, B. Fuchs, R. Sauleau, and N. J. G. Fonseca, “Synthèse d’antennes réseaux raréfiés à ondes de fuite,” *Proceedings of the 18emes Journées Nationales des Micro-ondes 2015*, Bordeaux, France, Jun. 2015.

F. Scattone, M. Ettorre, B. Fuchs, R. Sauleau, and N. J. G. Fonseca, “Pattern shaping and synthesis of planar leaky-wave-based arrays for satellite communications,” *Proceedings of the International Conference on Electromagnetics in Advanced Applications (ICEAA 15)*, Torino, Italy, Sep. 2015.